PLASMA AND ION BEAM ENHANCED CHEMICAL VAPOUR DEPOSITION OF DIAMOND AND DIAMOND-LIKE CARBON

A Thesis Submitted to the College of

Graduate Studies and Research

In Partial Fulfillment of the Requirements

For the Degree of Doctor of Philosophy

In the Department of Mechanical Engineering

University of Saskatchewan

Saskatoon

By

YONGJI TANG

© Copyright Yongji Tang, August, 2010. All rights reserved.

PERMISSION TO USE

In presenting this thesis in partial fulfilment of the requirements for a Postgraduate degree from the University of Saskatchewan, I agree that the Libraries of this University may make it freely available for inspection. I further agree that permission for copying of this thesis in any manner, in whole or in part, for scholarly purposes may be granted by the professors who supervised my thesis work, Prof. Q. Yang and Prof. A. Hirose, or, in their absence, by the Head of the Department or the Dean of the College in which my thesis work was done. It is understood that any copying or publication or use of this thesis or parts thereof for financial gain shall not be allowed without my written permission. It is also understood that due recognition shall be given to me and to the University of Saskatchewan in any scholarly use which may be made of any material in my thesis.

Requests for permission to copy or to make other use of material in this thesis in whole or part should be addressed to:

Head of the Department of Mechanical Engineering

University of Saskatchewan

Saskatoon, Saskatchewan, S7N 5A9

Canada

ABSTRACT

WC-Co cutting tools are widely used in the machining industry. The application of diamond coatings on the surfaces of the tools would prolong the cutting lifetime and improves the manufacturing efficiency. However, direct chemical vapor deposition (CVD) of diamond coatings on WC-Co suffer from severe premature adhesion failure due to interfacial graphitization induced by the binder phase Co. In this research, a combination of hydrochloric acid (HCl) and hydrogen (H_2) plasma pretreatments and a novel double interlayer of carbide forming element (CFE)/Al were developed to enhance diamond nucleation and adhesion. The results showed that both the pretreatments and interlayers were effective in forming continuous and adhesive nanocrystalline diamond coatings. The method is a promising replacement of the hazardous Murakami's regent currently used in WC-Co pretreatment with a more environmental friendly approach.

Apart from coatings, diamond can be fabricated into other forms of nanostructures, such as nanotips. In this work, it was demonstrated that oriented diamond nanotip arrays can be fabricated by ion beam etching of as-grown CVD diamond. The orientation of diamond nanotips can be controlled by adjusting the direction of incident ion beam. This method overcomes the limits of other techniques in producing nanotip arrays on large areas with controlled orientation. Oriented diamond nano-tip arrays have been used to

produce anisotropic frictional surface, which is successfully used in ultra-precision positioning systems.

Diamond-like carbon (DLC) has many properties comparable to diamond. In this thesis, the preparation of α-C:H thin films by end-Hall (EH) ion source and the effects of ion energy and nitrogen doping on the microstructure and mechanical properties of the as-deposited thin films were investigated. The results have demonstrated that smooth and uniform α-C:H and α-C:H:N films with large area and reasonably high hardness and Young's modulus can be synthesized by EH ion source with a low ion energy. The EH ion beam deposition of carbon-based thin films have potential applications such as protective coatings on high capacity magnetic memory disk, for which coating uniformity and smoothness cannot be achieved by the traditional sputtering methods.

ACKNOWLEDGMENTS

I would like to express deepest thanks and appreciation to my supervisors, Profs. Qiaoqin Yang and Akira Hirose, for their invaluable guidance, encouragement throughout this thesis work and truly care about my personal development. I wish to extend my appreciation to my advisory committee members, Profs. Ikechukwuka N.A. Oguocha, Chijin Xiao and Michael P. Bradley, for their invaluable support, constructive criticism and useful suggestions.

I especially thank Dr. Yuanshi Li for the insightful discussions and fruitful collaboration in experiments. My special thanks also go to Mr. Robert Peace for his technical assistance in materials synthesis and characterization facilities in the Department of Mechanical Engineering and Mr. David McColl for the help of CVD equipment in the Plasma Physics Laboratory. A note of thanks is also in order for those who provided help in sample characterization: Mr. H.-J. Steinmetz for conducting the indentation test, Mr. Tom Bonli for SEM and XRD, Mr. Jason Maley for Raman spectroscopy, Mr. T. Regier and Dr. R. Blyth for NEXAFS experiments, and Dr. D. Karpuzov for XPS and film thickness measurement.

Finally, I would like to thank all my family members for their patience and love throughout the tenure of my work on this thesis.

The financial support provided by the Canada Research Chair Program, the Natural Sciences and Engineering Research Council of Canada, Canada Foundation for Innovation and the University of Saskatchewan is acknowledged with gratitude.

Dedication

To my wife, Munan, my daughter, Grace, and my son, Aaron

TABLE OF CONTENTS

LIST OF TABLES

LIST OF FIGURES

LIST OF ACRONYMS

α-C	Amorphous carbon
α-C:H	Hydrogenated amorphous carbon
AFM	Atomic force microscopy
BEN	Bias enhanced nucleation
BSE	Backscattered electrons
CFE	Carbide forming element
CLS	Canadian Light Source Inc.
CVD	Chemical vapor deposition
DLC	Diamond-like carbon
EH	End-Hall
ESCA	Electron spectroscopy for chemical analysis
EXAFS	Extended X-ray absorption fine structure
FCC	Face-centered cubic
FCVA	Filtered cathode vacuum arc
FEE	Field electron emission
FIB	Focused Ion Beam
FLY	Fluorescence yield

FWHM	Full-width at half maximum
HFCVD	Hot filament chemical vapour deposition
HPHT	High pressure and high temperature
IBAD	Ion beam assisted deposition
IBE	Ion beam etching
LMIS	Liquid-metal ion sources
MEMS	Microelectromechanical system
MPCVD	Microwave plasma enhanced CVD
NCD	Nanocrystalline diamond
N-DLC	Nitrogen doped diamond-like carbon
NEXAFS	Near edge x-ray absorption fine structure spectroscopy
PDSSA	Piezoelectric-driven stick-slip actuator
PEA	Piezoelectric actuator
RIE	Reactive ion etching
RMS	Root mean square
SE	Secondary electron
SEM	Scanning electron microscopy
SGM	Spherical grating monochromator
SPM	Scanning probe microscopy
STM	Scanning tunneling microscopy
SZM	Structure zone model
tα-C	Tetrahedral amorphous carbon
tα-C:H	Hydrogenated tetrahedral amorphous carbon

TEY	Total electron yield
TPA	Trans-polyacetylene
UMT	Universal Material Tester
WC-Co	Cobalt-cemented tungsten carbide
XPS	X-ray photoelectron spectroscopy
XRD	X-ray diffraction

CHAPTER 1
INTRODUCTION

Materials are playing a key role in modern technologies, from automobile, aircraft, and space technology to micro- and nano-electromechanical systems. This is true not only for the working parts and components produced, but also for the tools used to fabricate them. Hard materials are specifically important for tools and components which require high wear resistance.

Materials with extremely high bulk modulus and high hardness are marked with short bond length, high coordinate number, and low ionicity. Such materials are found in the periodic table in the direct vicinity of carbon. According to the present state of knowledge, intrinsically hard materials should be restricted to the elements of boron (B), carbon (C), and nitrogen (N). In the B/C/N system, materials with tetrahedral sp^3 hybridization structure have relatively shorter bond length, higher coordinate number, and lower ionicity than other structures like sp and sp^2 hybridization. This research focused on thin films and nanostructures of these three types of materials in the B/C/N system: diamond, diamond-like carbon (DLC), nitrogen doped diamond-like carbon (N-DLC).

1.1 Structure and Properties of Diamond

Figure 1.1 shows a diamond structure which, in essence, can be viewed as a face-centered cubic (FCC) lattice, with a basis of two identical carbon atoms: one at (0, 0,

0) and the other at (1/4, 1/4, 1/4), where the coordinates are given as fractions along the cube sides. This structure is also equivalent to two interpenetrating FCC lattices, offset from one another along a body diagonal by one-quarter of its length.

In the diamond structure the atoms are connected by strong directional σ bonds, with each carbon atom bonded to four others in a tetrahedral geometry. With this kind of structure, diamond has a number of extreme physical properties. As listed in Table A1.1 (in Appendix), diamond is by far the hardest known natural material, and has the highest atom density, the largest room temperature thermal conductivity, and smallest thermal expansion coefficient. It is chemically inert, has low friction coefficient, excellent wear resistance and biocompatibility. It has a wide band gap of 5.5 eV with the largest electron and hole velocities of any semiconductor [*Angus and Hayman*, 1988].

1.2 Diamond synthesis

The first successful synthesis of diamond was achieved using high pressure (~12.5 GPa) high temperature (~3000 ºC) (HPHT) method by General Electric in the 1960s [*Bundy*, 1962; *Bundy*, 1963]. However, besides the high price, the diamond synthesized by the HPHT process is in the form of small particles, ranging from nanometers to a few millimetres, too small for many practical applications. In the 1980's, it was found that diamond thin films could be synthesized by chemical vapor deposition (CVD) with hydrogen and methane gas mixture at relatively low temperature (~1000 ºC) and low pressure (vacuum) [*Matsumoto et al.*, 1982a; *Celii*

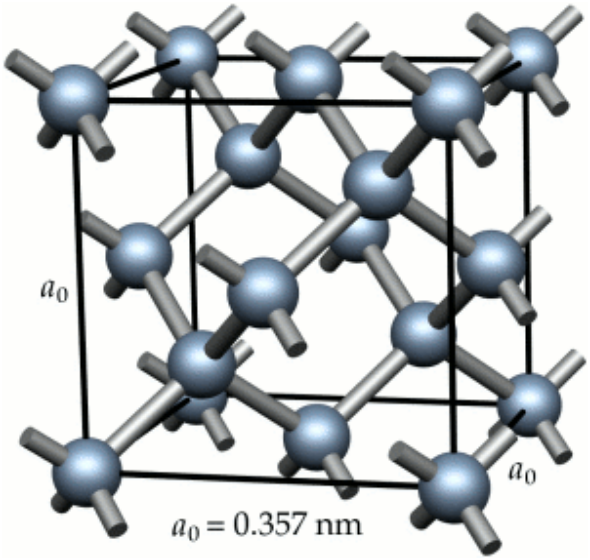

Figure 1.1. Structure of diamond crystal [http://newton.ex.ac.uk].

et al., 1991]. The CVD diamond has mechanical, tribological, and even electronic properties comparable to those of natural diamond. CVD involves a gas-phase chemical reaction occurring above a solid surface, which results in deposition onto the surface. All CVD techniques for producing diamond require a means of activating gas-phase carbon-containing precursor molecules. This can be achieved by thermal, e.g. hot filament CVD (HFCVD), or plasma, e.g. microwave plasma enhanced CVD (MPCVD).

1.2.1 HFCVD

Figure 1.2 shows the operational principles of HFCVD for producing diamond. In HFCVD, a metal filament (usually tantalum or tungsten) is heated to high temperatures (about 2000 K) to activate precursor gas mixture. For diamond deposition, a mixture of methane (CH_4) and hydrogen (H_2) (0.5-1% v/v) is used as

the precursor. After passing through the hot filament, CH_4/H_2 is activated to create free reactive radicals and atomic H for diamond deposition. The substrate is placed within a small distance from the filament (~1 cm) and maintained at a temperature in the range 1000-1400 K. The deposition is performed at reduced pressures (1 to 30 Torr).

The main advantage of HFCVD is its simple set-up. It is less expensive than most other CVD methods. The other advantage is its ability to scale up. By paralleling multiple filaments, a large isothermal area for deposition can be achieved. However, the filament method often suffers from contamination problems since metal from the filament may be evaporated and incorporated into the growing diamond film.

1.2.2 MPCVD

MPCVD is one of the plasma enhanced CVD methods. The reason to use plasma in deposition is to decompose relatively stable molecules and enhance deposition at much lower temperatures than in the thermal CVD. Besides that, energetic ions in plasma with a kinetic energy of a few to 100 eV may bombard the film surface, making the films denser with more compressive stress. In MPCVD, microwave frequencies are used to excite and sustain the plasmas. A schematic of a MPCVD reactor is presented in Figure 1.3, where microwaves (usually 2.45 GHz, a typical industrial frequency) are directed along a waveguide and are coupled into the chamber via an antenna. The microwaves pass through a quartz window and into the reactor.

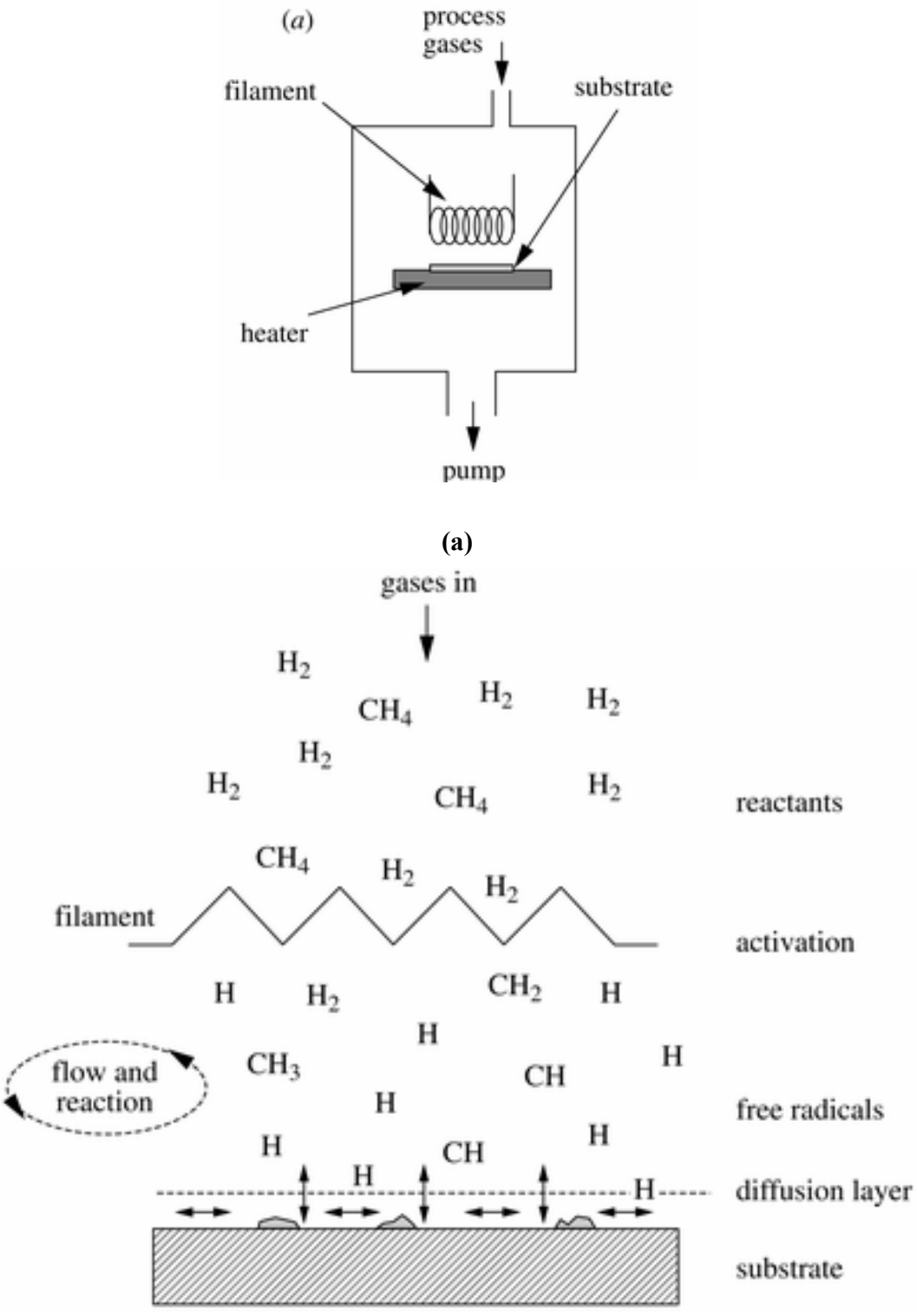

Figure 1.2. A schematic diagram of operation principles of HFCVD: (a) experiment setup (b) chemical process [*Ferro*, 2002].

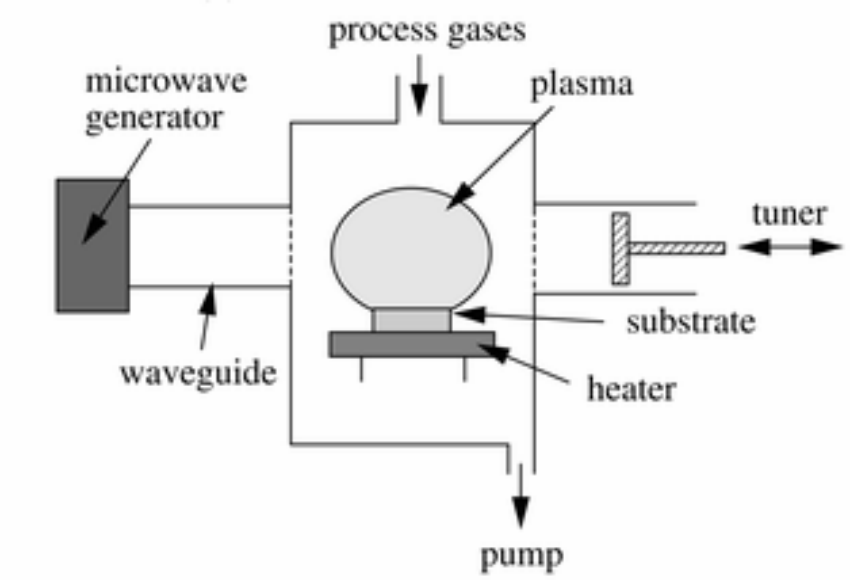

Figure 1.3. A schematic diagram of operation principles of MPCVD [*Ferro*, 2002].

There are some advantages of MPCVD over other CVD methods. It is clean since it is electrodeless without high potentials to cause sputtering. The plasma density produced by microwave can be very high. For example, an excitation frequency of 2.45 GHz allows densities to approach $10^{11}/cm^3$. The re-productivity of diamond films by MPCVD is much better than other CVD methods. A major drawback of MPCVD is its limited uniform area for deposition and low growth rate.

1.2.3 Role of Hydrogen in Diamond synthesis

It is well known that graphite, instead of diamond, is the stable form of solid carbon at the ambient conditions (atmospheric pressure and room temperature). Diamond is stable only at high temperatures and high pressures. The synthesis of diamond by CVD technique at low pressures and relatively low temperature is largely attributed

to the existence of hydrogen in the CVD process. First, hydrogen enhances the decomposition of methane (carbon source gas) into free reactive radicals, such as CH•, CH_2•, and CH_3•, which are the precursors for the formation of diamond. Second, atomic H terminates the "dangling" carbon bonds on the growing diamond surface and thus prevents them from forming graphite structures. Although graphite structures form on the surface, atomic H has the ability to selectively etch off the graphite since they etch graphitic much fast than diamond-like carbon. Thus, graphite structure can be preferably removed and only diamond structure left on the surface.

1.2.4 Diamond Nucleation

Nucleation is essential for diamond growth. A good control of the nucleation process would lead to the control of microstructure of the synthesized diamond thin films. For example, high nucleation density leads to the growth of smooth and dense diamond film with improved optical and electrical properties. High nucleation density also results in well adherent diamond films which is essential for many applications.

The nucleation of diamond on non-diamond substrates is challenging due to its high surface energy and crystal structure mismatch. For instance, the nucleation density of diamond on polished single crystal silicon wafer is only 10^4 cm^{-2} and the incubation time can be several hours under common conditions [*Pehrsson et al.*, 1993]. Two methods have been found effective in enhancing diamond nucleation: surface scratching and bias enhanced nucleation (BEN). In 1982, Matsumoto *et al*.

[*Matsumoto et al.*, 1982b] developed an abrasive pre-treatment technique, diamond powder scratching, to enhance diamond nucleation. In this method, substrate materials were scratched manually with diamond powders or ultrasonically treated in a liquid suspension of diamond powders resulting in a nucleation density of between 10^8 and 10^9 cm^{-2}. The mechanism can be attributed mainly to the creation of surface defects [*Chen et al.*, 1995; *Iijima et al.*, 1991], which act as nucleation sites during the diamond growth stage. In addition, the diamond particles left on the substrate surface can serve as nuclei for the subsequent growth of diamond [*Iijima et al.*, 1990; *Iijima et al.*, 1991].

In 1991, Yugo *et al*. [*Yugo et al.*, 1991] observed that the nucleation density of diamond on silicon substrates by MPCVD increased drastically by applying a negative bias voltage between the plasma and the substrate at the initial stage of the deposition. The applied bias voltage is typically between -200 V and -300 V, and a nucleation density ranging 10^9 to 10^{11} cm^{-2} can be achieved.

The advantages of BEN over abrasive treatment are: (i) BEN can be carried out in the same reactor as the subsequent deposition and the pretreatment; (ii) cleaning steps, which are necessary for the abrasive treatment, are avoided; (iii) the BEN process results in nuclei which are oriented with respect to each other and also to the underlying substrate [*Jiang et al.*, 1993; *Stoner et al.*, 1992] whereas the abrasive treatment inevitably leads to randomly oriented diamond nuclei.

With standard nucleation enhancement methods, as-synthesized diamond thin films usually have a grain size of a few micrometers. By changing the gas phase chemistry,

diamond thin film microstructure can be controlled so that grain size can be reduced to the nanometer scale. Michler *et al*. observed that the morphology of diamond films changed from faceted microcrystals to ball-shaped clusters of nanocrystals when the CH_4 content in the CH_4/H_2 mixture was increased while the substrate temperature was kept constant [*Michler et al.*, 1999]. As revealed by the electron diffraction, the diamond thin film synthesized at CH_4 content of 9% and substrate temperature of 800 ºC was of pure phase quality. As exemplified by Zhou *et al*. [*Zhou et al.*, 1998], by maintaining a constant carbon content (e.g., 1% CH_4) while substituting a noble gas (e.g., Ar) for hydrogen, the diamond thin film morphology changed from faceted microcrystals to equiaxed nanocrytals in the range of 3-5 nm.

The difficulty of diamond nucleation on transition metal-containing substrate such as cobalt-cemented tungsten carbide (WC-Co) comes from not only its high surface energy and crystal structure mismatch, but also the easiness for forming graphitic phases. Transition metals including Fe, Co, and Ni catalyze the growth of graphite, which leads to the formation of a graphite layer on the substrate surface prior to the growth of diamond. The formation of a soft graphite layer between the substrate and the diamond thin films results in poor adhesion of coatings to substrates [*Polini*, 2006; *Tang et al.*, 2009]. The remaining discussion in this section will take (WC-Co) substrate as an example.

WC-Co is widely used in the machining of carbon/graphite, plastics, fiber glass, and aluminum composites. Applying diamond coatings on the surfaces of tools prolongs their lifetime and improves manufacturing efficiency. For instance, the flank wear rate of diamond-coated cutting tools can be reduced by half as compared to the

uncoated ones [*Polini*, 2006]. However, CVD diamond coatings suffer from severe premature adhesion failure on WC-Co due to interfacial graphitization induced by Co. Co-cemented carbides contain cobalt as a binder to provides additional toughness to the tools, but it is hostile to diamond adhesion. Co, with partially filled 3d shell, acts as a catalyst for the formation of graphite. The graphite layer formed during the early stages of deposition makes it difficult for diamond to adhere well to the underlying substrate.

There are two widely used approaches to reduce the deleterious effect of cobalt and improve the adhesion of diamond coating on WC-Co. The first is to remove the cobalt binder phase on the surface by chemical etching. Peters and Cummings [*Peters and Cummings*, 1992] developed an effective two-step chemical etching process in which the substrate was first treated with Murakami's reagent ($K_3Fe(CN)_6$: KOH : H_2O = 1 : 1 : 10) and then etched with Caro's acid (a H_2SO_4–H_2O_2 solution). The Murakami's reagent attacks WC grains and thus roughens the substrate surface whereas Caro's acid oxidizes the binder to soluble Co^{2+} compounds and thus reduces the surface Co concentration.

The other method is to suppress the interactions between the binder and the deposited carbon films by using an interlayer which has a low diffusion coefficient for both C and Co and an intermediate thermal expansion coefficient between WC-Co and diamond. Many researchers have reported improvements in adhesion using various interlayers, such as amorphous carbon [*Deuerler et al*., 1996], metallic materials (Ti-Si) [*Lin et al.*, 1998], ceramics (SiAlON, Al_2O_3, SiC, Si_3N_4, TiC, TiN, CrN and WC) [*Cappelli et al.*, 1996; *Wright et al.*, 1994; *Silva et al.*, 1999; *Faure et*

al., 1999; *Polini*, 2006] and whisker reinforced ceramics (Al_2O_3 + SiC and ZrO_2) [*Cappelli et al.*, 1996]. Among these interlayers, CrN appears to be most effective [*Polini*, 2006; *Gowri et al.*, 2007; *Buijnsters et al*., 2002]. However, the CrN interlayer has to be several μm in thickness in order to sufficiently block the reaction of C and Co atoms. The thick interlayer may lead to the loss of sharpness of the cutting edge as well as increasing the brittleness of the coatings. In addition, diamond nucleation rate on nitrides is relatively low, which decreases the adhesion of diamond coatings.

Apart from flat thin films, diamond can be synthesized into other forms of nanostructures. In the section to follow, diamond nanotips will be discussed.

1.3 Diamond Nanotips

Aligned nanostructure arrays, such as nanotubes, nanofibres, nanowires, and nanotips, are recognized to have potential applications in vacuum microelectronics, optoelectronics and microelectromechanical system (MEMS). Among the nanostructures, diamond nanotip arrays are the most attractive as field electron emitter because of their superior field electron emission (FEE) properties [*Lu et al.*, 2006] and their high rigidity. Nanotips can also be used as probes in atomic force microscopes (AFMs) and scanning tunneling microscopes (STMs), write/read/erase heads in nanomechanical storage devices, and vibrating elements in MEMS devices.

1.3.1 Synthesis of Diamond Nanotip by CVD

Two methods are used to synthesize diamond nanotips, namely: bottom-up and top-down. The bottom-up method refers to the direct growth of diamond nanotips on substrates, usually by CVD. Well-aligned diamond nanotips have been grown by HFCVD on CVD diamond-coated Si substrates by Yang *et al*. [*Yang et al.*, 2005] in which the substrate holder was negatively biased in a DC glow discharge. In this case, the ion etching in the local electrical field was considered to be responsible for the oriented nanotip structure growth. Similarly, Chih *et al*. [*Chih et al.*, 2006] reported the growth of diamond nanotips on polycrystalline diamond substrates at a bias voltage of -250 V in a planar microwave plasma enhanced CVD system. The top-down method refers to the synthesis of diamond nanotips by post-treatment of polycrystalline diamond coatings with ion etching. Zhang *et al*. [*Zhang et al.*, 2003; *Zhang et al.*, 2004] reported the development of diamond conical structures by performing bias-assisted reactive ion etching in a hydrogen plasma on as-grown microwave CVD diamond. Ando *et al*. [*Ando et al.*, 2002] reported sharp diamond nanotips formed on single crystal diamond wafers by using reactive ion etching (RIE) in association with photolithography.

In both bottom-up and top-down methods, energetic ion etching is essential in the forming of nanotip structures. The mechanism of fabricating a nanotip structure by ion etching has recently been proposed by Yang *et al*. [*Yang et al.*, 2009], in which an angle-dependent ion sputtering model was developed to explain the crucial role of ion etching in nanotip formation.

For the method of ion etching by plasma bias in CVD, the ion etching process is difficult to control due to the system limitations. For instance, the ion energies must be limited below the arcing threshold and can only be increased to a few hundred eV. Moreover, the spatial distribution of ions, which is affected by plasma distribution in the chamber, is non-uniform. In addition, incident ions can only be perpendicular to substrate surfaces, making the control of nanotip orientation almost impossible. For the fabrication of nanotips by RIE, the lithography process is necessary, which is complicated and the orientation control is also hard to achieve.

The ion beam technique, which produces and extracts energetic ions from independent ion sources, has better control of ion dose, species, and energy compared to the plasma bias techniques and is a promising method for diamond nanotip fabrication.

1.3.2 Diamond Nanotips by Ion Beam Etching

1.3.2.1 Principle of Focused Ion Beam

The focused ion beam (FIB) usually uses liquid-metal ion sources (LMIS) operating with gallium ion sources. In a gallium LMIS (shown in Figure 1.4), gallium liquid is placed in contact with a sharpened tungsten needle and heated. A high electric field (greater than 10^8 V/cm) is applied for ionization and field emission of gallium ions (Ga^+). Ga^+ ions are then accelerated to energy of 5-50 keV, and focused onto the sample by electrostatic lenses. LMIS produce high current density ion beams with a very small energy spread, typically a few eV. The primary Ga^+ ion beam hits the

sample surface and sputters away (mill) material from a defined area with dimensions typically in square microns or deposit material onto it as shown in Figure 1.5. At high primary currents, a great deal of material can be removed by sputtering, allowing precision milling of the specimen down to a sub micron scale.

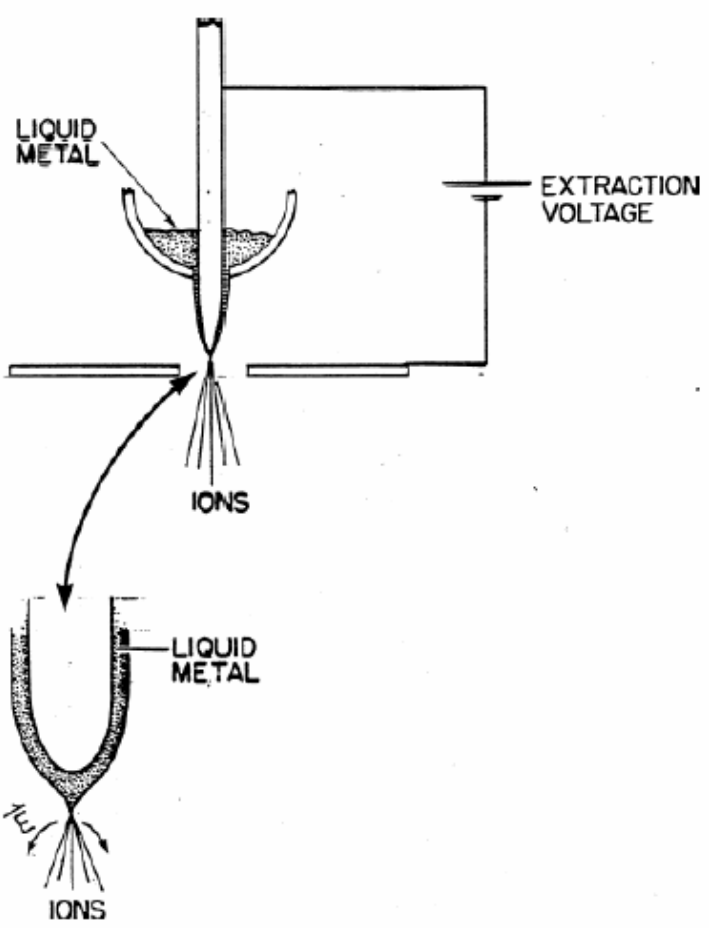

Figure 1.4. A schematic diagram of a liquid metal ion source [*Melngailis et al.*, 2001].

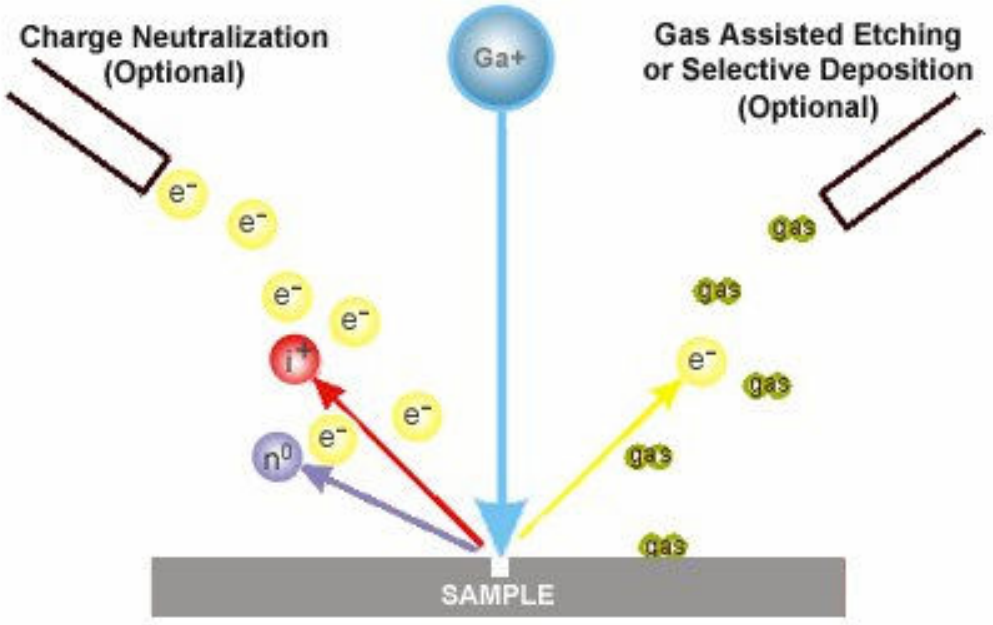

Figure 1.5. Principle of FIB etching
[http://en.wikipedia.org/wiki/Focused_ion_beam].

1.3.2.2 Principle of Broad Ion Beam

Broad ion beam has been widely used in materials processing, such as ion beam-assisted deposition (IBAD) and ion beam etching (IBE). In contrast to FIB, a broad ion beam system usually consists of a plasma source and an extractor. The plasma source that produces ions is located on one side of the ion beam system. An electrode at a high negative voltage, called the extractor, is located on the other side of the ion beam system. Ions flow from the plasma source towards the extractor and are accelerated to produce an energetic ion beam.

Two types of ion sources, Kaufman ion source (gridded) and end-Hall (EH) ion source (gridless), are commonly used in materials processing. Between the two, the Kaufman ion source is more suitable for ion beam etching and will be described here while end-Hall ion source is often used for ion beam (assisted) deposition and will be described later in this chapter.

Kaufman Ion Source

Of all types of ion beam sources, Kaufman ion beam source provides the most independent control of process parameters over a wide operating range [*Kaufman*, 1990]. As shown schematically in Figure 1.6, a discharge voltage (40 V) was applied between the filament cathode and the anode inside the ion source, adding feed gas and heating filament until it emits thermionic electrons. The electrons ionize the gas, forming a plasma. An array of magnets is used to increase the electron path lengths and obtain a uniform plasma source. The ions flowing from the plasma source are accelerated in the space between two grids, screen grid and accelerator grid. The inner grid or screen grid has the same potential as the electron source so that it screens the electron from escaping from the source. The outer accelerator grid is at a negative potential with respect to the source. The ions flowing to the accelerator grid gain energy and travel toward the surfaces of the samples. Ion flow is neutralized by electrons emitted from a separated hot filament as explained below.

Because they are positively charged, the ions accelerated from the ion source would repel each other and the beam would spread. Problems would also be raised when sputtering an insulating target or etching an insulating substrate. In addition, the ion

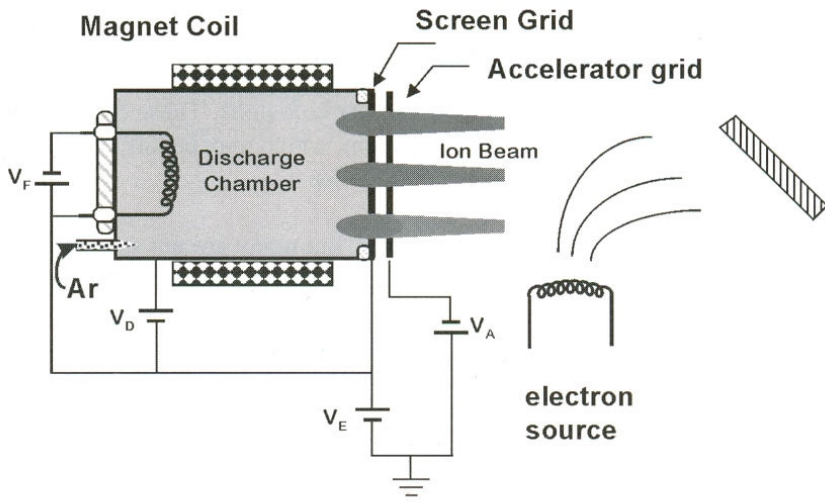

Figure 1.6. Schematic of Kaufman type gridded ion source [*Westwood*, 2003].

beam system would be negatively charged and pulls ions back if retardation of ions due to charging up occurs. Therefore, in Kaufman ion sources, a second electron source, called a neutralizer, is used to balance the ion current. A Kaufman type ion source uses a hot filament to emit electrons. Both ions and electrons arrive, there is no net charge arriving at the target.

Mechanism of Ion Beam Etching

Ion beam can be used to remove materials from surfaces, which is called ion beam etching, through physical collisions, chemical reactions or their combination. [*Kaufman*, 1979; *Lieberman*, 2005]

The removal of materials by physical collisions is also called sputtering. It occurs when energetic ions, e.g. Ar^+, make a series of collisions with atoms, e.g. C, in the

target. During the collisions, an energetic Ar^+ ion gives its energy to C atoms. The C atoms, after gaining enough energy, will be displaced from its normal lattice site. C atoms can be knocked off from the surface by directly colliding with Ar^+, or by colliding with other C atoms which gain energy from Ar^+ ions by cascade collision.

Sputtering is an anisotropic process, strongly sensitive to the angle of incident ions. Therefore, there is essentially no sidewall removal of material for normally incident ion etching. In addition, sputtering is the only process that can remove involatile products from a surface.

Sputtering is an unselective process since the sputtering yield at a given ion energy strongly depends on the binding energy and weakly on the masses of the target. Typically, the sputtering yields do not vary by more than a factor of 2-3 among different materials. Sputtering rates are generally small compared to commercially significant rates for material remove because the yield is typically of the order of one atom per incident ion.

A second etching mechanism is through pure chemical etching, in which the plasma discharge supplies gas-phase etchant atoms or molecules that chemically react with the surface to form volatile products. For example, F atoms etch solid silicon substrate to form gas-phase SiF_4. The etching process is highly chemically selective and isotropic. The etching rate can be quite large and only limited by the reactions at the surface leading to formation of etching products.

When an ion beam supplies both etchants and energetic ions to the surface, the etching rate is much higher than that of pure chemical etching or sputter along. This

process is called ion-enhanced energy-driven etching. Experiments suggest that etching is chemical in nature, but the etching rate is determined by the energetic ion bombardment. Because the energetic ions have a highly directional angular distribution, the etching can be highly anisotropic. The detailed mechanism for etch product formation and the rate of the formation are not well understood.

Synthesis of Diamond Nanotips by Ion Beam Etching

Taniguchi *et al*. [*Taniguchi et al.*, 1998 and 2000] studied the etching characteristics of CVD diamond using a Ga^+ FIB. A diamond nanotip with a less than 100 nm tip radius was obtained using Ga^+ FIB spot exposure. It was also found that by adding XeF_2 gas the etching rate increases by six times over the physical sputtering yield because fluorine reacts with graphite to produce carbon fluoride. The etch yield of diamond is orientation dependent. The (100) face has the highest etch yield of the three faces (100), (110), and (111). An amorphous layer of carbon caused by ion beam bombardment was also found on the surface of diamond.

Yu and Polycarpou [*Yu and Polycarpou,* 2004] produced a well-defined diamond tip, with a tip radius of 53.4 nm, using Ga^+ FIB with milling patterning technique on a blunt diamond indenter tip. The procedure Yu and Polycarpou adopted is described as follows. As shown in Figure 1.7, a blunt indenter tip was placed directly below the ion beam column. There was a circular ring shape ion milling patterning placed between ion column and the diamond indenter. The patterning played an essential role for the tip formation. The patterning allowed the beam to mill only the sidewalls of the indenter tip. The size of the patterning was computer controllable. In the

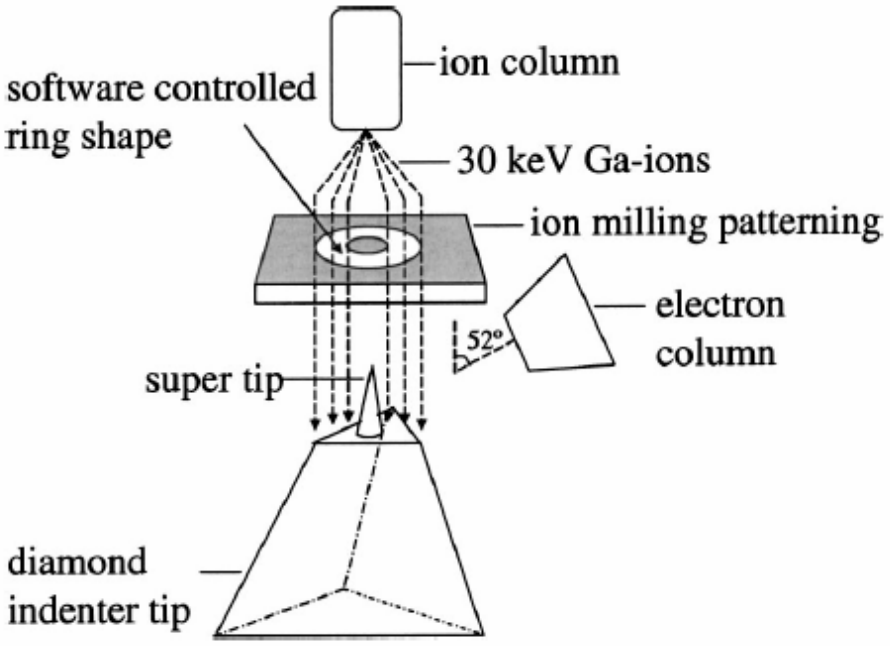

Figure 1.7. A schematic diagram of FIB milling with patterning [*Yu and Polycarpou*, 2004].

beginning, the patterning ring was set to 2 mm for outer radius and 1 mm for inner radius. After the first milling operation, the size of the patterning ring was reduced while keeping the ratio of the outer and inner radii the same to produce a progressively finer tip. The same steps were repeated four times with the last step having outer and inner radii of 0.15 and 0.08 mm, respectively. The complete milling process for sharpening the diamond tip took about 1 h. As shown in several experiments, FIB is a powerful tool for diamond nanotip fabrication. Nevertheless, apart from the high price of FIB system, the diamond nanotips can only be produced one by one by the system. The low efficiency would become an issue for making

diamond nanotip arrays on a large area unless using lithography method [*Wang et al.*, 2005]. Compared to FIB, broad ion beam has not only much lower cost but also much larger beam coverage. The coverage of broad ion beam can be up to several centimeters while FIB is just about few nanometers. In addition, the ion energy of broad ion beam is much lower than FIB (50-1500 eV comparing to tens of KeV). As a result, the damage to the surface microstructure would be much weaker.

1.4 Diamond-like Carbon

Diamond-like carbon (DLC) is a metastable form of amorphous carbon containing a significant fraction of sp^3 bonds [*Robertson*, 2002]. Because of the large amount of sp^3 bonds, DLC has some extreme properties similar to diamond, such as the hardness, elastic modulus and chemical inertness. There are some advantages of DLC, such as it is an isotropically disordered and relatively smooth thin film with no grain boundaries and it is less expensive to produce than diamond.

Jacob and Moller [Jacob and Moller, 1993] compared a large amount of data published on DLC and first introduced a ternary phase diagram as shown in Figure 1.8. According to the sp2, sp3 and H contents, carbon can form tetrahedral amorphous carbon (tα-C), hydrogenated tetrahedral amorphous carbon (tα-C:H), amorphous carbon (α-C), hydrogenated amorphous carbon (α-C:H), glassy carbon, graphite carbon, etc.

The main deposition methods for α-C thin films include ion beam, sputtering, arc discharge, and chemical vapour deposition. Because of the ability to independently control the ion energy and the ion current density, the ion beam deposition method

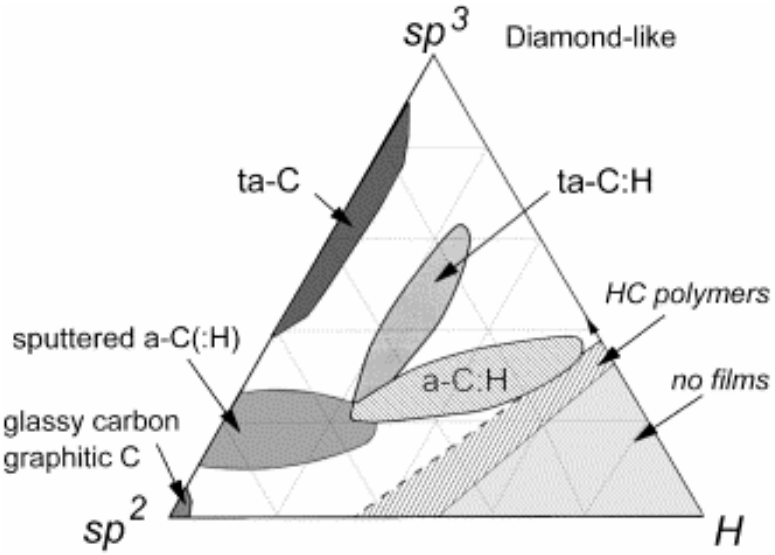

Figure 1.8. Ternary phase diagram of bonding in amorphous carbon-hydrogen alloys [*Robertson*, 2002].

has been widely used to produce α-C thin films. Since the pioneering work of Aisenberg and Chabot in 1971 [*Aisenberg and Chabot*, 1971], ion beam deposition of α-C thin films has been continuously advanced as a consequence of the development and innovation of ion sources. In the earlier ion beam systems, carbon ions were generated by plasma etching of carbon electrodes and accelerated by substrate potential [*Aisenberg and Chabot*, 1971]. Gridded ion beam source was developed in 1978 [*Kaufman*, 1978], in which magnetic field was used to improve ionization rate and grid optics was used to control the beam size and ion energy. In this ion beam source, hydrocarbon gas could be used as carbon source to enable the deposition of hydrogenated α-C films with varying C/H ratio.

It has been found that ion energy and ion current density are the two most important parameters affecting the microstructure and properties of ion beam deposited α-C

thin films [*Robertson*, 2002]. The beam current of gridded ion sources is limited to a maximum value of 500 mA by the space between the grids. The ion energy normally used is higher than 300 eV (the current is extremely low when the energy is below 300 eV). Gridless end-Hall ion sources [*Kaufman et al*., 1987] were then developed to provide ion beams with an average energy of 40 eV to 210 eV, which is a significant improvement over the gridded ion source to cover the low ion energy ranges.

Figure 1.9 shows a schematic of end-Hall ion source. Electrons are again emitted from a source such as a heated filament and accelerated to an anode. A permanent magnet provides a field parallel to the electron paths so that they follow spiral paths and increase ionization. Ions are accelerated toward the filament, which is also the cathode. Electrons, attracted by the positive charge of the ions, follow the ions to "neutralize" the beam.

Compared with the gridded ion sources, EH ion source has the advantage of easy installation, operation and maintenance. Most importantly, EH ion sources can supply large ion current (up to 5 A). The properties of thin films deposited in EH ion sources are dramatically improved compared with other sources. The low ion energy and high ion current in EH ion sources are the main factors that contribute to the improvement. Niederwald *et al*. [*Niederwald et al.*, 1999] compared EH, cold-cathode and plasma ion source deposited oxide thin films and found that EH ion source produced films with the highest density.

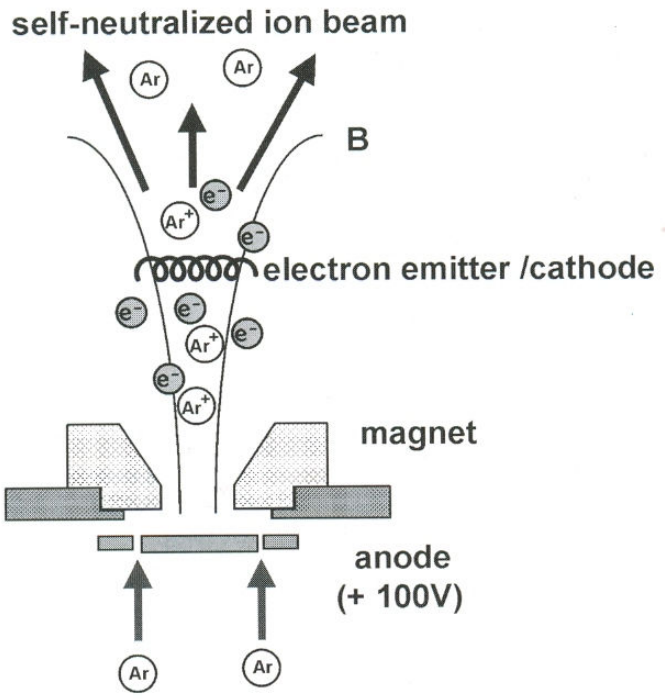

Figure 1.9. Schematic of end-Hall ion source [*Westwood*, 2003].

Since the introduction of EH ion beam for thin film deposition, there has been only a few investigations reported on α-C thin films. Grannen *et al*. [*Grannen et al.*, 2000] reported that EH ion beam deposited carbon films, which were used as an overcoat for magnetic thin film media, showed remarkable decrease in failure rate compared to the conventional hydrogenated or nitrogenated carbon thin films deposited by magnetron sputtering. Pan *et al*. [*Pan et al.*, 2007] reported the use of a custom-designed EH ion source to deposit α-C thin films, which showed excellent properties of infrared transmission and large-area uniformity. Although the progress has been made on EH ion beam deposited carbon thin films, little work has been reported on investigations of the microstructure and mechanical properties of α-C thin films deposited with EH ion beam.

1.5 Objectives of this research

1.5.1 Deposition and characterization of diamond coatings on WC-Co cutting tools

In order to deposit adherent diamond coating on WC-Co cutting tools, the cutting tools have to be pretreated by chemical etching or coated with interlayer to reduce the deleterious effect of cobalt. The most widely used chemical etching reagent ($K_3Fe(CN)_6$–KOH) contains $(CN)^-$ which is extremely hazardous for human beings and the environment. It is necessary to develop a cleaner pretreatment method for the growth of adhesive diamond coatings on WC-Co. In this work, a combination of hydrochloric acid etching and H_2 plasma treatment is used as pre-treatment to reduce surface Co concentration and modify the substrate surface morphology to increase coating adhesion.

In addition, a new double interlayer carbide-forming element (CFE)/Al for CVD of diamond coatings on WC-Co cutting tools is presented. A thin layer of Al deposited on WC-Co tools is used to suppress the formation of graphite catalyzed by Co and an additional thin layer of CFE is used to enhance diamond nucleation. The microsturcture, adhesion of diamond coating and the effect of Al and CFE interlayers on the nucleation and growth of diamond are studied.

1.5.2 Fabrication and orientation control of diamond nanotips by ion beam etching

To overcome the limitations of CVD, RIE and FIB in producing nanotip arrays on large areas with controlled orientation, in this work, broad ion beam technique was employed to manipulate nanostructure formation on the surface of CVD microcrystalline diamond to produce oriented diamond nanotip arrays.

1.5.3 Deposition and characterization of DLC thin films by end-Hall ion beam deposition

Although much progress has been made on EH ion beam deposited carbon thin films, little work has been reported on investigations of the microstructure and mechanical properties of α-C thin films deposited with EH ion beam. In this thesis, we report on the preparation of α-C thin films by EH ion source at a mean energy in the range 24 to 48 eV, which was not covered in previous reports, and the investigation of the effects of ion energy and nitrogen doping on the microstructure and mechanical properties of the as-deposited thin films.

1.6 Organization of the thesis

This thesis is composed of 9 chapters. A brief introduction of structure, properties and synthesis methods of diamond, diamond nucleation, diamond nanotips and diamond-like carbons has been given in this Chapter. The rest of the thesis is organized as follows.

Chapter 2 introduces experimental methodologies adopted in the thesis. Hot filament CVD and microwave plasma enhance CVD for diamond coating, and ion beam system for diamond etching, interlayer and α-C deposition will be described in details. In addition, various materials characterization techniques used in the thesis will be introduced.

Chapter 3 presents the results and discussions of the effect of chemical and plasma pretreatment on the deposition diamond coatings on WC-Co cutting tools. The results show that the tested combinations of hydrochloric acid and H_2 plasma pretreatments are all effective in forming continuous and adhesive nanocrystalline diamond coatings, while H_2 plasma pretreatment followed with HCl etching produces the highest diamond phase content.

Chapter 4 contains the deposition and characterization of diamond coatings on WC-Co cutting tools with Al interlayer. The results indicated that an Al thin film applied either directly on the blank tool substrate, or on the TiN, TiCN-interlayers, offers enhanced nucleation density and adhesion of the diamond films.

Chapter 5 presents a new double interlayer W/Al for CVD diamond coatings on WC-Co cutting tools. A thin layer of Al directly deposited on cutting tool is used to suppress the formation of graphite catalyzed by Co and an top layer of W is used to enhance diamond nucleation. The results have demonstrated that the W/Al interlayer can enhance diamond nucleation and adhesion on WC-Co tools and thus facilitating the formation of adherent diamond coatings on WC-Co inserts.

In Chapter 6, the diamond nucleation enhancement mechanism of Al and carbide-forming element interlayers (W, Cr and Ti) on WC-Co cutting tools were studied. The results showed that the CFE interlayers deposited by ion beam sputtering have amorphous/nanocrystalline structures to facilitate diamond nucleation and the formation of nanocrystalline diamond. Among the three interlayers investigated, diamond nucleation density was the highest on W and the lowest on Ti. The results also showed that the diamond nucleation density on CFE interlayers is much higher than those on widely used metal nitride interlayers.

Chapter 7 presents the fabrication and orientation control of diamond nanotips by broad ion beam etching. The experimental results clearly demonstrated that diamond nanotips can be fabricated by ion beam etching of as-grown CVD diamond. The orientation of diamond nanotips can be controlled by adjusting the incident ion direction. The surface with oriented diamond nanotip structure is proposed for the application in ultraprecise positioning system.

In Chapter 8, the characterization of hydrogenated amorphous carbon thin films by end-Hall ion beam deposition is presented. The results demonstrated that smooth and uniform α-C:H and α-C:H:N films with large area and reasonably high hardness and Young's modulus can be synthesized by EH ion source with a low ion energy. In addition, higher ion energy and doping with N can increase the fraction of sp^3 bonding, and thus improving the mechanical properties of the films.

Finally, the main results of the thesis are summarized in Chapter 9 with suggestions for future work.

CHAPTER 2
EXPERIMENTAL EQUIPMENTS AND CHARACTERIZATION TECHNIQUES

In this research, a HFCVD and a MPCVD were used for diamond growth, and an ion beam system was used for diamond etching, and interlayer and α-C deposition. The configuration of the equipments will be described in detail in this chapter. The synthesized materials were characterized by various characterization techniques, including scanning electron microscopy (SEM), atomic force microscopy (AFM), Raman spectroscopy, X-ray diffraction (XRD), X-ray photoelectron spectroscopy (XPS) and synchrotron based near edge x-ray absorption fine structure spectroscopy (NEXAFS). The principles of those techniques will be also explained in this chapter.

2.1 Experimental Equipments

2.1.1 CVD Reactors

HFCVD. The HFCVD reactor (Figure 2.1) was home made in the Plasma Physics Laboratory, University of Saskatchewan. It has four major components: a vacuum chamber, a pumping system, a gas flow system and a power supply. The vacuum chamber was made from a cross-shaped Pyrex glass tube of 150 mm in diameter. The pumping system is composed of a mechanical pump and a diffusion pump. The precursor gas is controlled by a two-channel gas flow meter. Methane (CH_4) and

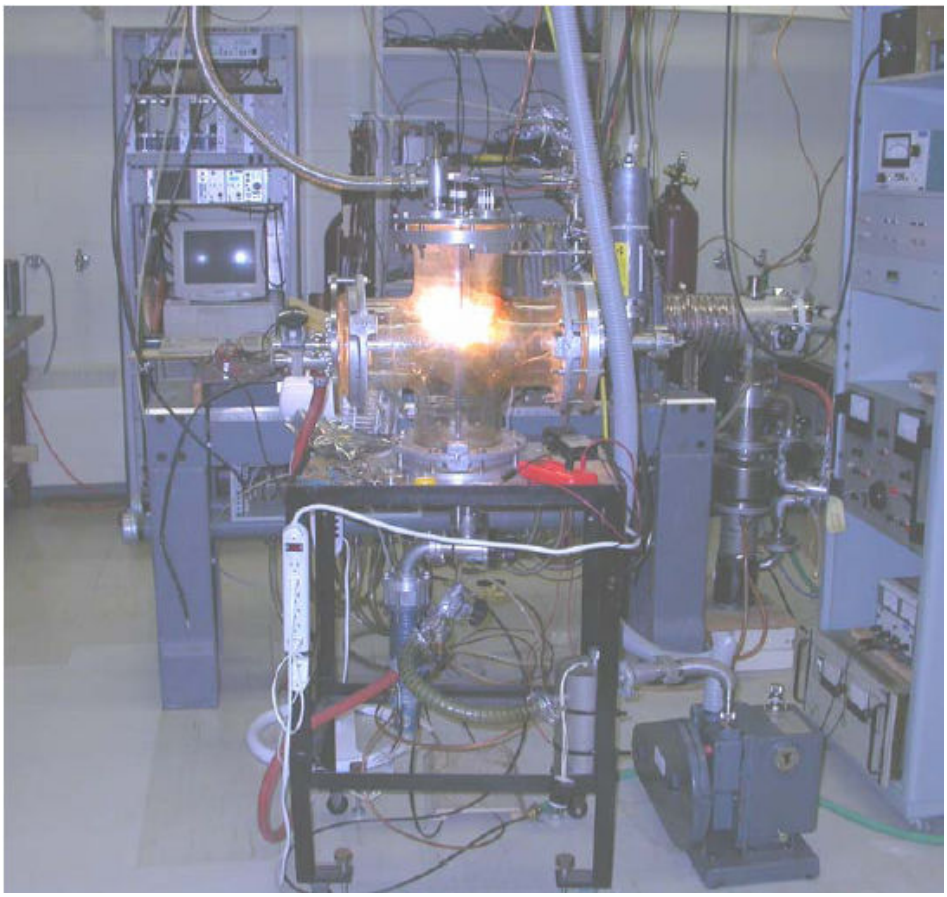

Figure 2.1. A picture of the HFCVD system.

hydrogen (H_2) were used as precursor gases for diamond growth. The gas mixture flows directly into the vacuum chamber from the top guided with a stainless steel tube. The filament used in the CVD chamber is a tungsten coil 4 mm in diameter and 40 mm in length. The coil is made from tungsten wire of 0.3 mm in diameter. The filament is connected to a power supply and ohmically heated to activate the precursor gas mixture into free reactive radicals. The radicals react and form diamond on the substrate. The substrate temperature is measured by a thermocouple mounted right behind the sample holder.

MPCVD. A MPCVD manufactured by Plasmionique Inc. (model number: MWPECVD 1250UOS) was used in this study. The system is composed of an ASTEX-type 2.45 GHz microwave source, a vacuum chamber, a pumping system, a gas flow system, and a manual/automatic control system as shown in Figure 2.2. The microwave source provides power up to 1.2 kW. The vertically oriented stainless steel vacuum chamber has an inner diameter of 140 mm. The substrate stage inside the vacuum chamber can be moved vertically to minimize microwave power reflection. During diamond deposition, the substrates were heated only by the plasma and substrate temperatures, measured with a thermocouple mounted right behind the substrate holder, were controlled by the applied microwave power. The precursor gas flow is controlled by a multi-channel flow meter. CH_4 and H_2 mixture was used as precursor for diamond growth.

2.1.2 Ion Beam System

An ion beam system was custom designed and manufactured by 4Wave Inc. The system consists of a vacuum chamber, a pumping system, a power supply and computer control system. Figure 2.3 shows the pictures of the ion beam system, (a) vacuum chamber and (b) control system and power supply. A schematic diagram of the configuration of the system is shown in Figure 2.4. Inside the vacuum chamber, there are targets, a sputter ion source, a preclean and assisted ion source, substrate holder and shutters for substrates and targets. The system is versatile and able to perform ion beam sputtering, ion beam etching and ion beam deposition.

Figure 2.2. A picture of the MPCVD system.

Ion Beam Sputtering. When only sputter ion source is in operation, target materials will be sputtered and deposited on the substrate, which is called ion beam sputtering. The interlayers on WC-Co for diamond growth to be discussed in Chapter 5 and 6 were synthesized by this technique.

Ion Beam Etching. If the Kaufman ion source is installed in the spot of Preclean and Assist Ion Source and in operation, the ion beam can be used to etch the

substrate. This approach is called ion beam etching which is used to fabricate diamond nanotips as will be discussed in Chapter 7.

Ion Beam Deposition. In ion beam deposition mode, the end-Hall ion source is installed in the spot of Preclean and Assist Ion Source instead of Kaufman ion source. Precursor gas (CH_4/Ar in this study) is introduced into the ion source and ionized into free carbon radicals. The carbon radicals can react and deposit onto the substrate as thin films. This technique is used to deposit amorphous carbon which will be discussed in Chapter 8.

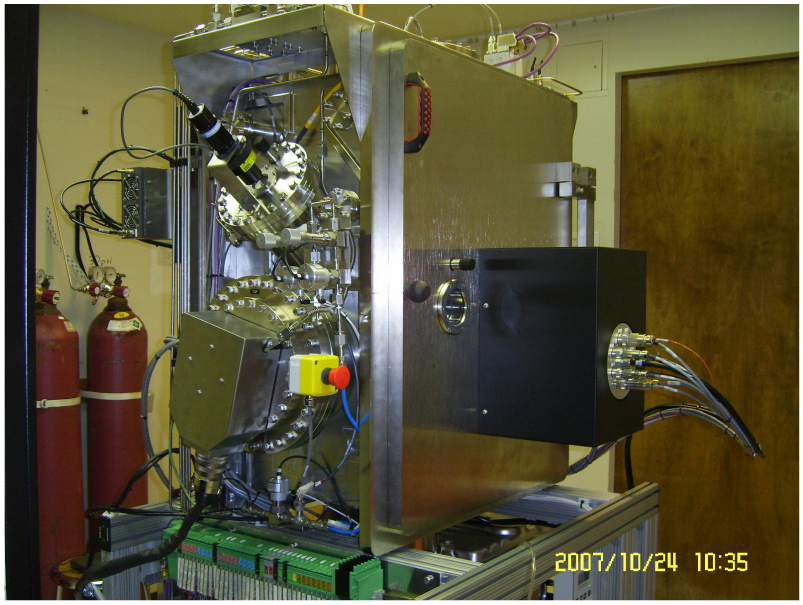

(a)

(b)

Figure 2.3. Pictures of the ion beam system, (a) vacuum chamber and (b) control system and power supply.

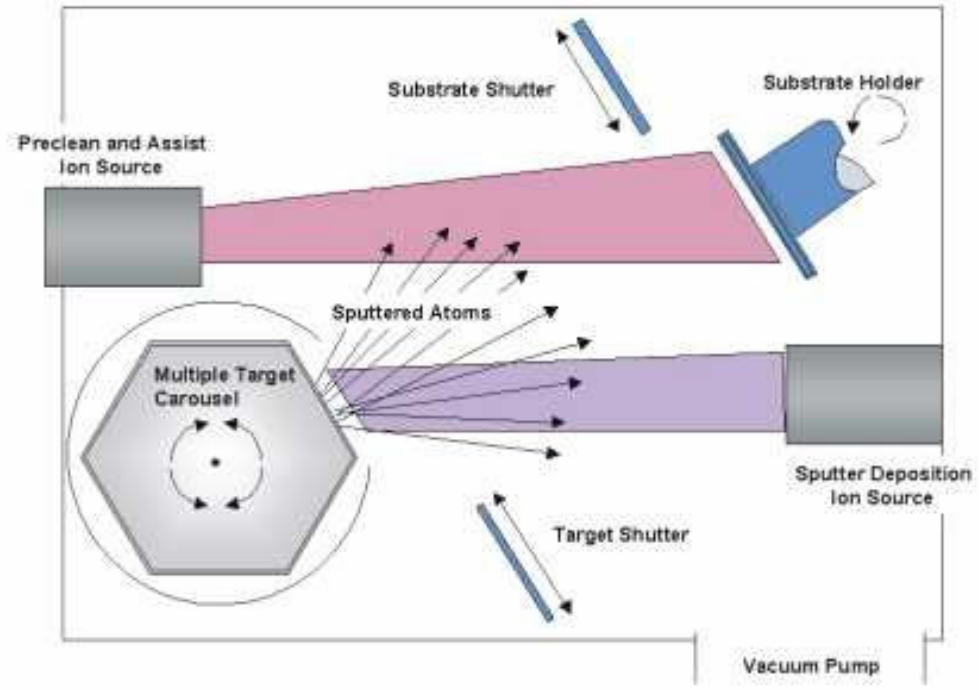

Figure 2.4. A schematic diagram of the configuration of ion beam system [http://www.4waveinc.com/ibd.html].

2.2 Characterization Techniques

2.2.1 SEM

Scanning electron microscopy (SEM) is one of the most versatile techniques to characterize the surface morphology and chemical composition of materials. SEM employs electron beams as radiation source and magnetic coils to focus electron beams on sample surfaces. SEM can generate images with high resolution down to a few nanometers, compared to several hundred nanometers for optical microscopes.

There are several kinds of signals that can be generated from the interaction of electron beam and materials surface as shown in Figure 2.5. Those signals include X-rays, Auger electrons, secondary electrons (SE), backscattered electrons (BSE) and so on.

When an electron is ejected from a core level of an atom, leaving a vacancy, an electron from a higher energy level may fall into the vacancy, resulting in a release of energy. This energy can be released in the form of photon, which is X-ray fluorescence. The energy can also be transferred to another electron, which is ejected from the atom. This second ejected electron is called an Auger electron.

Incident electrons that are elastically scattered by specimen atomic nucleus or outer shell electrons through an angle of more than 90° are called backscattered electrons (BSE). The BSE signal intensity is strongly dependent on specimen's nuclear structure (or atomic number). Thus, the BSE mode of SEM image yields atomic number contrast of the specimen.

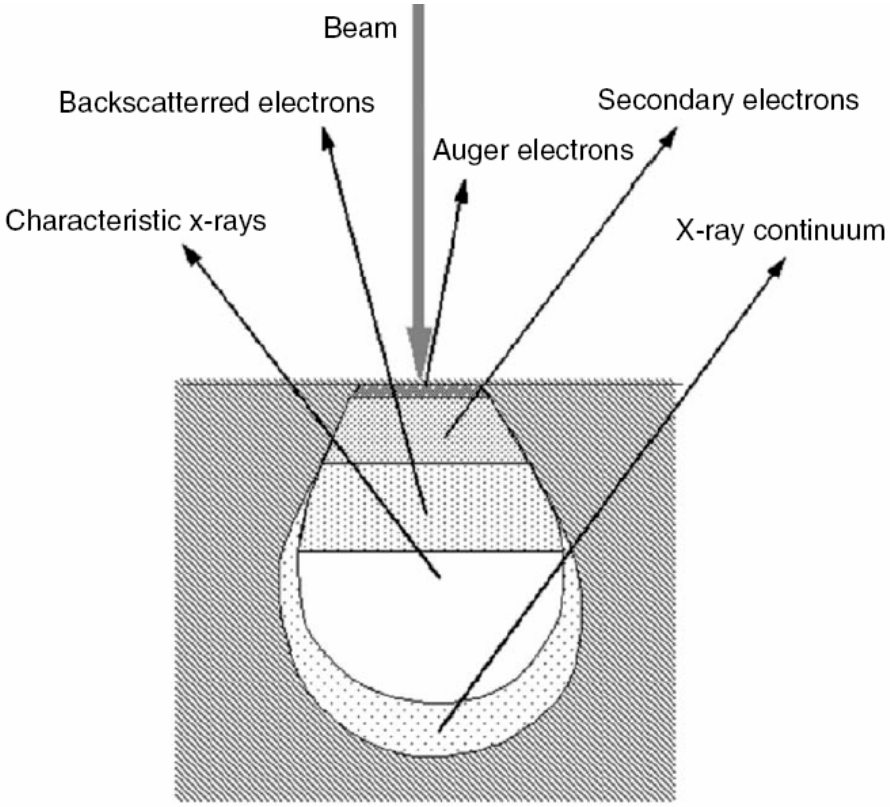

Figure 2.5. Illustration of signals generated by ion beam-specimen interaction in SEM [Zhou *et al*., 2005].

When the primary beam strikes the sample surface causing the ionization of specimen atoms, loosely bound electrons may be emitted and these are called secondary electrons (SE). As the electrons are at low energy, typically a few eV, they can only escape from regions of several nanometers from the materials surface. Therefore, SE can accurately mark the position of the beam and give topographic information with good resolution. Thus, the SE mode of SEM is often used to examine the topography of materials surface.

In this thesis, a JEOL 840A SEM with a maximum resolution of 10 nm (located in the Department of Geological Science, University of Saskatchewan) was used to characterize the surface morphology of the samples.

2.2.2 AFM

AFM and scanning tunneling microscopy (STM) are the two forms of scanning probe microscopy (SPM) where a small probe scans across the sample to obtain information about the surface. AFM was invented to overcome some drawbacks of STM, such as requiring ultra high vacuum and only imaging conducting or semiconducting surfaces. AFM can work under ambient conditions and can image almost any type of surfaces, including polymers, ceramics and biological samples. Typically, lateral resolution of <1 nm and height resolution of < 0.1 nm can be obtained by AFM.

AFM has a cantilever with a sharp tip (probe) at its end that is used to scan material surface as shown in Figure 2.6. The tip and cantilever are fabricated from Si or Si_3N_4. Typical tip radius is from a few to tens of nm. When the tip approaches the proximity of the sample surface, the cantilever deflects due to the forces between the tip and the sample. Depending on the circumstances, the forces can be mechanical contact force, van der Waals forces, capillary forces, chemical bonding, electrostatic forces, or magnetic forces. The deflection of cantilever is measured by a laser spot reflected from the top surface of the cantilever into a position-sensitive detector. The force can be determined from the deflection of cantilever with Hook's Law.

AFM can work in different modes. The most widely used mode is contact mode. The AFM probe scans at a constant force within a distance very close to the sample surface. When the probe cantilever is deflected by topographical changes, the scanner adjusts the probe position to restore the original cantilever deflection. The scanner position information is collected as data to create a topographical image. Contact mode is commonly used for rigid surfaces. To image soft samples or absorbed layers on sample surfaces, the second mode, non-contact mode, can be used. In non-contact mode, the tip interacts with the surface with van der Waals force or any other long range force which extends well above the surface. In the third mode, the probe tip is scanned at a height where it barely touches or "taps" the sample surface. This mode is called tapping mode. In tapping mode, lateral forces such as drag, common in contact mode, can be eliminated, which results in higher lateral resolution than contact mode.

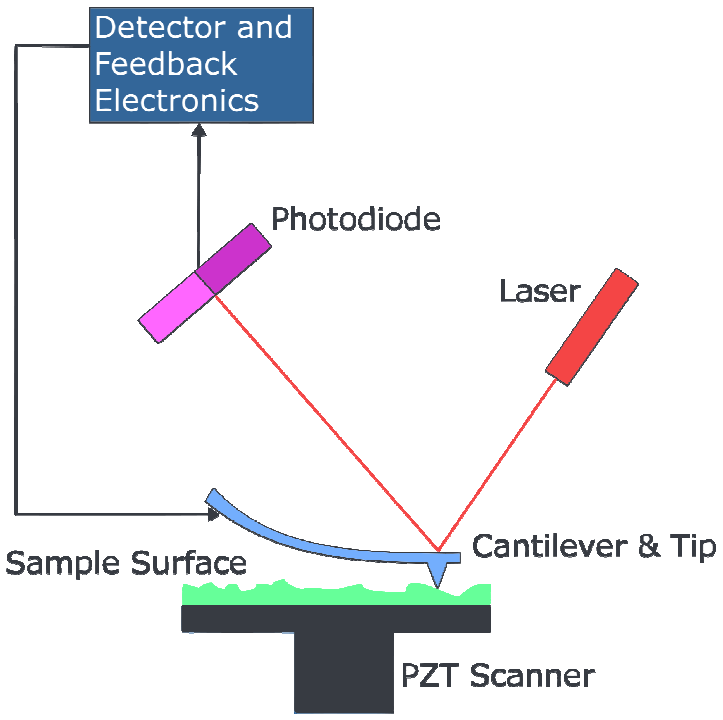

Figure 2.6. Schematic of the work principle of AFM.

The AFM analysis contained in this thesis was done using a NanoAnalyser manufactured by Center for Tribology Inc. USA. NanoAnalyzer is an AFM that works in contact mode. The NanoAnalyzer uses piezoresonance probe with high bending stiffness of the cantilever. High bending stiffness of the cantilever allows the tip to go through the absorbed layers and contact the elastic surface, making nano-indentation, nano-scratch and elastic modulus measurement.

Nano-scratch can be used to measure the hardness of materials. The procedure and principle are briefly described as follows with the example of nano-scratch on polymer coated Si. First, use the tip to scratch the reference sample of known

hardness (fused silica, usually) and testing sample. Figure 2.7 shows an AFM image of 3 nano-scratches at 500, 200 and 100 μN (left to right) on polymer coated Si by NanoAnalyzer [*Gitis et al.*, 2008]. Then scan the surface to find out the scratch widths. Figure 2.8 shows the scratch depth profiles of 3 scratches along xx in Fig 2.7 [*Gitis et al.*, 2008]. The hardness can be calculated using the following equation (2.1),

$$H_S = H_R \frac{F_S}{F_R}(\frac{W_R}{W_S})^2 \tag{2.1}$$

where H_S is hardness of the sample; H_R is hardness of reference materials; W_R and W_S are the scratch width on reference and on testing sample; F_R and F_S are the scratch load on the reference and on the testing sample [*Gitis et al.*, 2008]. Compared with frequently used nano-indentation for hardness measurement, nano-scratch [*Tayebi et al*., 2004] yields more reliable hardness results for thin films because of much less substrate effect. In addition, nano-scratch obtains data from a lateral length of several to hundreds of micrometers, which averages any inhomogeneities such as surface roughness and phase/composition variation. The NanoAnalyzer can also measure elastic modulus by monitoring the change of amplitude and frequency with load at the probe tip during the tip-surface interaction. This technique again is much less affected by substrate as compared to nano-indentation.

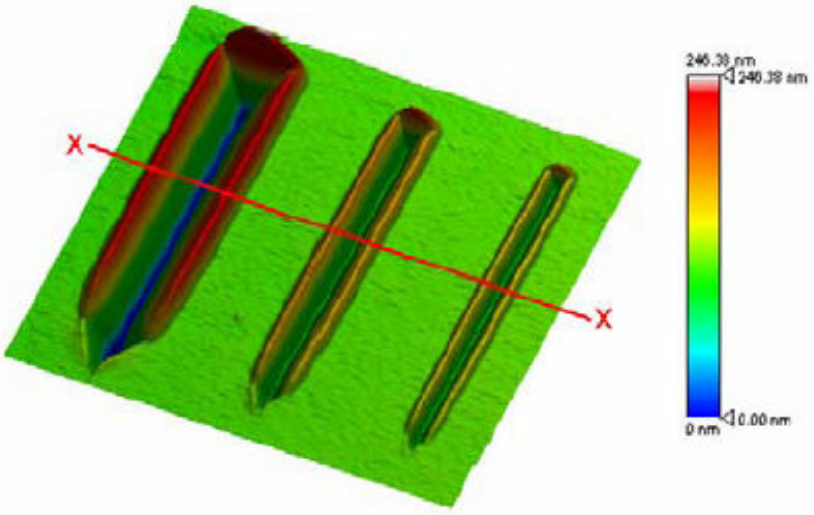

Figure 2.7. AFM image of 3 nano-scratches at 500, 200 and 100 μN (left to right) on polymer coated Si using NanoAnalyzer [*Gitis et al.*, 2008].

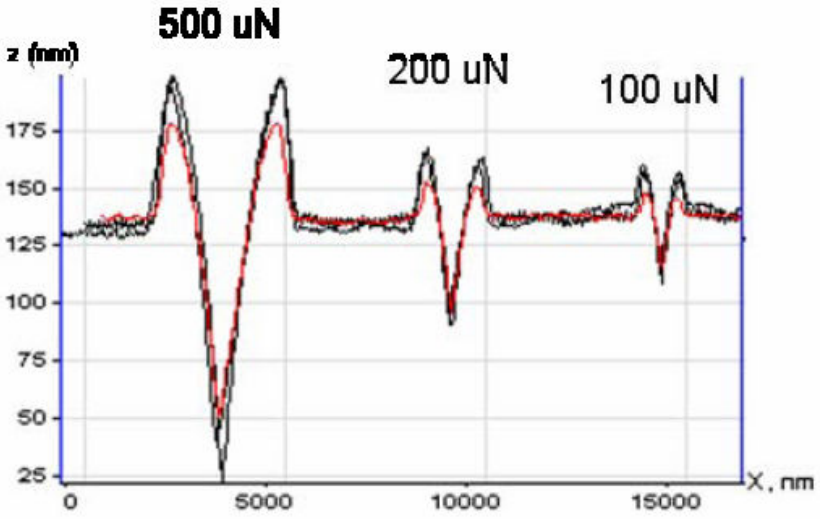

Figure 2.8. Scratch depth profiles of 3 scratches along xx in Figure 2.7 [*Gitis et al.*, 2008].

2.2.3 Raman Spectroscopy

When light is scattered by a molecule, most photons are elastically scattered and have the same energy as incident photons. However, a small fraction of light (approximately 1 in 10^7 photons) is inelastically scattered and have an energy value different from that of the incident photons. The process leading to this inelastic scattering is called Raman effect. The difference in energy between the incident photon and the Raman scattered photon is equal to the vibration energy of the scattering molecule. A plot of intensity of scattered light versus energy difference is a Raman spectrum. The spectra of two molecules are different, if these molecules have different constitutions, isotopic distributions, configurations, conformations or if their environment are different. The spectra show certain bands of characteristic vibrations. Therefore, definite substances can be identified from their Raman spectra, interpreted like fingerprints.

The main application of Raman spectroscopy in inorganic chemistry is the qualitative and quantitative analysis of known substances. The interpretation of Raman spectra involves comparing the measured spectra with reference spectra in databases by aid of certain software. Definite substances can be qualitatively identified from their characteristic peaks in the spectra. For example, natural diamond exhibits a sharp first order peak at ~1333 cm^{-1} and a weak second order feature at ~2750 cm^{-1} in the Raman spectrum. The concentration of different components of a mixture can also be quantitatively analyzed. In the cases that the components have the same Raman scattering efficiency, the area of the band is proportional to the concentration of the species.

In this thesis, the Raman spectra of diamond were obtained using a Renishaw micro-Raman system 2000 spectrometers operated at a laser wavelength of 514.5 nm generated by an argon laser. The spot size was approximately 2 μm.

2.2.4 XRD

X-ray diffraction (XRD) is a non-destructive technique that reveals detailed information about the chemical composition and crystallographic structure of crystalline materials. The spacing between crystalline planes of regular crystals is in the same order of the wavelength of X-ray, therefore diffractions could occur when a monochromatic X-ray beam is projected onto a crystalline material. The interference of X-rays scattered by crystals can be explained by Bragg's Law. As schematized in Figure 2.9, wave 1 and 2 of an X-ray beam with the wavelength of λ is scattered by a crystal. The path difference between the waves reflected by two neighboring lattice planes can be written as (AB+BC), or $2d\sin\theta$, where d is the spacing between the lattice planes and θ is the angle between the incident beam and the planes. If the path difference is an integer multiple of the incident wavelength, $2d\sin\theta=n\lambda$, constructive interferences will occur and result in diffraction peaks.

By varying the incident angle θ, the Bragg's Law conditions are satisfied by different d-spacings in polycrystalline materials. Plotting the angular positions and intensities of the resultant diffracted peaks of radiation produces a pattern, or XRD, which is characteristic of a crystalline phase. Where a mixture of different phases is present, the resultant pattern is formed by addition of the individual patterns.

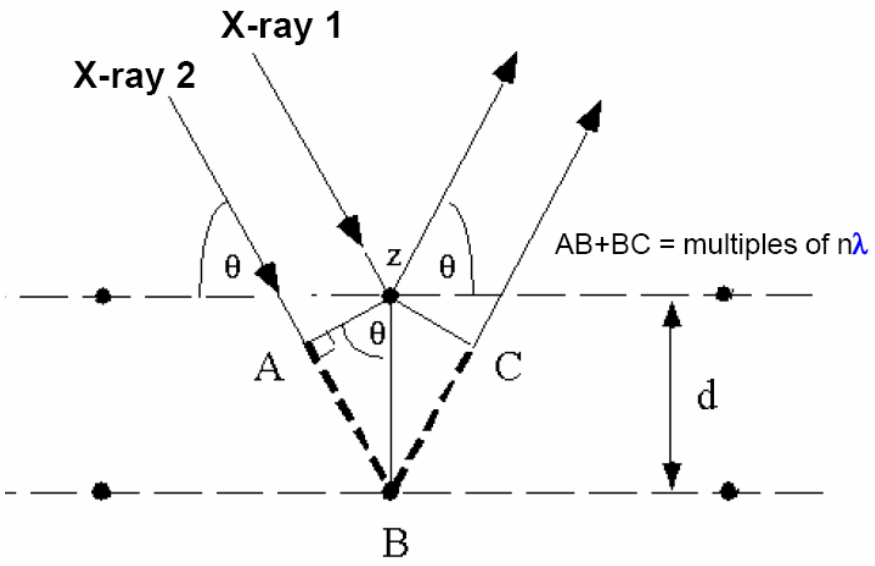

Figure 2.9. A schematic diagram of Bragg's Law.

Powder XRD is commonly used to identify phases in a sample, by comparing diffraction data against XRD database. Powder diffraction is also a common method for determining grain size in crystalline materials. An effect of the finite crystallite sizes is seen as a broadening of the peaks in an X-ray diffraction as is explained by the Debye-Scherrer's Equation (2.2) [*Patterson*, 1939] which can be written as

$$\tau = \frac{K\lambda}{\beta \cos\theta} \tag{2.2}$$

where τ is the mean size of the ordered (crystalline) domains, K is the shape factor, and β is the line broadening at half the maximum intensity (FWHM) in radians.

The Debye-Scherrer's equation is limited to nano-scale particles. It is not applicable to grains larger than about 0.1 μm. It is also important to realize that the Debye-Scherrer's formula provides a lower bound on the particle size because a variety of

factors besides particle size, such as inhomogeneous strain and instrumental effects can contribute to the width of a diffraction peak.

XRD patterns in this thesis were measured by a Rigaku (Rotaflex Ru-200) diffractometer which uses X-rays of the Cu *K*α line (λ=0.15418 nm), produced by impinging an 80 kV, 40 mA electron beam on a Cu target. The sample and the detector are mounted on two separate rotating bases, when the sample rotates an angle θ, the detector rotates an angle 2θ.

2.2.5 XPS

X-ray Photoelectron Spectroscopy (XPS) is also known as electron spectroscopy for chemical analysis (ESCA). A sample surface is irradiated with soft X-rays photons (1-2 keV) to excite the inner shell electrons of target atoms to induce direct emission of photoelectrons. As each element has it own core level, the binding energy of the peaks are characteristic of each element. The fraction of each element is proportional to peak areas, which can be used to determine the composition of the materials surface.

XPS also gives information about the chemical bonding state of each element by measuring the shifts of core level. The shifts are mainly caused by the Coulombic potential from ionic charges of adjacent atoms. For instance, C 1s has a core level shift of proximately 0.9 eV between diamond and graphite due to the different bond length of sp^2 and sp^3 carbon. XPS is a surface sensitive technique because only those photoelectrons from the top 2-20 atomic layers, depending on the material, can escape and be detected.

In this study, the composition and element bonding states of amorphous carbon films was studied by XPS. All XPS measurements were performed on Kratos Axis 165 spectrometer with a monochromatic Al *K*α x-ray source and a base pressure in the analytical chamber of 10^{-6}-10^{-7} Pa. The resolution of the instrument is 0.4-0.5 eV.

2.2.6 Synchrotron based NEXAFS

When electrons are accelerated, linearly or centripetally, they emit electromagnetic radiation. In synchrotron radiation, relativistic charged particles (moving at a velocity near the speed of light) circulate in the storage ring. Due to periodic acceleration in special insertion device magnets, such as undulators and wigglers, the path of charged particles is bent (accelerated) and radiation is produced. The radiation may range over the entire electromagnetic spectrum, from radio waves, to infrared light, visible light, ultraviolet light, X-rays and gamma rays. Synchrotron radiations have high brightness which is orders of magnitude brighter than optical sources. Synchrotron can produce a smooth spectrum of energies with high energy resolution. When a beam of monochromatic X-ray produced by synchrotron is projected on a material, it loses its intensity due to the interaction with atoms in the material. As shown in Figure 2.10, an X-ray beam with proper range of energy can excite inner core level electrons to emit photoelectrons, Auger electrons and fluorescence. By tuning the photon energy of X-ray beam using a monochromator and collecting the data of electron/fluorescence emission, X-ray absorption spectroscopy (XAS) can be obtained as shown in Figure 2.11. XAS is used to probe the local unoccupied electronic density of states in an atom.

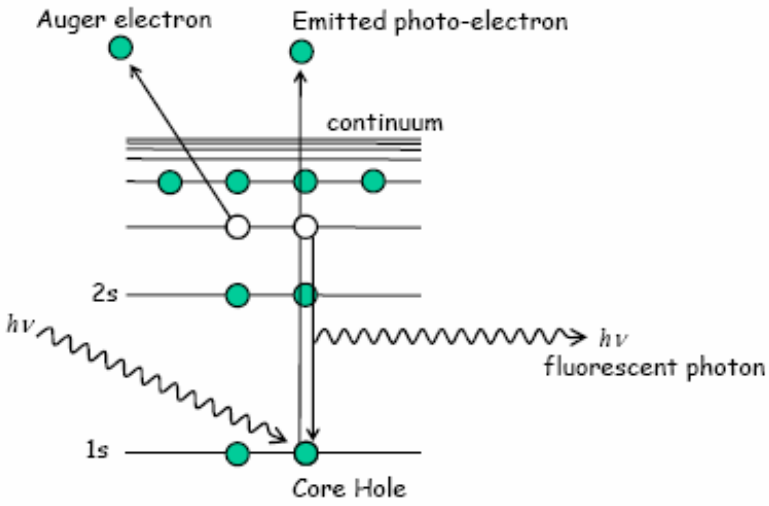

Figure 2.10. A schematic diagram of electron-transitions that occur when an X-ray beam is incident on a material [George and Pickering, 2006].

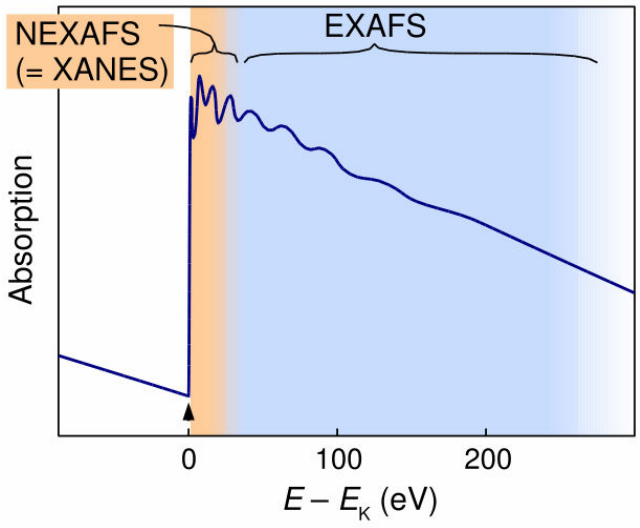

Figure 2.11. A schematic diagram of X-ray absorption spectrum with NEXAFS and EXAFS two regions [http://commons.wikimedia.org].

The X-ray absorption spectra show a steep rise at the absorption edge and then attenuate gradually with the X-ray energy. The region within ~50 eV of the absorption edge is called near edge X-ray absorption fine structure (NEXAFS or

XANES). NEXAFS is very sensitive to the chemical state, such as the oxidation state and local geometry of the absorbing atom. It can be used as "fingerprint" to identify the presence of a particular chemical species. The oscillatory structure of the spectra extending to hundreds of eV past the edges is called extended X-ray absorption fine structure (EXAFS). EXAFS gives detailed interatomic information of the absorbing atom, such as bond-lengths and coordination numbers. The regions of NEXAFS and EXAFS in a typical XAS spectrum are shown in Figure 2.11.

XAS data can be collected mainly by three ways: transmittance, fluorescence yield (FLY) and total electron yield (TEY). Transmittance is a relatively simple experimental technique which uses ion chamber detectors to detect the intensity of incident (I_0) and transmitted (I) X-rays. The absorbance, $A = \mu x$, can be written as $\mu x = \ln(\frac{I_0}{I})$ where μ is the absorption coefficient, and x the sample thickness. Transmittance is only useful for concentrated samples. For dilute samples, FLY is commonly used. FLY measures fluorescent photons emitted from the sample. The number of fluorescence photons is proportional to the number of absorbed photons of X-ray. FLY is relatively bulk sensitive. For carbon K-edge, the sensitivity range of FLY is proximately 100 nm. In TEY mode, the total number of electrons escaping from the sample is counted including photoelectrons and Auger electrons. The total number of escaped electrons is closely related to the absorption process and thus can be used to represent the absorption spectrum. Due to the low energy of photoelectrons and Auger electrons, TEY mode is surface sensitive giving information ranging from 2-10 nm in the surface.

The NEXAFS experiments were performed using the high resolution Spherical Grating Monochromator (SGM) beamline at the Canadian Light Source Inc. (CLS), University of Saskatchewan. The spectra were recorded in total electron yield (TEY) mode by monitoring the sample current.

2.2.7 Friction Measurement

Friction is the resistance to motion during sliding or rolling that is experienced when one solid body moves tangentially over another with which it is in contact. The resistive tangential force, which acts directly opposite to the direction of motion, is called the friction force. There are two main kinds of friction: dry friction and fluid friction.

Dry friction, also known as Coulomb friction, describes the tangential component of the contact force that exists when two dry surfaces move or tend to move relative to one another. When two nominally flat surfaces are placed in contact under load, the real contact happens at the tips of the asperities. The sum of the areas of all the contact spots constitutes the real area of contact. The real contact area is only a small fraction of the apparent (nominal) area of contact. The high stress on the contact spots results in the deformation of the asperities and even adhesive bonds. When two surfaces move relative to each other, a frictional energy (or force) is required to shear the adhesive bonds formed at the interface. In addition, energy is required for microscale deformation of the contacting surfaces during relative motion.

Fluid friction describes the tangential component of the contact force that exists between adjacent layers in a fluid that are moving relative to each other as in a liquid

or gas between bearing surfaces. With the presence of a thin liquid film with a small contact angle such as lubricant or adsorbed water layer at the contact interface, curved menisci form around contacting and non-contacting asperities due to surface energy effects. The attractive meniscus force arises from the negative Laplace pressure inside the curve meniscus as a result of surface tension. Therefore, the total normal force on the wet interface is the externally applied normal force plus the intrinsic meniscus force.

Figure 2.12 shows a schematic diagram of ball-on-flat sliding test. The coefficient of friction is calculated from the ratio of friction force to applied normal load. The stationary specimen of the material pair is mounted on a sample stage, and the flexible one is mounted on a movable head. When certain load is applied the sliding is initiated, a strain-gage transducer is used to measure the frictional force. Under some circumstances, piezoelectric force transducers are used for dynamic frictional force measurements.

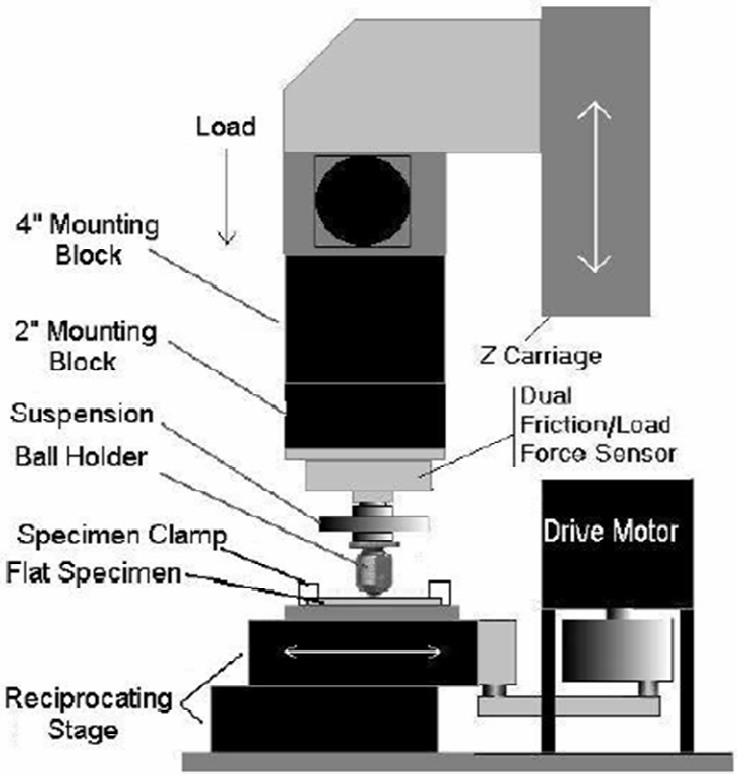

Figure 2.12. A schematic diagram of ball-on-flat sliding test [*Multi-Specimen Test System User's Manual, CETR*, 2004].

CHAPTER 3
DEPOSITION AND CHARACTERIZATION OF DIAMOND COATINGS ON WC-CO CUTTING TOOLS WITH CHEMICAL AND PLASMA PRETREATMENT*

3.1 Introduction

In order to deposit adhesive diamond coating on WC-Co cutting tools, the cutting tools need to be pretreated by chemical etching or coated with interlayer to reduce the deleterious effect of cobalt. The most widely used chemical etching reagent ($K_3Fe(CN)_6$–KOH) contains $(CN)^-$ which is extremely hazardous for human beings and the environment. It is necessary to develop a cleaner pretreatment method for the growth of adhesive diamond coatings on WC-Co. In this work, a combination of hydrochloric acid etching and H_2 plasma treatment is studied as pre-treatment to reduce surface Co concentration and modify the substrate surface morphology to increase coating adhesion.

3.2 Experimental

In order to decrease the Co content on the WC-Co surface, two methods, hydrochloric (HCl) acid etching and hydrogen (H_2) plasma treatment, were used in

* Part of this Section has been published in *Advanced Ceramic Coatings And Interfaces III Book Series: Ceramic Engineering And Science Proceedings*,

this experiment to etch Co out and modify the surface of WC-Co. For HCl etching, the WC-Co substrates were immersed in HCl solution (30% v/v) for 40 minutes to form an "etched layer" with a thickness of a few micrometers and then rinsed with deionised water. For H_2 plasma treatment, 2.45 GHz Microwave plasma CVD reactor was used. The vacuum chamber was pumped down to a pressure of 6.65×10^{-4} Pa using a turbo-molecular pump and then filled with hydrogen (H_2). The flow rate of H_2 was 100sccm. When the working pressure was stabilized at 4 kPa, a 2.45 GHz microwave source was switched on to form a plasma. The working gas pressure was maintained at 4 kPa and the microwave power at 1000 W. During the treatment, the substrates were heated only by the plasma and the substrate temperature was about 740 °C as measured with a thermocouple mounted right behind the substrate holder. The duration of treatment was 4 hours.

Three different combinations of chemical etching and plasma treatment were applied as pretreatments: (1) HCl etching, (2) H_2 plasma treatment +HCl etching, and (3) HCl etching + H_2 plasma treatment.

The synthesized materials were characterized using SEM and Raman spectroscopy. The Raman spectra were obtained by a Renishaw micro-Raman system 2000 spectrometers operated at a laser wavelength of 514.5 nm generated by an argon laser. The spot size was approximately 2 μm. The adhesion of diamond coatings on WC-Co was examined by scratch testing.

according to the Copyright Agreement of the publisher, "contributors may use the articles in teaching duties and in other works such as theses".

3.2 Results and Discussion

The surface morphologies of WC-Co substrates before and after pretreatments are shown in Figure 3.1. Figure 3.1a shows the original WC-Co surface. Grooves can be found on the surface because the cutting inserts were finished with grounding by the manufacturer. The bright phase is WC and the dark phase is Co. After HCl solution etching, as shown in Figure 3.1b, Co phase on the surface was partly etched out and the surface became roughened. Figure 3.1c shows the surface morphology of WC-Co pretreated with H_2 plasma followed by HCl etching. The surface treated by this combination has more rough WC grains than the case treated only by HCl etching. In the third pretreatment method, the sequence of the combination was changed, that is, the substrates were first treated with HCl and then with H_2 plasma. As shown in Figure 3.1d, small Co particles can be seen mostly on the WC grains. This is because Co diffused onto the surface due to the heat in the H_2 plasma treatment. All the as-deposited coatings on pretreated and non-pretreated cutting inserts were first examined by optical microscopy. It was found that all the coatings on pretreated substrates were smooth, uniform and continuous. Figure 3.2 shows the typical optical image of different WC-Co cutting inserts coated with diamond. It was also found that that the coatings on non-pretreated substrate were coarse and non-continuous.

The surface morphologies of coatings were further characterized by SEM, as shown in Figure3.3. Figure3.3a shows the materials grown on non-pretreated substrates. It can be seen that a composite of separated diamond crystals and graphite was formed on the surface. The binder phase Co is responsible for the formation of graphite.

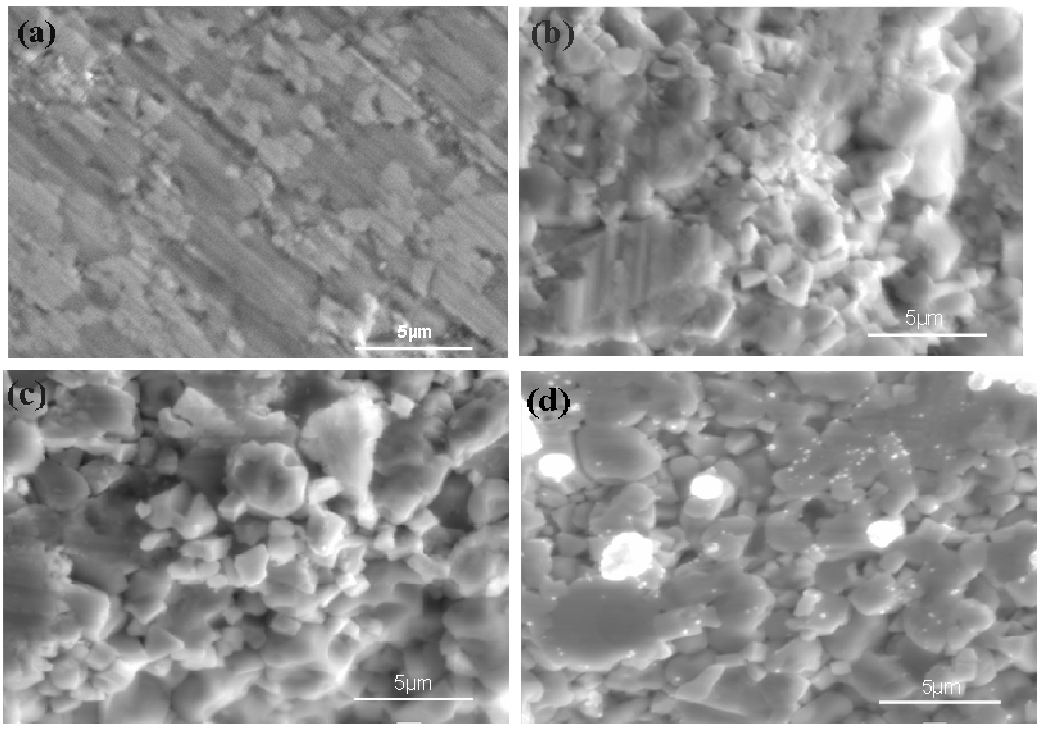

Figure 3.1. SEM surface morphologies of (a) non-pretreated and pretreated WC-Co cutting inserts with (b) HCl etching (c) H_2 plasma+ HCl etching and (d)HCl etching+ H_2 plasma.

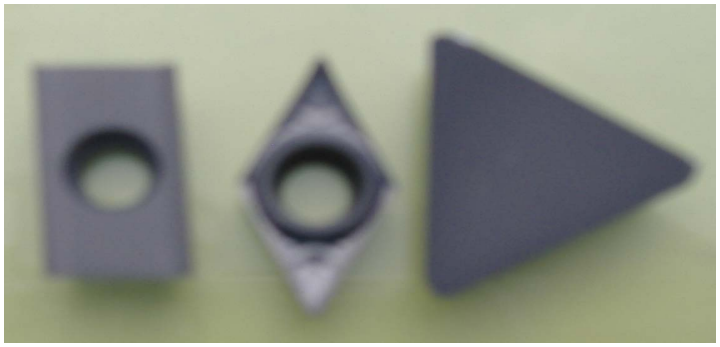

Figure 3.2. Optical image of different WC-Co cutting inserts coated with diamond.

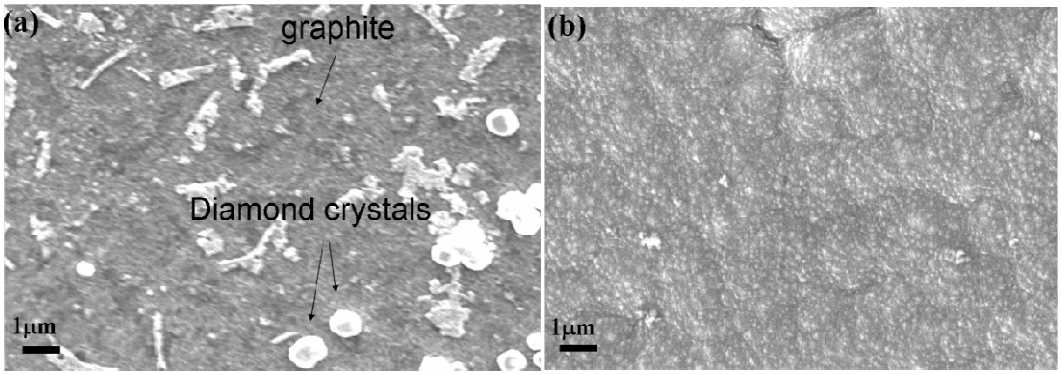

Figure 3.3. Typical SEM surface morphologies of coatings (6 hrs) on (a) untreated and (b) pretreated WC-Co substrates.

Figure3.3b shows the typical surface morphology of the coating grown on pretreated substrates. It is evident that continuous nanocrystalline diamond coatings were formed on pretreated substrates.

Coating adhesion is a main concern in the application of diamond on WC-Co cutting inserts. Scratch testing was chosen to evaluate the adhesion between the coating and substrate, since it has been proved to be the most practical method for evaluating the adhesion of hard, thin coatings [*Steinmann et al.*, 1989, *Ollendorf et al.*, 1999]. In this experiment, scratch testing of the diamond coatings on pretreated substrates was performed with a Universal Micro/Nano Testing system. In the scratch test, the normal load applied on the indenter was linearly increased from zero to 500 N. The system was equipped with acoustic emission (AE), electrical resistance (R), and friction coefficient (f) sensors to detect film spalling. There was no evidence of coating detachment up to 500 N normal loads from the AE, R or f diagram. The surface morphology of scratched diamond coatings was examined with SEM as shown in Figure 3.4: 4a with lower magnification and 4b with higher magnification.

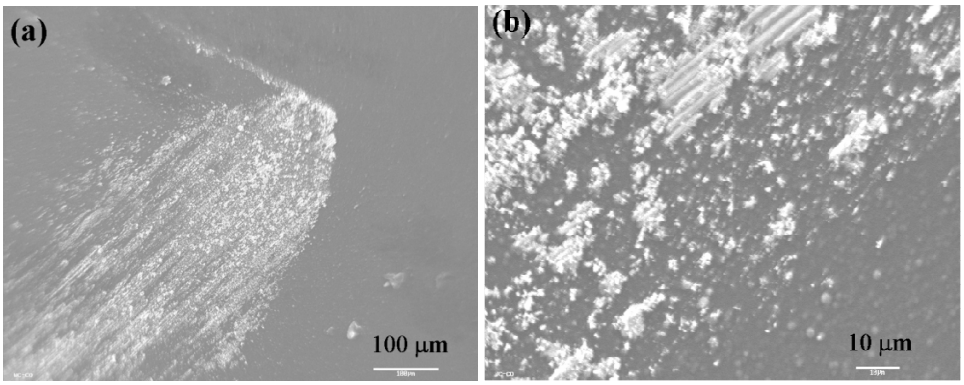

Figure 3.4. SEM surface morphologies of diamond coatings on pretreated substrate after scratching test.

It can be seen that there was no coating detachment along the scratching track during scratch testing, which indicates a good adhesion.

Figure 3.5 shows the Raman spectra of diamond coatings on pretreated and non-pretreated substrates. Characteristic peak of diamond at about 1332 cm^{-1} can be clearly seen in all pretreated WC-Co substrates. The spectra also show a broad peak around 1580 cm^{-1}. Considering the fact that Raman scattering in the visible range (514 nm) is up to 233 times more sensitive to sp^2-bonded carbon than to sp^3-bonded carbon [*Sails et al., 1996*], the coatings on pretreated substrates have high content of diamond. Comparing the spectra of samples with different pretreatments, one can find that the diamond coating on H_2+HCl pretreated substrate has the sharpest diamond characteristic peak, which indicates highest diamond content. HCl and HCl+H_2 pretreated samples have comparable diamond content. The diamond peak of non-pretreated samples is rather weak and graphite peaks are strong. It indicates that the coating has high content of non-diamond carbon.

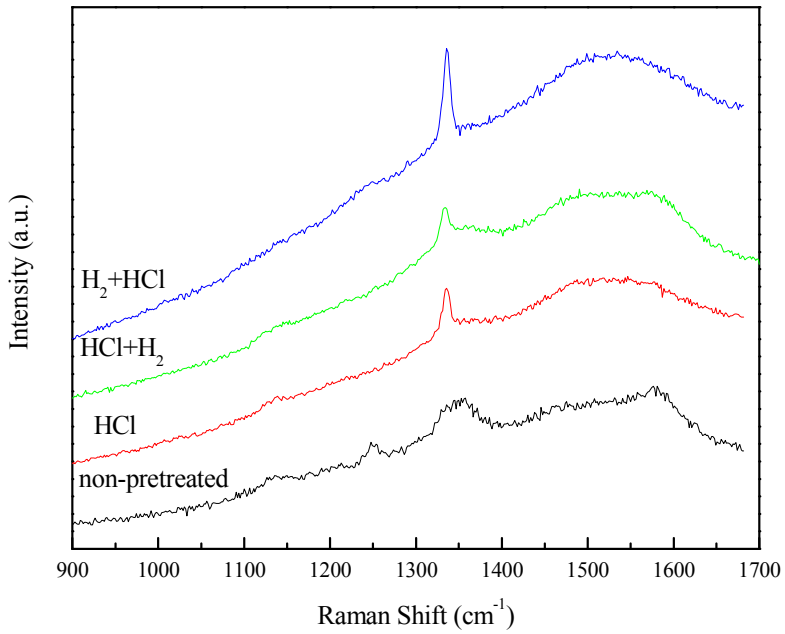

Figure 3.5. Raman spectra of diamond coatings on pretreated and untreated substrates.

From the results, it can be obviously seen that the three pretreatments, HCl, HCl+H_2, and H_2+HCl, are all effective in improving the diamond phase content and coating adhesion. Hydrochloride solution as a strong acid reacts and etches out the Co binder phase on the substrate surface. Then the graphite forming reaction induced by Co is restricted. Hydrogen plasma pretreatment has two effects on WC-Co substrates according to the research by Li *et al*. [*Li et al.*, 2006]. One is that the heating of H_2 plasma results in the growth of WC crystal grains. The coarsening of WC grains roughens substrate surface, which increases the actual contact area of coating/substrate and improves the adhesion of diamond coatings. However, coarsening of WC grain was not clearly evident from the SEM results in this study.

The other effect of H_2 plasma pretreatment is that H_2 plasma can decarbonize substrate surface and reduce the chemical state of tungsten. The reduced tungsten carbides then react with carbon atoms from precursor gases during the subsequent deposition. The reaction can not only result in chemical bonding between diamond coatings and substrates but also improve the diamond nucleation on WC-Co. The diamond nucleation improvement effect explains why the H_2+HCl pretreatment produces higher diamond phase content than single HCl pretreatment. However, it should be noticed that HCl+H_2 pretreatment is not as effective as H_2+HCl pretreatment. The reason may be attributed to the fact that Co atoms underneath the surface diffused out during the followed H_2 plasma treatment.

3.3 Conclusions

Diamond coatings were deposited on the WC-Co inserts by microwave plasma enhanced chemical vapour deposition. A combination of hydrochloric acid and H_2 plasma pretreatments were used to reduce surface Co concentration and modify the substrate surface morphology. The results show that the tested pretreatments were all effective in forming continuous and adhesive nanocrystalline diamond coatings, while H_2 plasma pretreatment followed with HCl etching produces the highest diamond phase content. The pretreatments may be promising replacements for the hazardous Murakami's reagent in the WC-Co pretreatment with more environmental friendly hydrochloride acid etching combined with hydrogen plasma pretreatment.

CHAPTER 4
DEPOSITION AND CHARACTERIZATION OF DIAMOND COATINGS ON WC-CO CUTTING TOOLS WITH AL INTERLAYER*

4.1 Introduction

In Chapter 3, it has been demonstrated that the combination of HCl chemical etching and H_2 plasma pretreatments is effective in forming continuous and adhesive nanocrystalline diamond coatings. Besides surface pretreatment, the approach of developing new interlayers is also explored. In this Chapter, nucleation and growth behaviors of diamond films on WC–Co cutting tool inserts will be presented for several interlayers, including Al, TiN, TiCN, Al–TiN and Al–TiCN.

4.2 Experimental

The substrate materials for diamond deposition were commercial WC–6 wt.% Co cutting tool inserts with or without pre-coated TiN and TiCN surface coatings (made by Hokkaido Sumiden Precision Industries Ltd., coatings thickness about 7 μm). In addition, an Al thin film of 50 nm in thickness was deposited on the surface of some blank WC–Co substrates, and TiN- or TiCN-precoated substrates.

---

* Part of this section has been published in *International Journal of Refractory Metals and Hard Materials*. According to the Copyright Agreement, "the authors retain the right to include the journal article, in full or in part, in a thesis or dissertation".

Diamond deposition was conducted in 2.45 GHz microwave plasma assisted CVD reactor (Plasmionique) using H_2 gas mixed with 1 vol.% CH_4 with a total flow rate of 100 sccm. The working pressure was maintained at 30 Torr. Microwave power was 1000 W. The substrate temperature was about 740 °C as measured by a thermocouple mounted underneath the stainless steel substrate holder. Morphology observation and structural identification of the diamond films were made with SEM and Raman spectrometer. An average diamond nucleation density, defined as nuclei number in unit surface area, was evaluated under SEM. The adhesion property of the diamond films to the substrates were evaluated by surface mechanical polishing, Rockwell C indentation test unit (load of 1470 N), and scratch test.

4.3 Results

4.3.1 Diamond growth on blank substrates

Figure 4.1 shows the typical surface morphology and Raman spectrum of the reaction products on the surface of the blank WC-Co substrates. After 4 h deposition, the film formed on the as-received tool substrate can be easily scratched off the substrate. The SEM surface observation (Figure 4.1a) shows that this film has a poorly packed structure consisting of small particles and nanoclusters. The Raman spectrum (Figure4.1b) reveals no clear diamond peak, but two major sp^2 bonding features (1351 cm^{-1} for D and 1580 cm^{-1} for G band), similar to the reference spectrum of an isotropic polycrystalline graphite sheet (the lower spectrum in Figure 4.1b). This phenomenon is closely associated with the catalytic role played by Co for the preferential formation of graphitic phase.

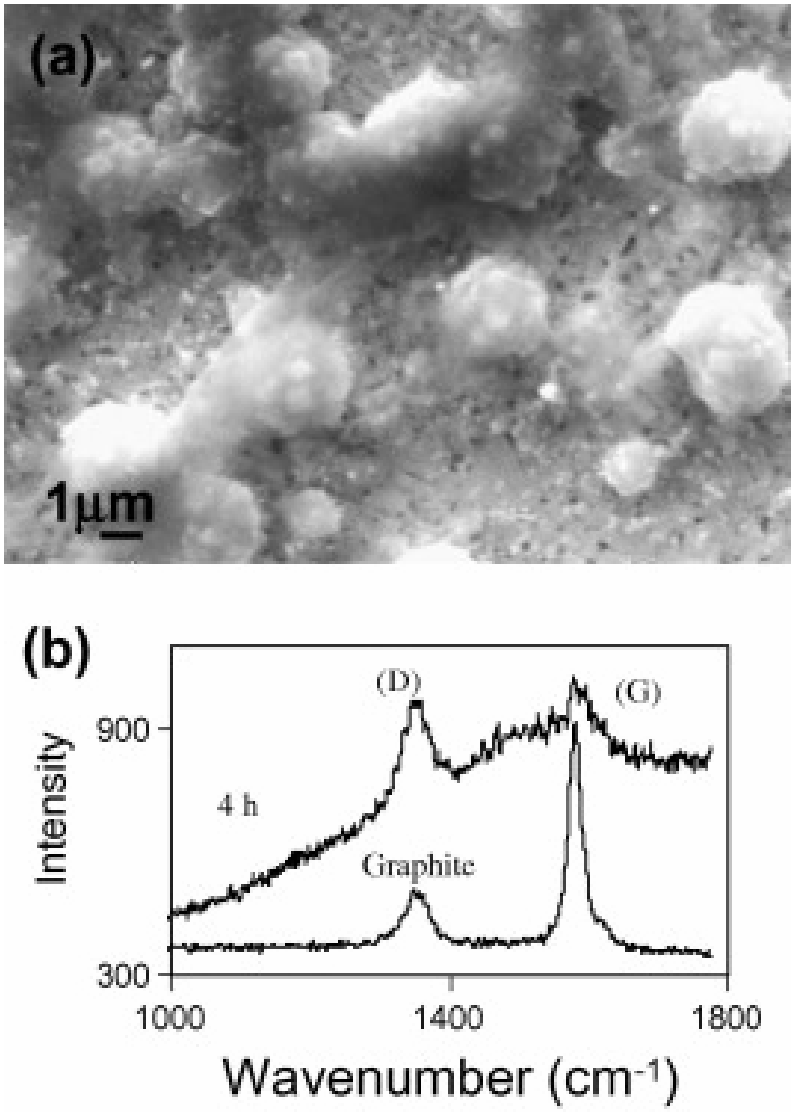

Figure 4.1. SEM image (a) and Raman spectrum (b) of diamond film deposited for 4 h on blank WC–Co substrate.

In this case, a long incubation period is needed for diamond nucleation and the nucleation density is also low. After prolonged deposition time, continuous diamond films can be developed on such substrate. However, due to the existence of this porous intermediate layer between diamond film and tool substrate, the adhesion of diamond film to the tool substrate is significantly deteriorated. For instance, local

spallation has been found at the edge of the inserts and a large area of film spallation around the imprint occurs after indentation test.

4.3.2 Diamond growth with Al, TiN, and TiCN interlayers

In order to suppress the detrimental effect of cobalt (Co) contained in the substrate, three kinds of interlayer, pure Al, TiN, and TiCN are tested. Figure 4.2a shows the surface morphology of as-sputtered Al intermediate layer. The Al film is composed of micro-clusters, each containing more fine particles in a sub-micrometric scale. The film thickness is about 50 nm. Figure 4.2b presents surface morphology of the diamond film grown for 12 h on this Al-covered tool substrate. Microcrystalline diamond film has been produced and the crystallites are densely packed, continuous without spallation. The Raman spectrum in Figure 4.2c shows a single sharp peak centered at 1338 cm^{-1}, corresponding to a diamond phase of high purity. The spallation area of diamond film around the indentation imprint is slight and much less than that deposited on blank substrates. This means that the Al interlayer has effectively improved the adhesion ability of diamond films on the WC–Co substrates.

Figure 4.3 shows the surface morphology of diamond deposited on TiCN-covered WC–Co substrates. After 4 h deposition, the film is not yet continuous and the nucleation density (particle number within unit surface area) is approximately 10^6 cm^{-2}. The corresponding Raman spectrum (Figure 4.3b) shows that the film comprises primarily diamond as confirmed by its clear and sharp characteristic peak centered at 1334 cm^{-1}. After 10 h deposition, the film becomes continuous but it is

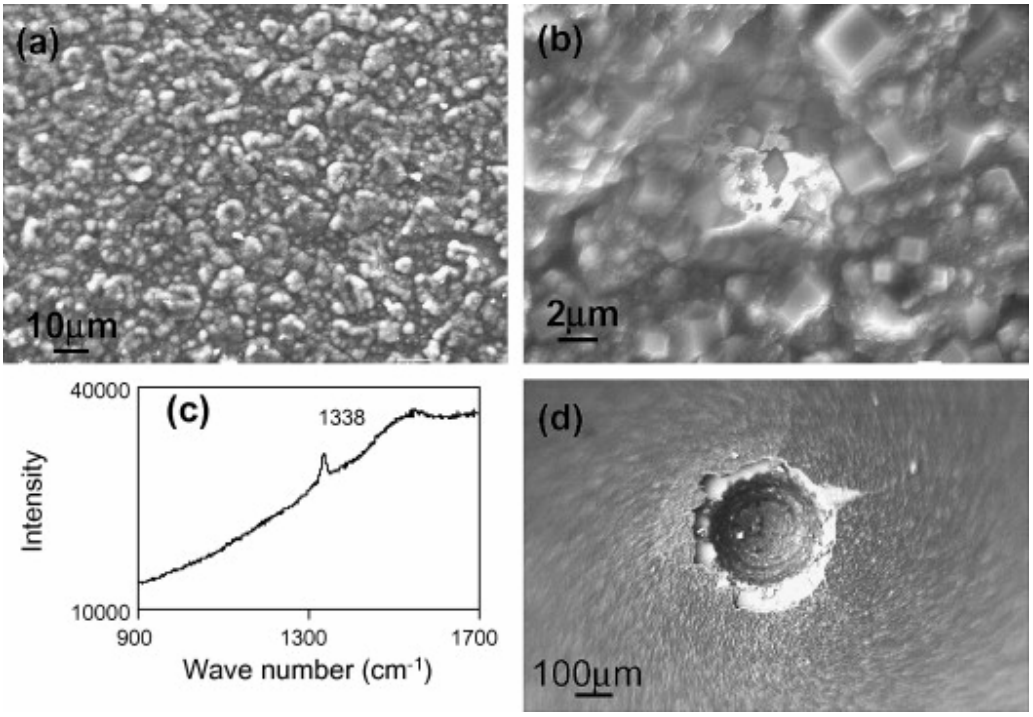

Figure 4.2. SEM images of as-coated Al interlayer (a), followed by diamond film deposition for 12 h on Al-covered WC–Co substrate (b), Raman spectrum of the diamond film (c), after indentation test of the diamond film (d).

severely wrinkled and can be easily peeled off from the substrate after cooling to room temperature.

The results demonstrate that the TiCN layer is an effective barrier to suppress catalytic effect of Co, but the nucleation density of diamond on it is low, and the bonding strength between diamond film and the intermediate layer is weak. Similar results are obtained with TiN intermediate layer.

4.3.3 Diamond growth with Al–TiN, Al–TiCN interlayers

As the Al interlayer has shown a positive effect for diamond growth on the hardmetal substrates, it is further deposited on the top of the TiN and TiCN-coated

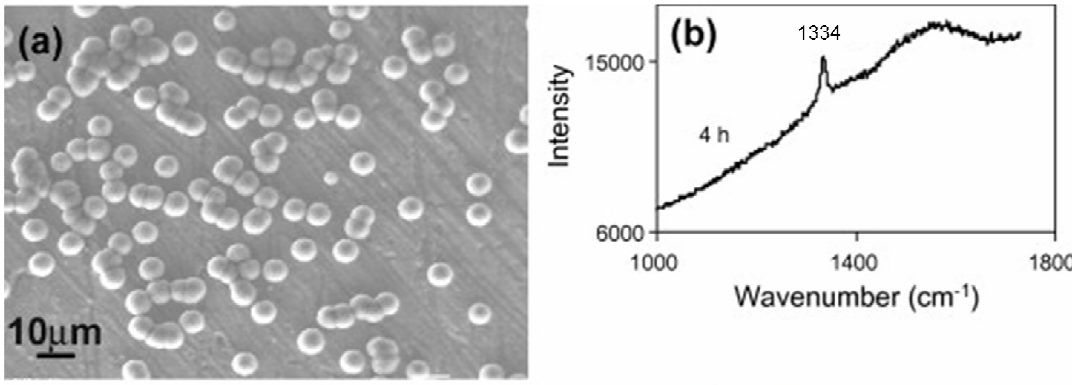

Figure 4.3. SEM image (a) and Raman spectrum (b) of diamond deposited for 4 h on TiCN-coated WC–Co substrates.

WC–Co substrates for subsequent diamond deposition. Figure 4.4 shows the results for diamond growth on WC–Co substrates with Al–TiCN interlayer. After 3 h deposition (Figure 4.4a), the nucleation density of diamond is approximately 5×10^7 cm^{-2}.With prolonged growth time for 6 h, the diamond film becomes continuous and closely packed (Figure 4.4b). The film is composed of particles in a micrometer scale which further contain finer crystallites (see insert). Raman spectrum of this diamond film (Figure 4.4c) shows that the diamond characteristic peak position is centered at 1338 cm^{-1}. In addition, two broad bands at 1140 and 1470 cm^{-1} emerge and they are related to nanocrystalline diamond. Therefore, the morphological observation and Raman spectrum confirm that fine-grained diamond films down to nano-scale have nucleated and grown on the surface of the Al interlayer film in an early stage of deposition. The diamond film with more than 6 h deposition is difficult to remove from the substrate by conventional mechanical polishing. Figure 4.5 shows surface morphology of the diamond film after being partly polished with

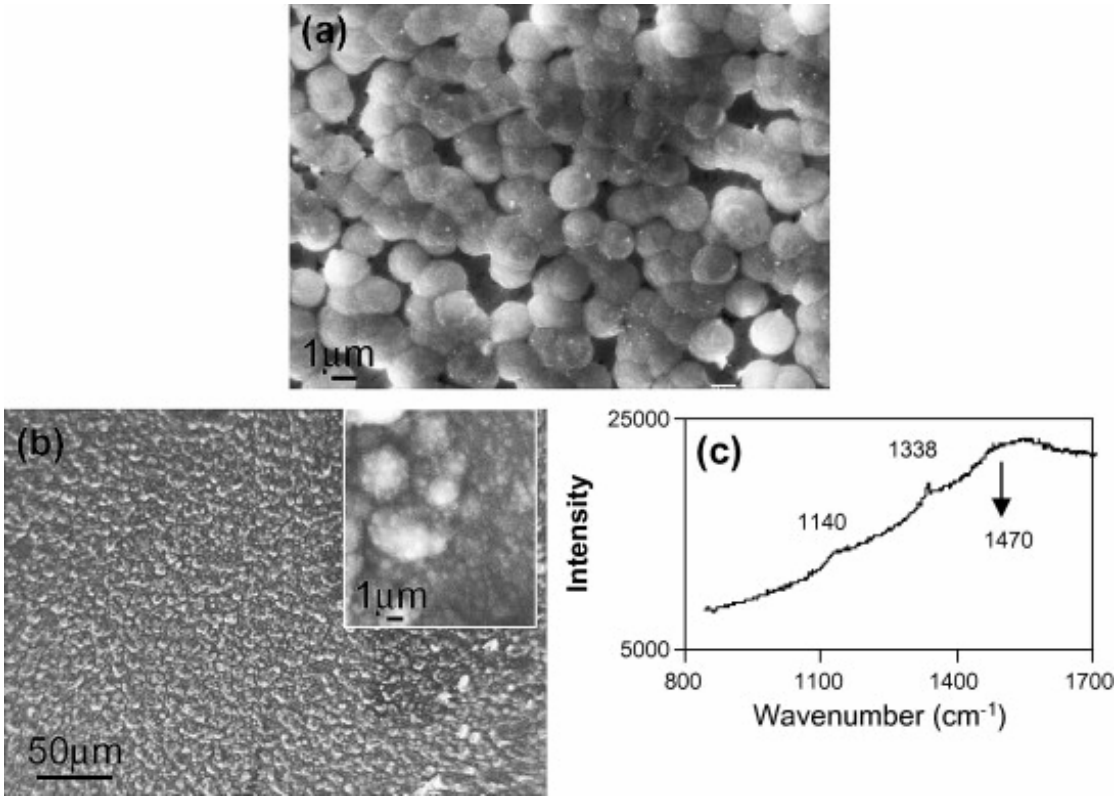

Figure 4.4. Surface images of diamond film deposited on WC–Co with Al–TiCN intermediate layer. (a) For 3 h, (b) for 6 h and (c) the corresponding Raman spectrum.

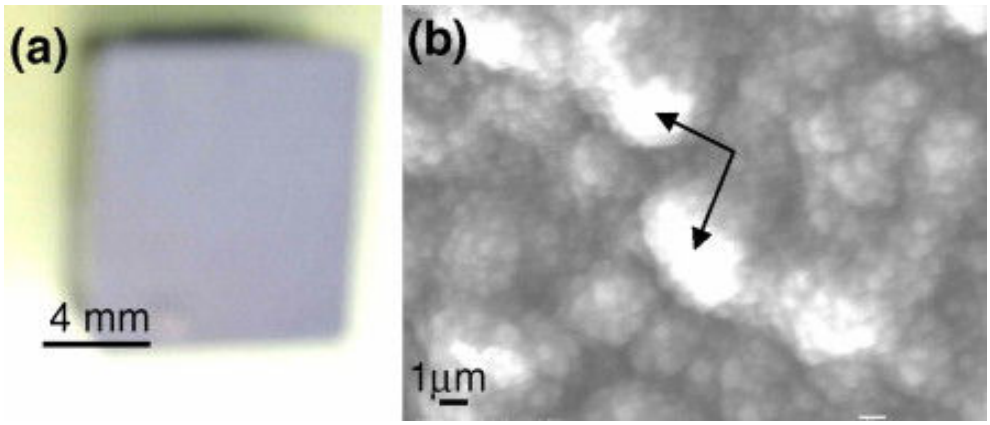

Figure 4.5. Surface images of diamond film deposited for 6 h on WC–Co with Al–TiCN intermediate layer. (a) A general view, (b) a magnified view after mechanical polishing.

#600 SiC sandpaper. Only apex of the diamond clusters is removed, as shown by arrows in the photograph, while no film spallation is detected. When the deposition time is extended to 12 h, a well-faceted microcrystalline diamond film is produced (Figure 4.6a and b). Its Raman spectrum reveals only single sharp peak at 1346 cm^{-1}, indicating high diamond phase purity. The larger upward shift of the peak position from standard one indicates increased compressive stress in the thickened film. The film still remains a high detachment tolerance. The scratch test preliminarily conducted to evaluate the adhesion ability shows that no significant failure tendency of the diamond film (such as detachment or cracking) occurs along the scratch track edges (Figure 4.6c).

In comparison with the diamond film directly deposited on TiN-coated WC–Co substrate, an additional Al layer applied on the top of TiN significantly promotes the quality of diamond film on WC–Co substrates. Figure 4.7 shows the results for diamond film coating on Al–TiN interlayered WC–Co substrates. After 12 h deposition, a continuous and densely packed microcrystalline diamond film is obtained on the substrate (Figure 4.7a). Rockwell C indentations test with a load of 1470 N results in partial spallation and cracking of diamond film around the imprint (Figure 4.7b). A magnified view of the indented area demonstrates that this indentation also causes a cracking in the underlying TiN (Figure 4.7c).

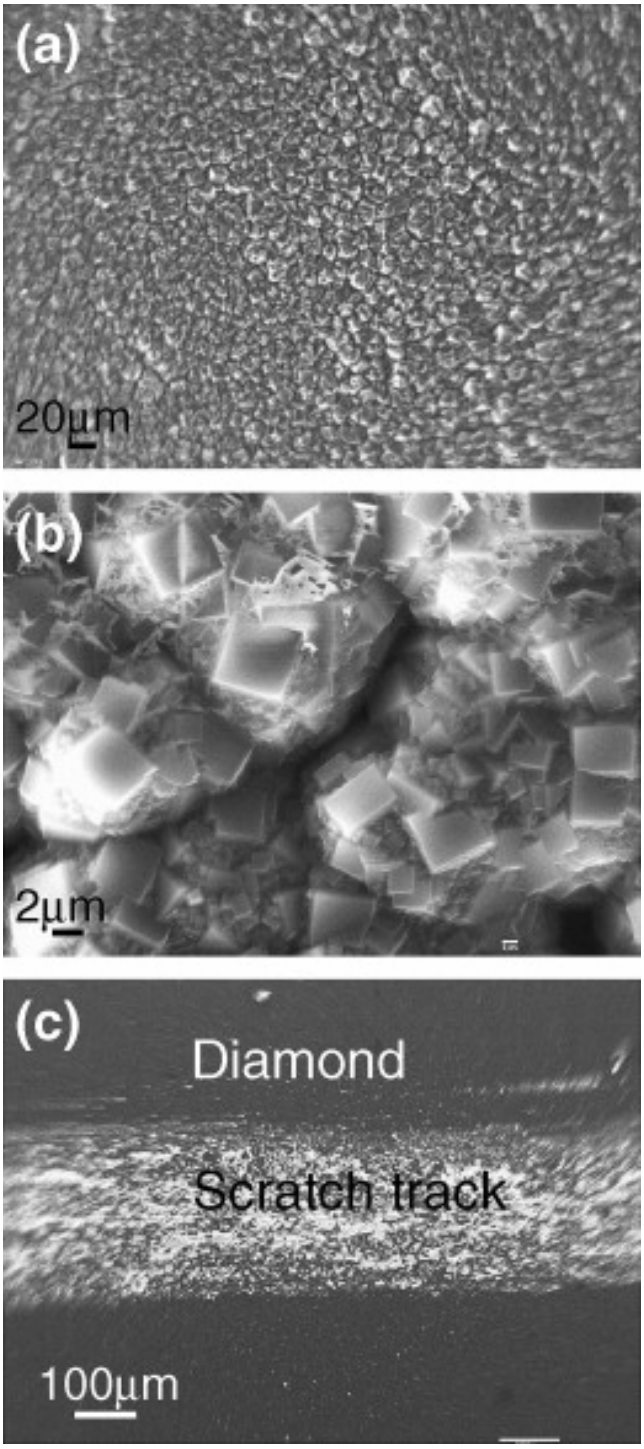

Figure 4.6. SEM images of diamond films deposited for 12 h on WC–Co substrates with Al–TiCN interlayers; (a, b) as deposited film, (c) after scratch test.

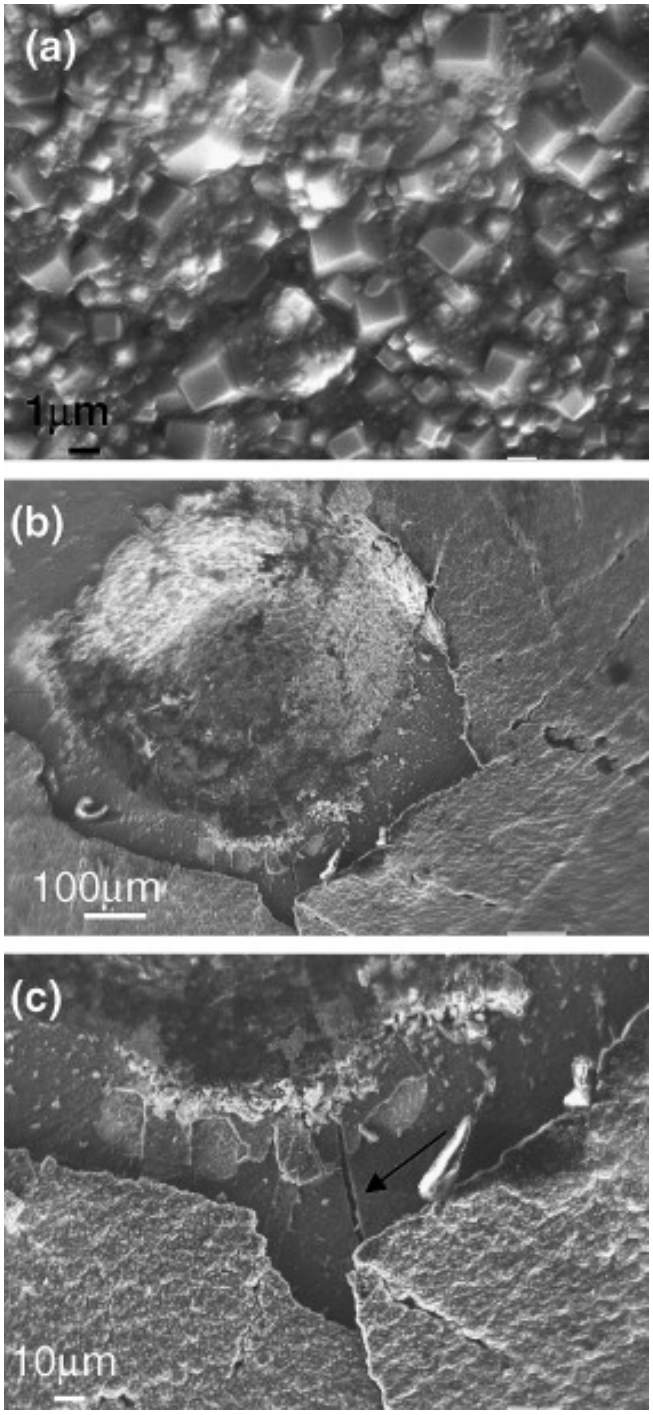

Figure 4.7. SEM images of diamond films deposited for 12 h on WC–Co substrates pre-coated with Al–TiN interlayer. (a) As deposited, (b, c) general and magnified views of diamond films after Rockwell C indentation test with a load of 1470 N.

4.4. Discussion

The results shown in Section 4.3 clearly demonstrate that as intermediate layers, Al, TiN, or TiCN on WC–Co substrates show different effects on subsequent diamond growth. An Al thin film, either directly applied to the blank WC–Co substrates, or on the top of TiN or TiCN-coated ones, has significantly promoted the nucleation and adhesion of diamond films. A possible mechanism could be primarily associated with the corresponding changes in the substrate surface conditions. For diamond deposition directly on the as-received WC–Co substrates, due to the catalytic effect from the binder phase cobalt, an intermediate layer rich in graphite is preferentially formed between diamond film and the substrate, causing weak interfacial adhesion strength. As to the diamond deposition with individual TiN or TiCN intermediate layer, although these interlayers can effectively prevent the formation of detrimental graphite at film-substrate interface, the low nucleation density of diamond on them has led to weak bonding strength between diamond film and these interlayers. In combination with the negative effect of the mismatch in thermal expansion coefficient between diamond film and tool substrate, the diamond films easily detach from the substrate upon cooling.

The beneficial effect of Al thin film on improved diamond growth can be related to the following two important factors. First, it has been known from previous studies that element Al, when alloyed to Fe-base bulk alloys, can effectively suppress the catalytic action of element Fe to form graphite [*Li and Hirose, 2007*] and [*Li and Hirose, 2006*]. Similarly, the Al thin film coated on the WC–Co substrate should dissolve into, or react with the binder phase Co during CVD process [*Kolber et al.,*

1999], thereby greatly decrease the graphitization tendency during diamond deposition process. This function of Al is especially important for diamond synthesis when Al is directly coated onto blank WC–Co substrates. Second, the fine-sized Al films have high surface energy and chemical reactivity. At the initial stage of CVD process, the aluminum crystallites are subjected to a carburization process and are possibly transformed into carbide phase like Al_4C_3 [*Liao et al., 1999*] and [*Godbole et al., 1995*]. On the one hand, the fine aluminum carbide particles can act as active sites for diamond nucleation producing a higher nucleation density, which will promote adhesion strength at diamond/substrate interface due to the increased contact area and lowered interfacial voids [*Li et al., 2006*] and [*Ternyak et al., 2005*]. This hypothesis has been partly confirmed by the experimental results obtained at different deposition periods. For instance, due to the high nucleation density promoted by the Al film, nano-scaled diamond starts to nucleate and grow at the early stage of deposition. Only after the establishment of a continuous and dense nanocrystalline diamond film, which means the continued growth of diamond is less affected by the substrate nature, will microcrystalline diamond emerge with prolonged deposition process. On the other hand, the formation of such a carbide layer in contact with the outer-most diamond film provides a stronger chemical bonding in comparison with the conventional mechanical interlocking. Similar effects have been observed when other carbide-former metals such as Ti [*Huang et al., 2007*], W [*Ralchenko et al., 1995*], Cr [*Fan et al., 2000*], and Mo [*Huang et al., 2005*] were employed as interlayers for diamond deposition. Nevertheless, a better understanding on the exact roles Al plays in the mechanism requires more related

work in the continued research, such as by using X-ray photoelectron spectroscopy to determine the chemical bonding state changes of Al before and after diamond deposition, using TEM to obtain detailed interfacial information of Al with the adjacent inner layer as well as its thickness effect.

4.5 Conclusions

The growth behavior of diamond thin films on WC–Co tool substrates have been investigated with the aid of several intermediate layers. Diamond films directly synthesized on the as-received tool substrates are of low quality associated with the formation of graphite-rich impurities at diamond film-substrate interface. TiN or TiCN thin film pre-coated on the tool substrates as barrier layer is beneficial to suppress graphite formation, but the resulting nucleation density and adhesion strength of diamond on it is low. An Al thin film applied either directly on the blank tool substrate, or on the TiN, TiCN-interlayered ones, offers enhanced nucleation density and adhesion strength for the diamond films formed on them, respectively.

CHAPTER 5
DEPOSITION AND CHARACTERIZATION OF DIAMOND COATINGS ON WC-CO CUTTING TOOLS WITH W/AL INTERLAYER*

5.1 Introduction

In Chapter 4, it has clearly been demonstrated that Al interlayer, either directly on the blank tool substrate or on the TiN, TiCN-interlayered ones, can significantly enhance nucleation density of diamond. As a result, microcrystalline diamond films can be formed on them. For cutting tools, smaller grain size of the diamond coatings enhances coating toughness and increases surface smoothness, and a smoother surface can facilitate chip evacuation and thus reduce cutting forces. Therefore nanocrystalline diamond (NCD) would offer advantages over microcrystalline diamond. In this Chapter, in order to further enhance the diamond nucleation on WC-Co for NCD growth, a new method of double interlayers W/Al is presented. A thin layer of Al deposited on WC-Co tools is used to suppress the formation of graphite catalyzed by Co and an additional thin layer of W is used to enhance diamond nucleation.

---

* Part of this section has been published on the journal of *Diamond and Related Materials*. According to the Copyright Agreement, "the authors retain the right to include the journal article, in full or in part, in a thesis or dissertation".

5.2 Experimental

The samples were prepared using two steps: (1) interlayer deposition, and (2) growth of diamond coating. Firstly, WC-Co cutting tool inserts were chemically cleaned with acetone followed by methanol, and then placed into an ion beam assisted sputtering system for interlayer deposition. Al and W targets (both having 99.99% purity) sputtered by Ar ion beam were employed to produce Al and W interlayers. The thickness was measured by a profilometer. For comparison, WC-Co with a single interlayer of W and WC-Co without interlayer were also used as substrates for the following experiments. Before CVD of diamond coatings, all the samples with or without interlayer were scratched by diamond powders in an ultrasonic bath for 120 s to increase diamond nucleation. Diamond coating deposition was conducted in a 2.45 GHz microwave plasma CVD reactor. The precursor gas mixture was CH_4 and H_2 with a flow rate of 1 sccm and 99 sccm, respectively. The working pressure was maintained at 30 Torr. Microwave power was 1000 W. The substrate temperature was about 740 ºC as measured by a thermocouple mounted underneath the stainless steel substrate holder. Five groups of samples were prepared as listed in Table 5.1. After diamond deposition, the structure and morphologies of the samples were characterized by X-ray diffraction (XRD), micro-Raman spectroscopy and scanning electron microscopy (SEM). The Raman spectrometer was operated at a laser wavelength of 514.5 nm generated by an argon laser. The adhesion of diamond coatings on WC-Co was examined by Rockwell C indentation test at a load of 1470 N.

Table 5.1: Detailed information of samples prepared

Sample name	Interlayer	Diamond Growth period	Diamond Coating Thickness
Dia/WC-Co_20h	N/A	20 h	N/A
Dia/W/WC-Co_12h	10-15 nm W	12 h	~2.4 μ m
Dia/W/Al/WC-Co_12h	40-50 nm Al (directly on WC-Co) 10-15 nm W (on top of Al)	12 h	~2.4 μ m
Dia/W/Al/WC-Co_20h	40-50 nm Al (directly on WC-Co) 10-15 nm W (on top of Al)	20 h	~4.0 μ m
Dia/Al/WC-Co_12h [11]	40-50 nm Al	12 h	~2.4 μ m

(Dia: short for diamond)

5.3 Results and Discussion

Figure 5.1 shows the normalized XRD patterns of the samples after diamond deposition. Besides peaks of WC and Co from the substrate, diffraction peaks from the interlayers and diamond coatings are clearly shown. A W peak at 2θ=39.41º is found in the samples of Dia/W/WC-Co_12h (Dia: short for diamond), while in the samples of Dia/W/Al/WC-Co_12h and Dia/W/Al/WC-Co_20h, the W peak shifts to 40.40º. This shifting takes place probably because some Al atoms diffused into the W layer to form substitutional solid solution and the W crystal lattice constants decrease due to the smaller atomic size of Al. There are no Al peaks revealed from the XRD patterns, which is probably because of the dissolution, the relatively low diffraction intensity and adsorption of X-ray by diamond and W layers. The XRD results also show diamond peaks (denoted as D) in each pattern, while those on W/Al have the highest intensity and the one on the bare substrate has the lowest.

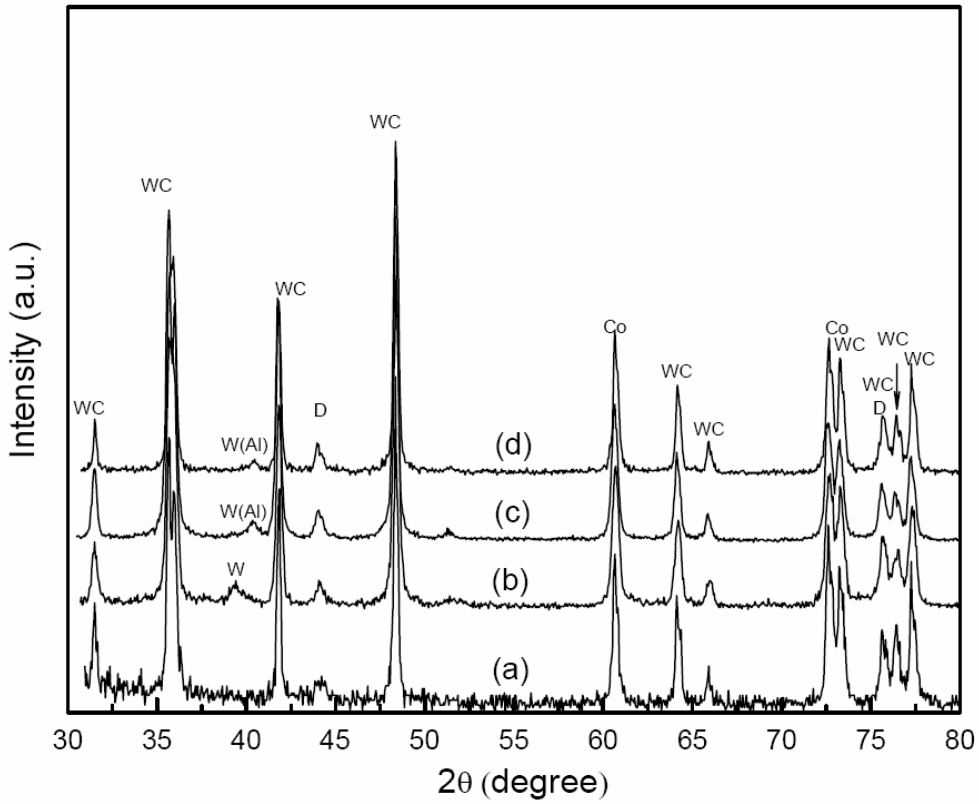

Figure 5.1. XRD patterns of (a) Dia/WC-Co_20h (b) Dia/W/WC-Co_12h (c) Dia/W/Al/WC-Co_12h and (d) Dia/W/Al/WC-Co_20h.

Figure 5.2 shows the Raman spectra of the deposits on WC-Co with and without an interlayer. All of the spectra clearly reveal a diamond characteristic peak at 1332 cm^{-1}. Comparing the spectra, we can see that the 1332 cm^{-1} peak for Dia/W/Al/WC-Co_12h has the largest full-width at half maximum (FWHM), which is approximately 14 cm^{-1}. The broadening of the peak is caused by the refining of the grain size of diamond. This indicates that Dia/W/Al/WC-Co_12h has the smallest grain size. The broad peak at around 1550 cm^{-1} in all spectra corresponds to sp^2-bonded non-diamond carbon. The assignment of the 1450 cm^{-1} peak is still

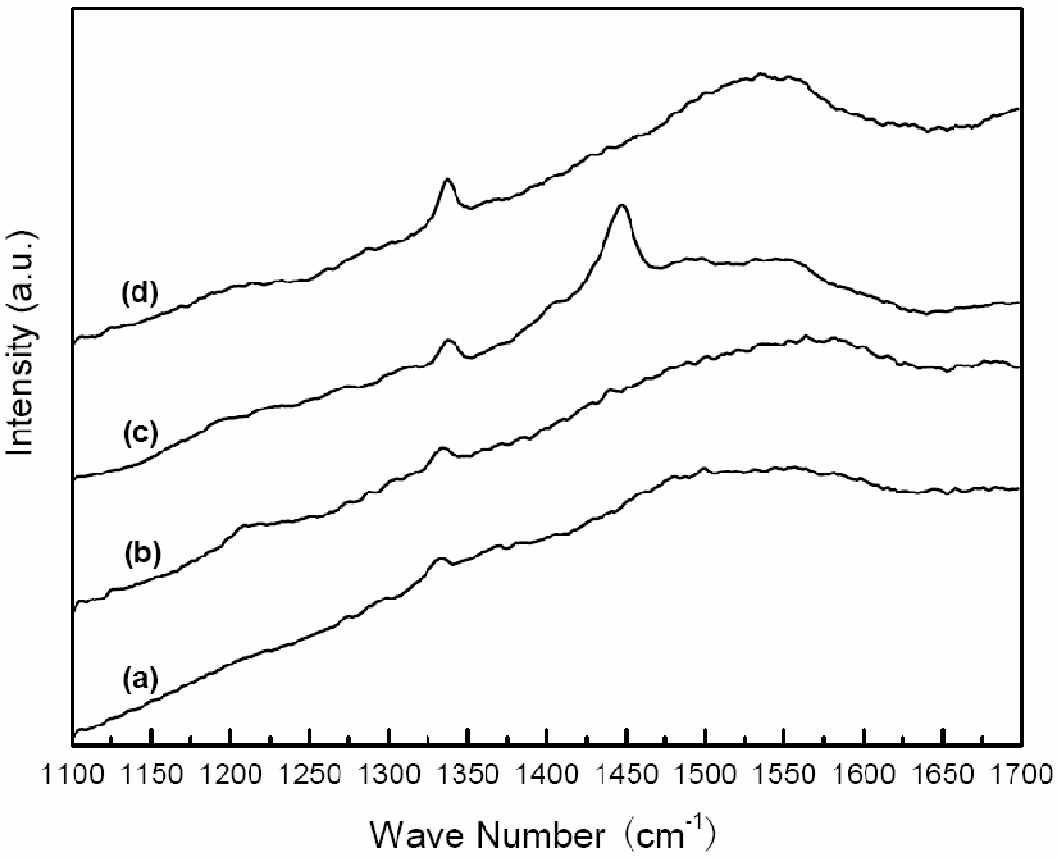

Figure 5.2. Raman spectra of (a) Dia/WC-Co_20h (b) Dia/W/WC-Co_12h (c) Dia/W/Al/WC-Co_12h and (d) Dia/W/Al/WC-Co_20h.

controversial. It has been attributed to the scattering from amorphous sp^2 carbon [*Nemanich et al., 1988*] or some form of sp^3 bonding [*Shroder et al., 1990*]. Ferrari and Robertson [*Ferrari and Robertson, 2001*] assigned the peak (together with the one at 1150 cm^{-1} which is not seen in this case) to trans-polyacetylene (TPA), $(C_2H_2)n$, that is expected to be present at grain boundaries in NCD.

SEM surface images of the samples, as shown in Figure 5.3, further reveal the coating quality. Figure 5.3(a) shows the deposits on bare WC-Co. It can be seen that

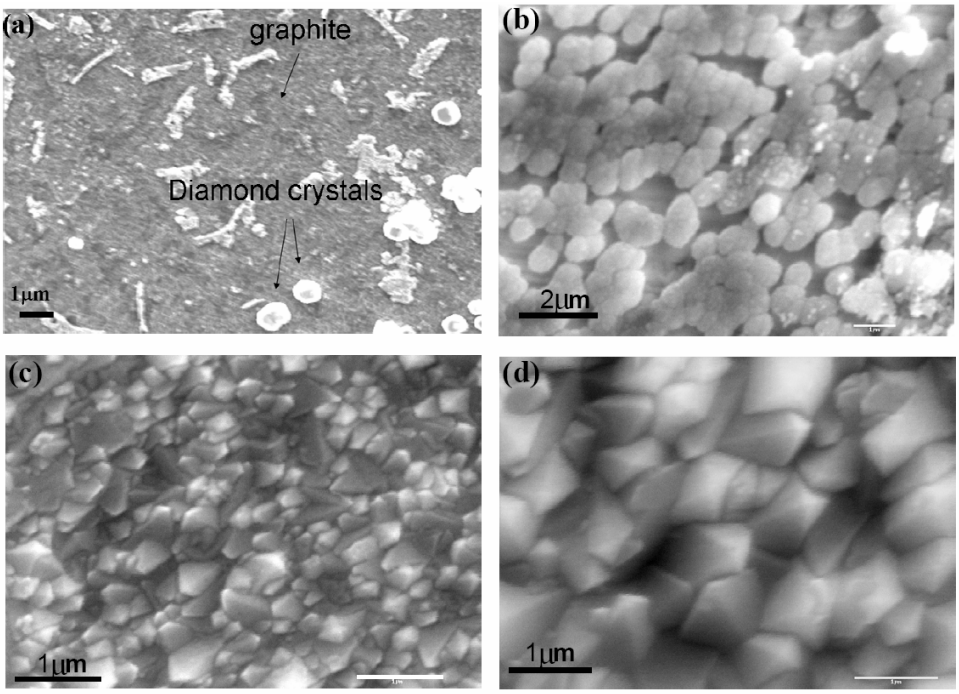

Figure 5.3. SEM images of (a) Dia/WC-Co_20h (b) Dia/W/WC-Co_12h (c) Dia/W/Al/WC-Co_12h and (d) Dia/W/Al/WC-Co_20h.

a composite of separated diamond crystals and graphite was formed on the surface. The formation of graphite is due to the presence of Co, which acts as a catalyst to form graphite instead of diamond. Figure 5.3b shows the diamond coating grown on WC-Co with a W interlayer. The nucleation density is much higher than that on bare WC-Co but it is still not high enough to form continuous thin film. There are some bright spots on the diamond particles, which are Co particles diffused from the substrate due to the high temperature during the CVD process, as confirmed by energy dispersion X-ray analysis. Figure 5.3c shows the diamond coating grown for 12h on a double W/Al interlayer. It can be seen that continuous diamond coating was formed. The grain size ranges from several tens to hundreds of nm. However,

with the continuing growth of diamond for 20 h, as seen from Figure 5.3d, the grain size reached to an average size of approximately 1 μm.

Coating adhesion is the main concern for cutting tool applications. Figure 5.4 shows the SEM images of diamond coating after Rockwell C indentation test at 1470 N. The indentation on Dia/W/WC-Co_12h is shown in Figure 5.4a, in which one can find a large white area corresponding to film spallation around the indentation. Figure 5.4b shows the indentation on Dia/W/Al/WC-Co_12h. The white area of spalled diamond film around the indentation is much less than that on diamond/W. For a thicker diamond coating (Dia/W/Al/WC-Co_20h) as depicted in Figure 5.4c, the spallation area is larger than that of sample with 12h deposition, indicating that a higher internal stress developed when the diamond grains grew into micro scale and the film thickened. Comparing Figure 5.4, we can find that the spallation area around the indentation on Dia/W/Al/WC-Co is smaller than that on Dia/W/WC-Co.

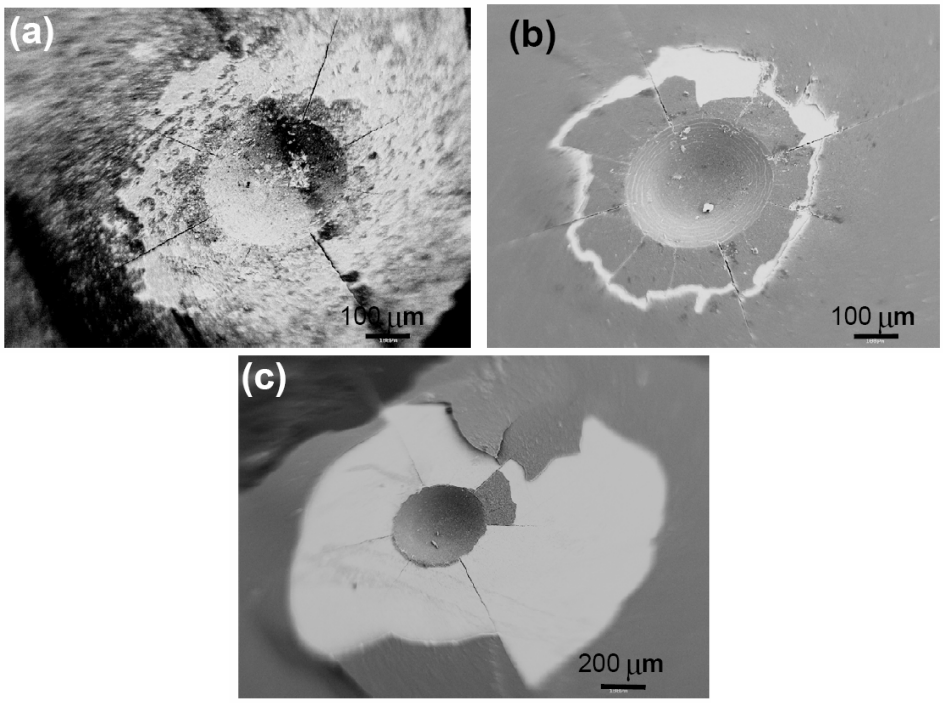

Figure 5.4. SEM images of samples after Rockwell C indentation test: (a) Dia/W/WC-Co_12h (b) Dia/W/Al/WC-Co_12h and (c) Dia/W/Al/WC-Co_20h.

The results presented in this paper show that the diamond coating on a double W/Al interlayer has much higher nucleation density and better adhesion than that on W single interlayer. Without Al, a layer of W cannot completely suppress the detrimental effect of Co. These results indicate that the Al interlayer plays an important role in the enhancement of the nucleation and adhesion of diamond coating on WC-Co cemented cutting tools, which is in consistence with the results in the previous Chapter. It was suggested that the Al interlayer decreases the graphitization tendency during diamond deposition process by donating electrons to Co and modifying its external 3d electronic structure which is closely related to its catalytic ability [*Li and Hirose, 2006*]**.**

The main advantage of introducing W into the W/Al interlayer system is that it facilitates NCD formation under typical microcrystalline diamond growth conditions. The diamond coating grown on Al/WC-Co in the same growth conditions is found to be microcrystalline. The formation of NCD on W/Al/WC-Co in this work is attributed to the suppression of graphite formation introduced by Al and the enhancement of diamond nucleation by W layer. The thin layer of W would react with C from the deposition precursor and form the W-C phase to enhance diamond nucleation [*Chen et al., 2008*]. As is well known, NCD coatings are highly desirable for cutting tool and other tribological applications [*Gruen et al., 1999*], because smaller grain size enhances coating toughness and increases surface smoothness, and a smoother surface can facilitate chip evacuation and thus reduce cutting forces [*Polini, 2006*].

In addition, the total thickness of the double interlayer is approximately 50-65 nm. The loss of cutting edge sharpness and the effect on mechanical properties due to the introduction of interlayer would be negligible. Furthermore, it is possible to optimize the thickness of individual Al and W layers so that the interlayer maintains the functionality but after the CVD process, little of the interlayer materials remain. As a result, there would be no mechanically weak layers existing between the WC-Co substrates and diamond coatings.

5.4 Conclusions

This Chapter presents a new double interlayer W/Al for CVD diamond coatings on WC-Co cemented cutting tools, in which a thin layer of Al directly deposited on

cutting tool is used to suppress the formation of graphite catalyzed by Co and an additional thin layer of W is used to enhance diamond nucleation. The results have demonstrated that the W/Al interlayer can enhance diamond nucleation and adhesion on WC-Co tools and thus facilitating the formation of adherent diamond coatings on WC-Co inserts.

CHAPTER 6
DIAMOND NUCLEATION ENHANCEMENT MECHANISM OF AL AND CARBIDE-FORMING ELEMENT INTERLAYERS ON WC-CO CUTTING TOOLS*

6.1 Introduction

In the previous Chapter, a new double W/Al interlayer design was proposed to enhance diamond nucleation and adhesion on WC-Co cutting tools. The double interlayer consists of a thin layer of Al directly deposited on WC-Co to suppress the interfacial graphitization induced by Co, and an additional thin layer of W to enhance diamond nucleation. The investigation of W/Al double layer on WC-Co has showed that the double interlayer can prevent the formation of graphite soot between the substrate and the diamond thin films and enhance the nucleation of diamond, and thus facilitate the growth of adhesive nanocrytalline diamond thin films on WC-Co under typical microcrystalline diamond growth conditions.

In order to optimize the double interlayer design for diamond coating deposition, it is necessary to understand the individual effect of Al and W interlayers on the

* Part of this section has been published on the journal of *Thin Solid Films*. According to the Copyright Agreement, "the authors retain the right to include the journal article, in full or in part, in a thesis or dissertation".

nucleation and growth of diamond and how W compares to other typical carbide-forming elements (CFE).

In this Chapter, diamond nucleation and growth on WC-Co and Si (to remove the effect of Al and Co) coated with several typical CFE (Ti, Cr and W) interlayers is investigated. The results are compared with those on the corresponding CFE bulk materials and some typical metal nitride interlayers to understand the involved mechanisms.

6.2 Experimental

Si wafers and WC-Co cutting tool inserts were chemically cleaned with acetone followed by methanol, and then placed into an ion beam sputtering system for interlayer deposition. The working pressure for interlayer deposition was 0.12 Pa. For WC-Co cutting inserts, prior to the deposition of CFE interlayer, a layer of Al (40 to 50 nm) was deposited on them to suppress the catalytic effect of Co for diamond deposition. The subsequent deposition of Ti, Cr and W was conducted by Ar ion beam sputtering the respective target (all having 99.99% purity) to produce interlayers of Ti, Cr and W with a thickness of 10 to 15 nm on both Si wafers and the Al precoated WC-Co inserts. For the deposition of AlN and WN interlayers, nitrogen gas with a flow rate of 2 sccm was introduced to the chamber during the sputtering of Al and W. After interlayer deposition, the substrates were scratched by diamond powders in an ultrasonic bath for 120 s to increase diamond nucleation. Diamond thin film deposition was conducted in a 2.45 GHz Microwave plasma CVD reactor. The working pressure and microwave power were maintained at 30

Torr and 1000 W, respectively. The substrate temperature was approximately 740 ºC as measured by a thermocouple mounted underneath the Mo substrate holder. The surface morphologies and microstructure of the samples were characterized by scanning electron microscopy (SEM), scanning probe microscopy (SPM) and X-ray diffraction (XRD).

6.3 Results and Discussion

Figure 6.1 shows the XRD pattern of the as-deposited W interlayer. A halo broad peak centered at approximately $2\theta = 15^{\circ}$ can be clearly seen. This peak is originated from the scattering of the amorphous phase. Broadened peaks of crystalline W can also be clearly seen. The strongest peak of W (210) shows a FWHM (full-width at half maximum) of 0.85º. A rough estimation using Debye-Scherrer's equation [*Patterson, 1939*] shows that the average grain size of the samples is in the order of nanometer (several nanometers). The insert shown in Figure 6.1 is a typical AFM image of the W interlayer. The surface is smooth with a root mean square (RMS) roughness of 0.9 nm. These results indicate that the as-deposited W interlayer is of amorphous/nanocrystalline microstructure. Similar microstructure was obtained for the Ti and Cr interlayers (not shown). It is well known that the microstructure of thin films strongly depends on the deposition processes and processing conditions. According to the generally accepted structure zone model (SZM) [*Movchan and Demchishin, 1969*], the grain size and microstructure of sputtered thin films are a function of T_s/T_m, where T_s is the substrate temperature and T_m is the melting point of the thin film material. The microstructure evolutes from

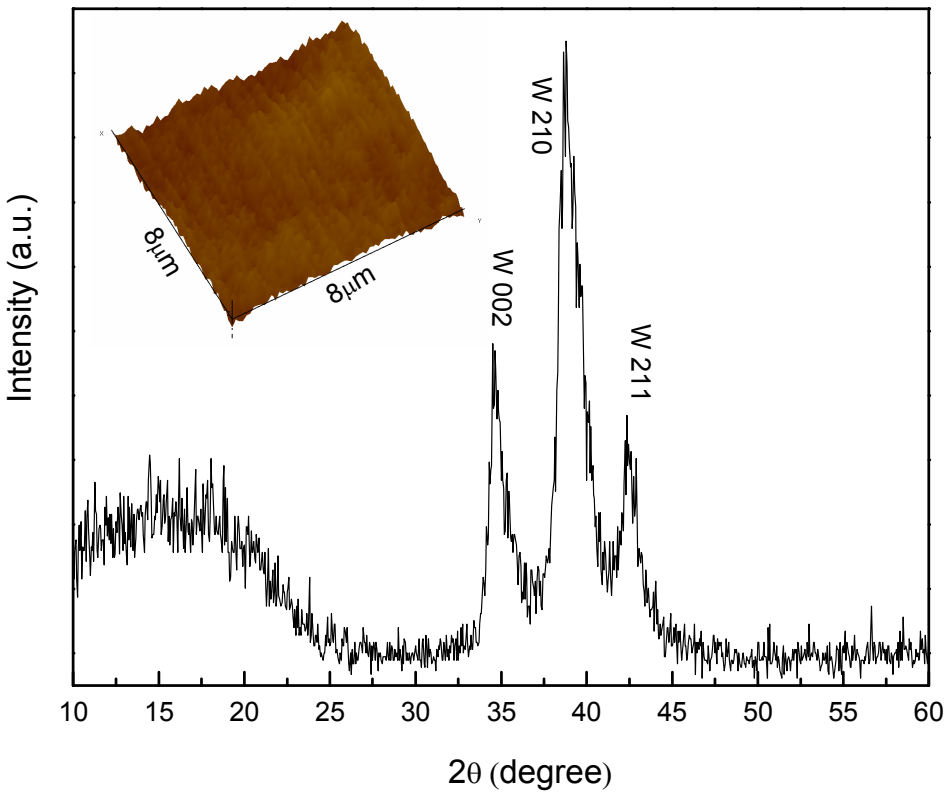

Figure 6.1. XRD pattern of the as-deposited W interlayer. The insert is a SPM image of the W interlayer.

amorphous/nanocrystalline for $T_s/T_m<0.3$ (zone 1), to dense columnar grains for $0.3<T_s/T_m<0.5$ (zone 2), to equiaxial grains for $T_s/T_m>0.5$ (zone 3). In these experiments, the interlayers were deposited at room temperature, where $T_s/T_m < 0.3$. Because of the low mobility of the adatoms at low deposition temperature, the deposited thin films are of amorphous or nanocrystalline structure (zone 1).

Figure 6.2 shows the typical SEM images of diamond grown for 2 h on (a) bare Si and (b) W coated Si. Diamond nucleation density on Si is approximately10^8 cm^{-2}

(Figure 6.2a), typical for diamond scratch pretreatment. The nucleation density increases to$10^9 cm^{-2}$ (Figure 6.2b) when a W interlayer is applied. Figure 3 illustrates the diamond films grown for a longer period of 4 h. On the bare Si substrates (Figure 6.3a), the diamond does not fully cover the substrate and many voids are observed among the diamond clusters. On the other hand, diamond films grown on the W coated Si (Figure 6.3b) show a dense and continuous structure and the grains are so fine that the SEM images of the surface are featureless. For a comparison under the same conditions, a Si wafer partly coated with W was used to grow diamond thin films for 6 h. The SEM images of sample are shown in Figure 6.4. The dashed line in Figure 6.4a shows a distinguishable boundary between the films grown on the uncoated and coated areas of Si. An enlarged view of the area with the interlayer (Figure 6.4b) shows much finer grains than the area without the interlayer (Figure 6.4c). Similar results were observed for the Ti and Cr interlayers (not shown). These results clearly demonstrate that the interlayers can significantly enhance diamond nucleation and result in much finer grains in the diamond thin films.

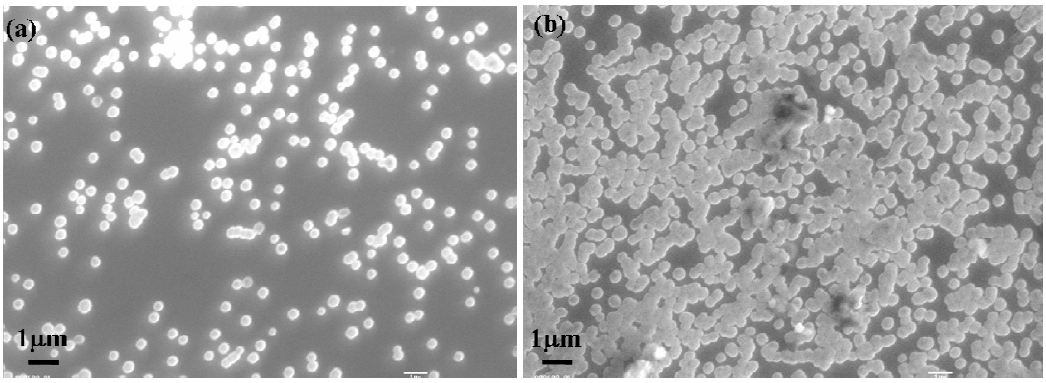

Figure 6.2. Typical SEM images of diamond grown for 2 h on (a) bare Si and (b) W coated Si.

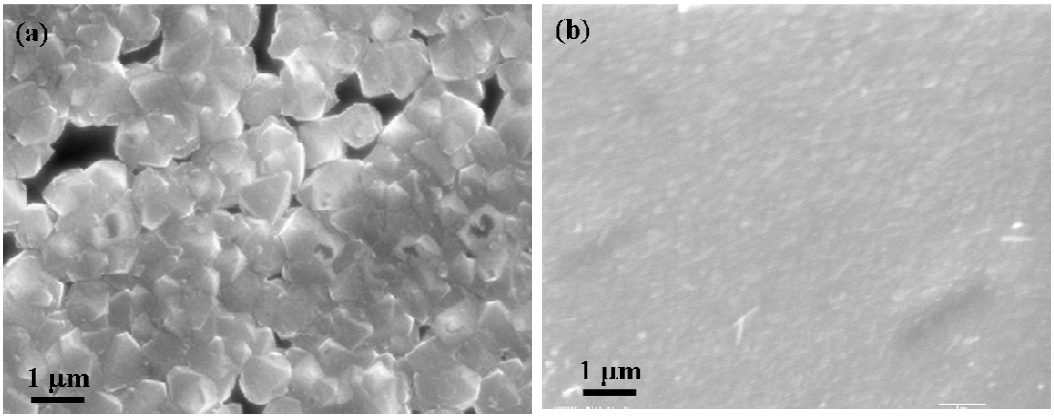

Figure 6.3. Typical SEM images of diamond grown for 4 h on (a) bare Si and (b) W coated Si.

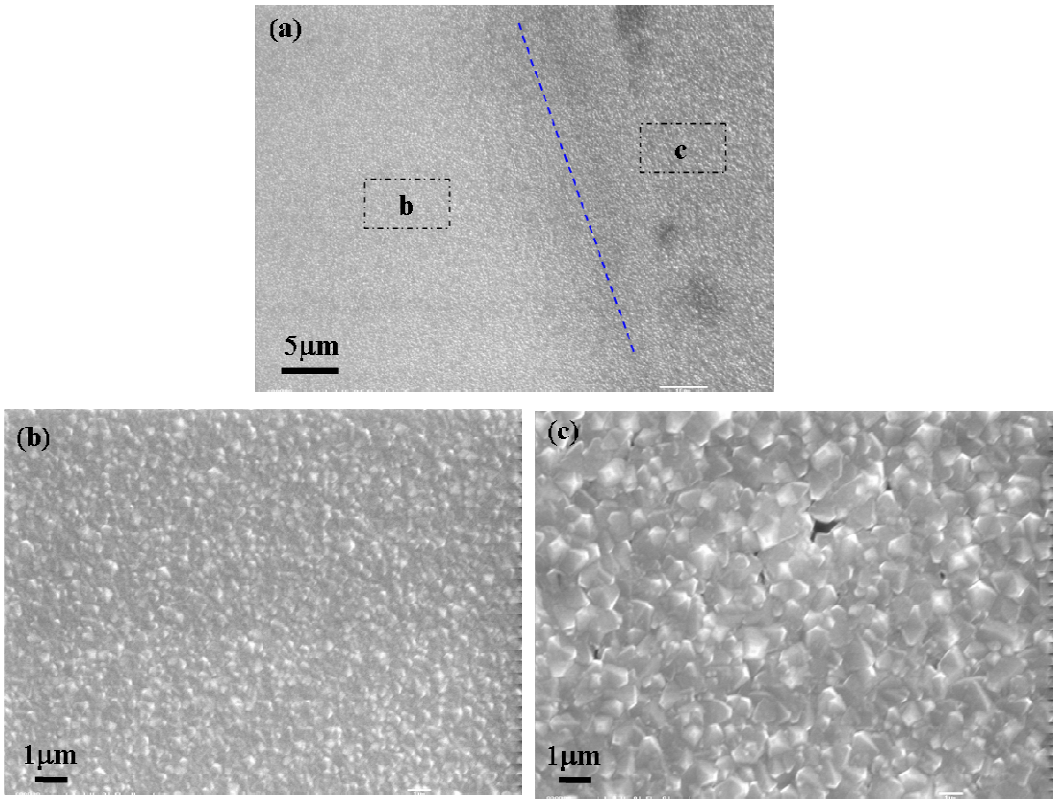

Figure 6.4. SEM images of diamond grown for 6 h on (a) Si substrate partly deposited with the W interlayer (The dash line shows the boundary of areas with and without interlayer.), (b) the area with the W interlayer, and (c) the area without the interlayer.

In order to resolve the fine-grained diamond structure on CFE coated Si wafers, an AFM was used to further examine the surface morphology of the diamond samples. Figure 6.5 shows the samples after a diamond growth for 7 hours. The films on bare Si substrate show the largest grain size and the highest RMS roughness of 224 nm. The diamond films grown on Ti, Cr, and W coated Si wafers show RMS roughness of 36 nm, 30 nm, and 18 nm, respectively, associated with their nanocrystalline structures [*Gruen, 1999*]. These results show that the diamond nucleation density is the highest on W coated samples and the lowest on Ti coated samples.

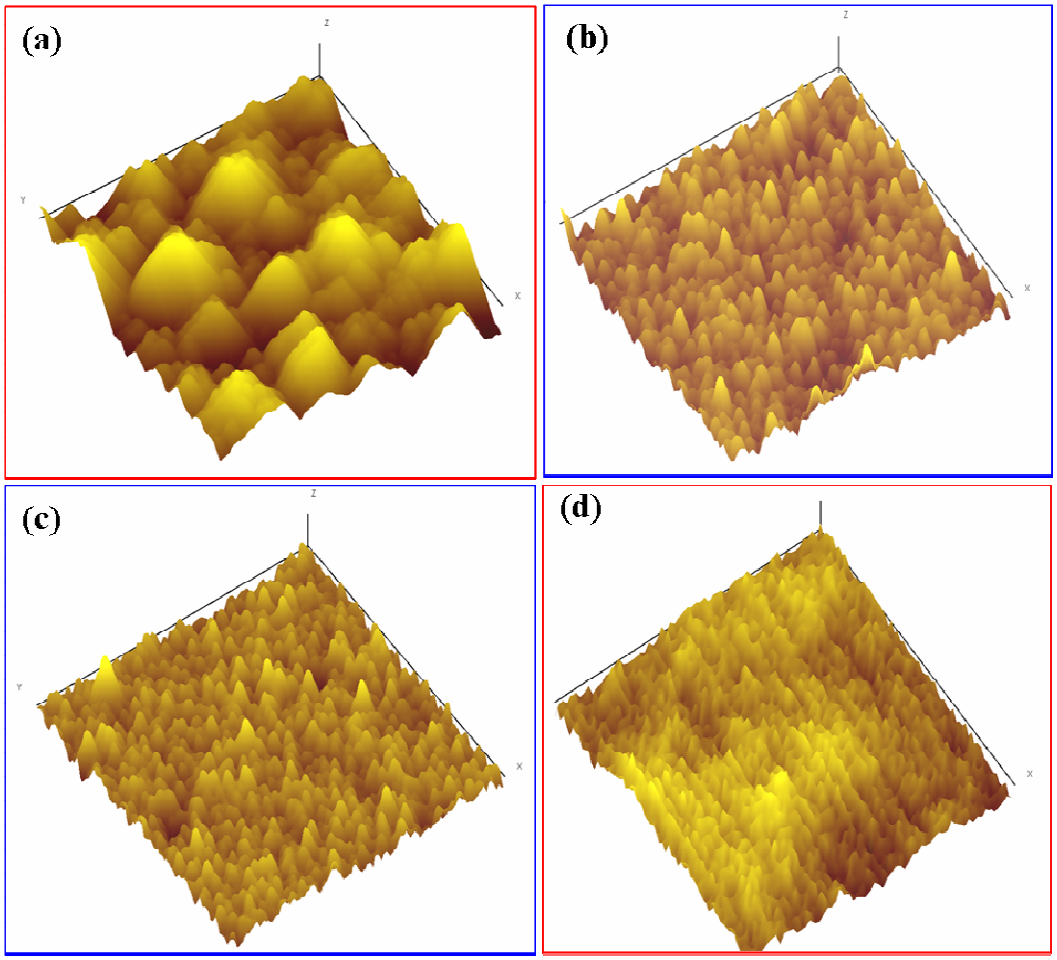

Figure 6.5. SPM images of diamond films grown for 7 h on (a) bare Si, (b) Ti, (c) Cr, (d) W coated Si wafers.

Figure 6.6 shows the typical SEM images of diamond thin films on W/Al, Cr/Al, AlN/Al, and WN/Al coated WC-Co inserts after 12 h growth. The diamond thin films grown with the W/Al interlayer show a dense crystalline structure with grain size ranging from several dozens of nanometers to sub-micrometers (Figure 6.6a). The films on Cr/Al coated inserts (Figure 6.6b) show much larger grains and voids among the grains, which indicates a lower nucleation density. The diamond

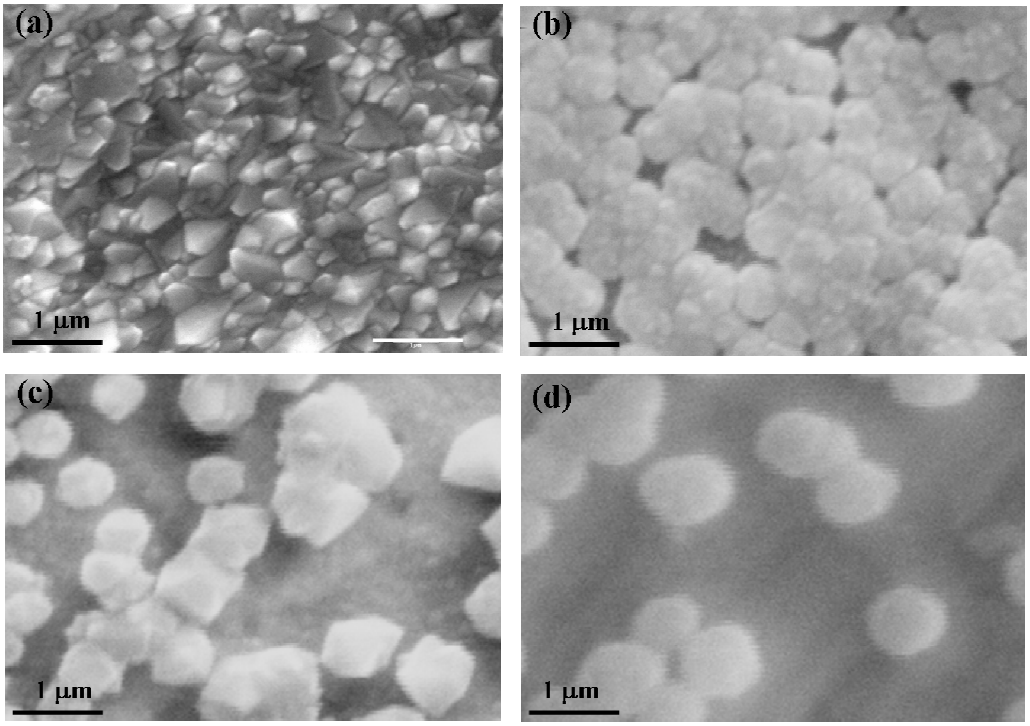

Figure 6.6. Typical SEM images of diamond grown for 12 h on (a) W/Al [9] (b) Cr/Al (c) AlN/Al (d) WN/Al coated WC-Co inserts.

nucleation density on AlN/Al (Figure 6.6c) and WN/Al (Figure 6.6d) coated inserts is much lower in comparison with those on the CFE interlayers. This is in agreement with the results reported on other nitrides such as TiN [*Fu et al., 2000*] and CrN [*Gowri et al., 2007*]. On the whole, the W thin layers demonstrate to be the most effective while Ti thin layers the least in the enhancement of diamond nucleation on both WC-Co inserts and Si wafers.

A comparison of the results of this work with those reported on bulk CFE substrates including Ti [*Fu et al., 1999*], W [*Zhu et al., 1995; Haubner et al., 1996*], Mo [*Zhu et al., 1995; Haubner et al., 1996*], Nb [*Haubner et al., 1996*] and Ta [*Haubner et al.,*

1996] indicates that both the bulk forms and thin layers of CFE have a high diamond nucleation density. Interestingly, however, diamond nucleation density on the CFE thin layer coated substrates is much higher than on bulk CFE materials. In addition, under conventional diamond growth conditions, the diamond thin films formed on bulk CFE materials all show microcrystalline structures [*Fu et al., 1999*; *Zhu et al., 1995; Haubner et al., 1996*] whereas the diamond thin films on the CFE coated Si wafers show nanocrystalline structures, as observed in this research. To understand these different growth behaviors, the enhancement mechanism of diamond nucleation on CFE coated substrates is discussed as follows.

For CFE bulk substrate materials, carbon adatoms on the substrate surface dissolve into the CFE substrate at the initial stage of deposition and form a stable carbide layer. Diamond nucleation occurs on the carbide layer when the carbon concentration on the surface reaches its saturation value [*Joffreau et al., 1988; Lux et al., 1991*]. As indicated by XRD and SPM, the ion beam deposited CFE interlayers have amorphous/nanocrystalline microstructure. It is well known that grain boundaries have various kinds of nonequilibrium defects and stored energy, which facilitate their chemical reactivity [*Gleiter, 1989; Suryanarayana, 2001*]. Because of the enhanced chemical reactivity relative to the conventional coarse-grained bulk materials, carbon atoms can rapidly react with the CFE and supersaturate on the surface to form diamond nuclei on the interlayer. In addition, the defective grain boundaries can lower the energy barrier for nucleation and provide more nucleation sites for diamond, which further enhance the diamond

nucleation rate and nucleation density. Therefore, higher nucleation density and finer diamond grains can be achieved on the CFE coated Si than on bulk CFE materials.

According to the SZM model [*Movchan and Demchishin, 1969*] of thin film growth, the grain size is mainly determined by T_s/T_m. Because W has the highest T_m (3695 K) and Ti has the lowest T_m (1941 K) among W, Ti, and Cr (T_m = 2180 K), the grain size of the W interlayer is expected to be the finest and Ti the coarsest, leading to the highest nucleation density on the W interlayer and lowest on Ti. Moreover, according to Lux *et al*. [*Lux et al., 1991*], the carbon diffusion rate in the metal carbides formed on the CFE surface also affects diamond nucleation and growth. For lower carbon diffusion rate, the carbon adatoms transport into the carbides relatively slowly and more carbon adatoms contribute to diamond nucleation and growth. On the other hand, for higher carbon diffusion rate, carbon adatoms are more readily dissolved in the carbides, and thus the nucleation is delayed and nucleation density is lower. Generally, higher melting points would lead to lower carbon diffusion rate of carbon in the carbides (carbon diffusion rate in WC is three orders of magnitude lower than that in TiC). [*Lux et al., 1991*] Therefore, the diamond has the highest nucleation density in the W interlayer and lowest on Ti among the three tested interlayers.

It is worth noting that diamond nucleation and growth rate on WC-Co is lower than that on Si with the same CFE interlayer (For instance, diamond on Cr coated Si formed continuous films at 4 h, while voids were still observed after 12 h growth on Cr/Al coated WC-Co). This could be attributed to the diffusion of some carbon adatoms into the underneath WC-Co substrate.

This study has also demonstrated the advantage of the CFE interlayers on diamond nucleation over their nitrides which have been widely investigated as the interlayers for diamond thin film deposition. In metallic nitrides, metal atoms form relatively strong and stable bonding with nitrogen atoms. Thus, it is hard for carbon to break the bonds to form a layer of carbide on the top of nitride to facilitate diamond nucleation. In addition, there is a large mismatch of lattice constants and thermal expansion coefficient between nitrides and diamond [*Fu et al., 2000*], which would lead to the delamination of diamond thin films.

6.4 Conclusions

Investigations of diamond nucleation and growth on several typical CFE (Ti, Cr and W) coated Si and WC-Co substrates were presented. The results show that the CFE interlayers deposited by ion beam sputtering have amorphous/nanocrystalline structures to facilitate diamond nucleation, leading to the formation of nanocrystalline diamond thin films on the CFE interlayers even under conventional microcrystalline diamond growth conditions. Among the three interlayers investigated, diamond nucleation density is the highest on W and the lowest on Ti. The results also demonstrate that the diamond nucleation density on the CFE interlayers is much higher than those on widely used metal nitride interlayers.

CHAPTER 7
FABRICATION AND ORIENTATION CONTROL OF DIAMOND NANOTIPS BY BROAD ION BEAM ETCHING*

7.1 Introduction

So far, various novel methods have been discussed to enhance diamond growth on substrate containing transition metals. Apart from coatings, diamond can be fabricated into other forms of nanostructures, such as nanotips, which have potential applications in electronics (field electron emission) and mechanical engineering (e.g. controlling of friction coefficient for development of novel actuators). Diamond nanotips have been synthesized by CVD, RIE and FIB as reviewed in Chapter 1. To overcome the limits of the above techniques in producing nanotip arrays on large areas with controlled orientation, in this Chapter, broad ion beam technique is employed to manipulate nanostructure formation on the surface of CVD microcrystalline diamond to produce oriented diamond nanotip arrays.

---

* Part of this section has been published on the Journal of Physics D: applied physics. According to the Copyright Agreement, the authors retain the right of "copying the article (all or part) for teaching purposes, and including the article (all or part) in research theses or dissertations".

7.2 Experimental

Diamond nanotips were prepared with two steps: (1) growth of diamond on Si substrates and (2) etching by ion beam. Diamond growth was completed with a custom-made HFCVD system. P-type (100) mirror-polished silicon wafers, each with the size of $10\times30\times0.67$ mm^3, were used as substrates. A portion of the Si substrates were scratched with diamond powders to increase diamond nucleation. Both scratched and unscratched Si substrates were chemically cleaned in an ultrasonic bath for 10 minutes, first with acetone and then methanol, before being placed into the vacuum chamber for diamond deposition. The chamber was pumped down to a pressure of 1×10^{-4} Torr using a turbo-molecular pump and then filled with a gas mixture of hydrogen (H_2) and methane (CH_4). The flow rates of H_2 and CH_4 were 50 sccm and 0.5 sccm, respectively. The working pressure was maintained at 4~6 Torr and the filament current was 9.5 A. A thermocouple was mounted right behind the substrate to measure the substrate temperature. The deposition temperature was 750 °C. The growth duration was 1 hour.

The ion etching process employed a Kaufman type ion source made by Kaufman & Robinson, Inc. The ion source was fixed in the wall of the vacuum chamber. The sample stage is located 30.5 cm away from the ion source and can be rotated. The incident angles of the energetic ions were set to 30, 45 and 90 degree with respect to the substrate tangent. The ion current density was approximately 0.2 mA/cm^2 on the surface of the samples and the diameter of the uniform distribution circular area is ~80 mm as measured by a screened probe. In each etching process, one sample is

fixated on the sample stage with the center aligned with ion beam, so that the sample was entirely under the uniform area of ion etching. The etching condition was repeated three times to ensure repeatability. The ion etching was performed without any extra heating. The temperature of the substrate holder is close to room temperature. However, the diamond surface during etching should be above room temperature due to the ion bombardment. The surface temperature due to ion bombardment is estimated to be below 200 °C because of the relatively low ion energy. The vacuum of the chamber is maintained at 8×10^{-6} Torr. Argon was used as feed gas and the accelerate voltage was 800 V. The etching was one hour for each sample and the fluence of ions can be estimated as 4.5×10^{22} /m^2 from the ion current density.

The surface morphologies of the as-grown and ion beam etched samples were examined by scanning electron microscopy (SEM). Raman spectroscopy and synchrotron based near-edge X-ray absorption fine structure (NEXAFS) spectroscopy were employed to study the bonding structure of diamond before and after nanotip formation.

7.3 Results and Discussion

7.3.1 Characterization of Diamond Nanotips

As-grown CVD diamond coating on a scratched Si substrate is shown in Figure 7.1a. The diamond grains are equiaxial and exhibit (111) preferential orientation. After ion beam etching at 30 degrees, well aligned nanotips are formed as shown in Figure

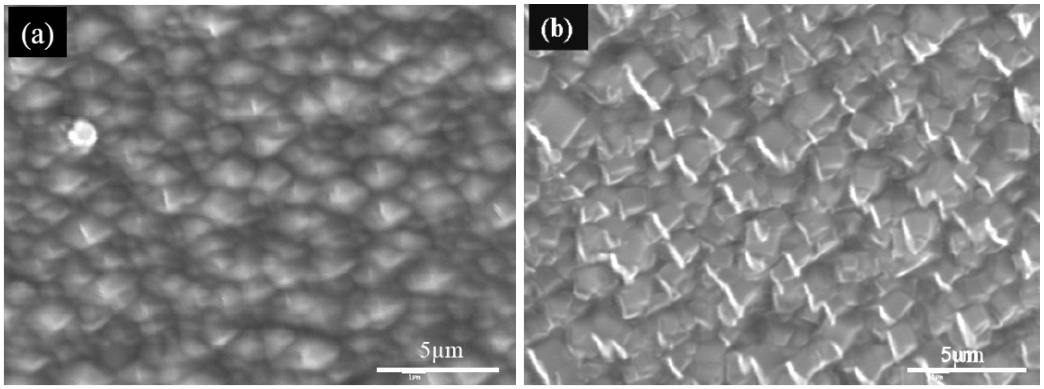

Figure 7.1. SEM images of (a) as-grown diamond coatings (b) diamond nanotips formed after ion beam etching at 30 degrees.

7.1b. To examine the change of individual grains in the process, some mirror polished silicon substrates, without any pretreatment, were employed to grow diamond. In this way, diamond grown on the substrate forms separated crystals rather than a continuous film. As can be seen in Figure 7.2a, the crystals are well faceted and close to equiaxial. The inset shows a portion of the image at higher magnification. Figure 7.2b depicts a top view of the surface structure after ion beam etching. A higher magnification image of a diamond nanotip is shown in the inset of Figure 7.2b. It can be seen that the equiaxial diamond crystals were changed into nanotips. All the nanotips have nanometer-size tips and micrometer-size roots. In addition, all the diamond nanotips have the same apex angle under a given etching condition. Figure 7.3 presents a tilt (7.3a) and cross-sectional (7.3b) view of a typical diamond nanotip structure. All of the nanotips have the same orientation and consistently point against the incident ion beam. To closely examine the relationship between nanotip orientation and ion incidental direction, oblique incident ion

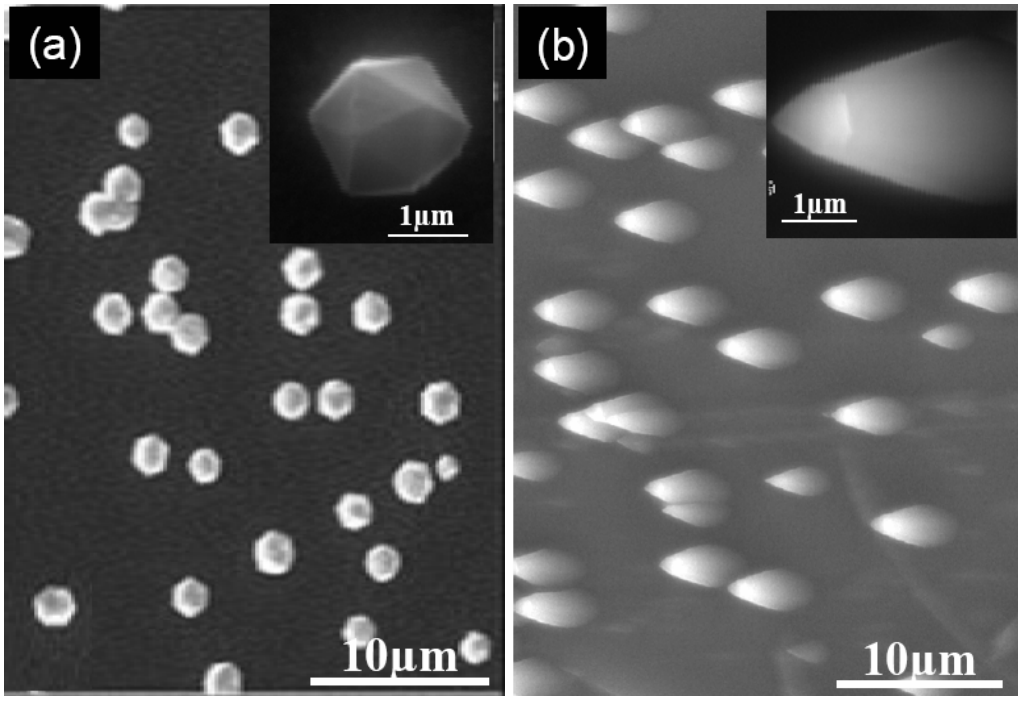

Figure 7.2. SEM images of (a) as-grown diamond grains (b) diamond nanotips formed after ion beam etching. Insets are high magnification view.

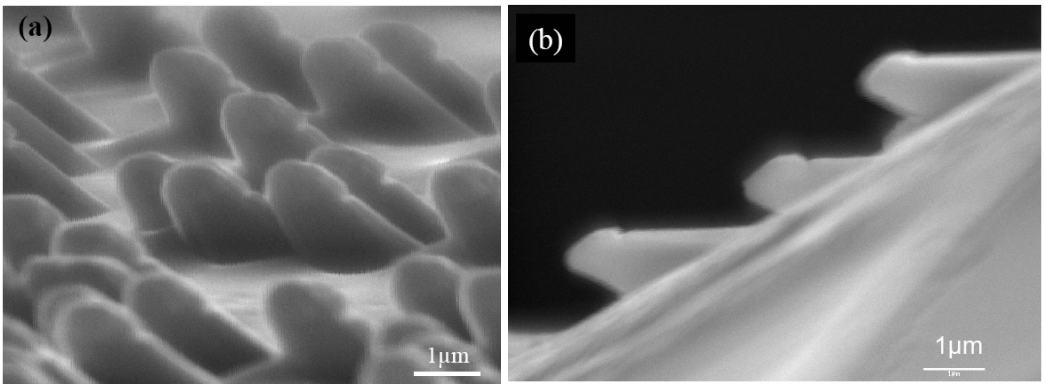

Figure 7.3. SEM tilt (a) and cross-sectional (b) view of a typical diamond nanotip structure.

etching was performed at angles of 90, 45 and 30 degrees relative to the surface tangent.

The diamond nanotips etched at 90 degrees are shown in Figure 7.4. From the tilt view of the sample (Figure 7.4a), it can be seen that the nanotips are vertical to the substrate. This is confirmed by the top view (Figure 7.4b), in which only round dots are seen. The tilt view of 45 degrees etched diamond nanotips is presented in Figure 7.4c which reveals that the obtained nanotips are 45 degrees from the substrate. In the top view (7.4d), part of the side of the nanotips can be seen, which means the nanotips incline towards the substrate plane. Figure 7.4f and 7.4e present a tilt view and a top view of diamond nanotips after being etched at 30 degrees. The nanotips lean towards the substrate at approximately 30 degrees from the tilt view. The top view reveals more sides of the nanotips as compare to 7.4b and 7.4d, which means the nanotips incline further towards the substrate. It should be noted that a groove can be resolved for each of the nanotips in Figure 7.3a, 7.3b, 7.4e and 7.4f. The groove is approximately parallel to the orientation of the substrate. The origin of this interesting feature is still under investigation.

The diamond nanotip structure was assessed not only by shape and orientation but also by the chemical bonding structures. Raman spectroscopy was employed to study the bonding structure of carbon in the nanotips. Figure 7.5 shows the Raman spectra of diamond coating before and after ion etching at 30 degrees (The differences of other spectra from this one are marginal and not shown here). The spectrum of as-grown diamond coating clearly reveals diamond characteristic peak at 1332 cm^{-1}. After ion etching, the diamond peak position remains at 1332 cm^{-1} but the width broadens slightly. The broad peak at around 1550 cm^{-1} in both spectra corresponds to sp^2-bonded non-diamond carbon. It is known that Raman scattering

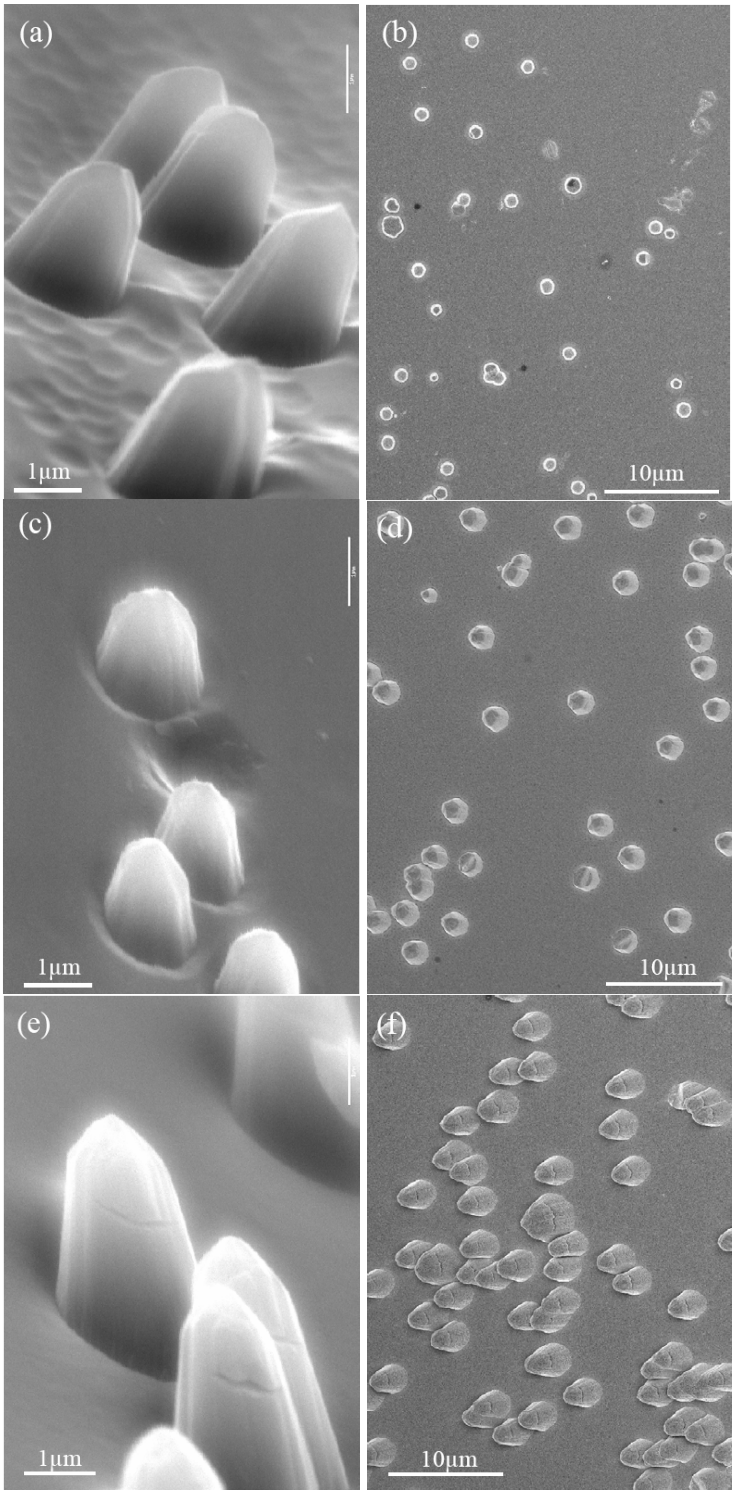

Figure 7.4. SEM tilt and top view of diamond nanotips etched at 90 (a, b), 45 (c, d) and 30 (e, f) degrees to the substrate surface tangent.

in the visible range (514.5 nm) is up to 233 times more sensitive to sp^2-bonded carbon than sp^3-bonded carbon [*Sails et al., 1996*]. The Raman spectra after ion beam etching do not show significant increase of graphitic peak intensity, indicating that the quality of diamond is barely degraded by ion beam etching. However, due to the large difference and variation of Raman scattering sensitivity, it is very difficult to use Raman spectra to determine the sp^2/sp^3 ratio in the diamond samples. In addition, the Raman technique is bulk-like: Raman scattering depth for carbon materials is approximately 500 nm. Thus, Raman spectroscopy cannot quantitatively determine the surface hybridization changes of carbon due to ion beam etching. Unlike Raman, synchrotron based NEXAFS spectroscopy has equal detection sensitivity for sp^2 and sp^3 and other forms of carbon hybridization. In the NEXAFS experiments, the signal was collected in TEY mode which reflects bonding information carried by secondary electrons. For carbon K-edge, the secondary electrons emit from an average depth of a few nm [*Frazer et al., 2003*], much less than that of Raman scattering. Therefore, this technique is an efficient tool to study the radiation damage on the surface of diamond due to ion etching.

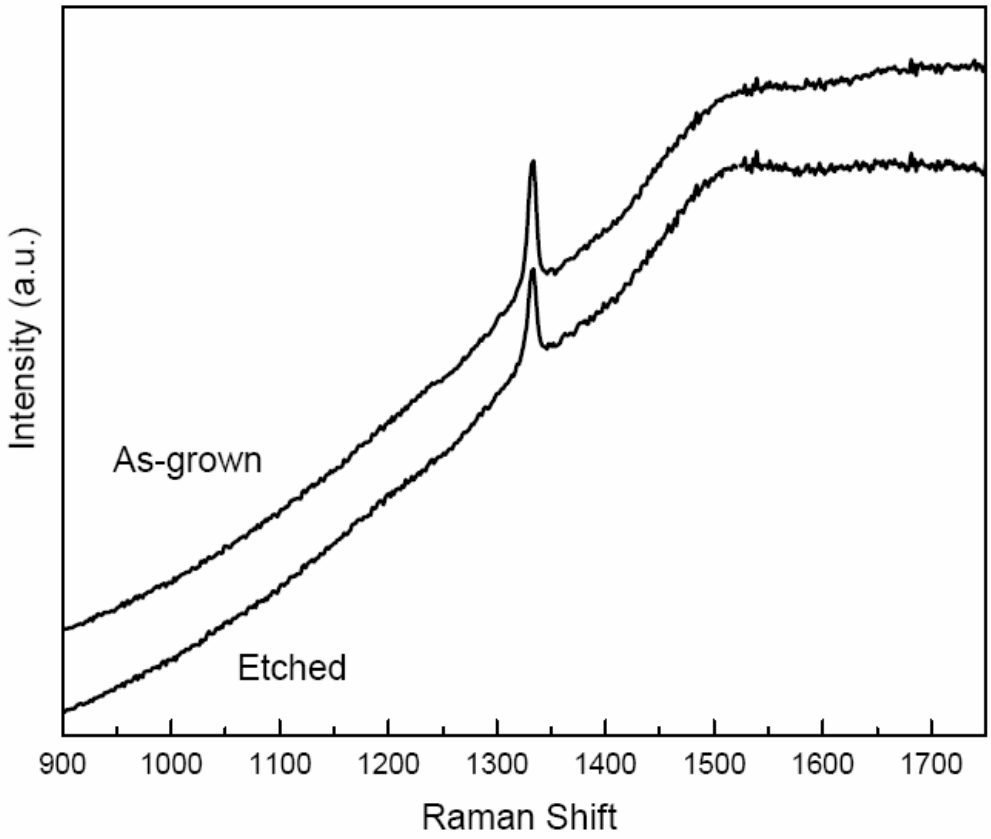

Figure 7.5. Raman spectra of as-grown diamond coating and nanotips after being etched by ion beam at 30 degrees.

The NEXAFS spectra of as-grown and ion beam etched diamond at 30 degrees (The differences of other spectra from this one are marginal and not shown here) are shown in Figure 7.6. Both spectra clearly exhibit a sharp 1s absorption edge at 289.5 eV and a large dip at 302.0 eV, which are characteristic features of pure diamond. There is also a weak peak at 285.5 eV in the spectra. This is the signature of π^* bonding from the non-diamond carbon. Based on the relative intensity, one can see the diamond sp^3 structure is dominant in both spectra. A close examination reveals that the peaks at 288.0 eV and 288.7 eV associated with as-grown diamond coatings,

vanished after ion beam etching. The two peaks correspond to C-H bonding at the very surface of CVD diamond. The change is reasonable since the C-H bonding is weak and unstable, and thus easily destroyed by energetic ion bombardment.

The sp^2/sp^3 ratio change after ion etching is also examined from the NEXAFS spectra. The sp^2 fraction was quantified using the following formula [*Berger et al., 1988*]:

$$f_{sp^2} = \frac{I_{sam}^{\pi^*} I_{ref}(\Delta E)}{I_{ref}^{\pi^*} I_{sam}(\Delta E)} \tag{7.1}$$

where $I_{sam}^{\pi^*}$ and $I_{ref}^{\pi^*}$ are the integral areas of the π^* peaks in the C K-edge of the diamond coatings and a reference sample of highly oriented pyrolytic graphite (HOPG), respectively. $I_{ref}(\Delta E)$ and $I_{sam}(\Delta E)$ are the total integral areas of the whole energy window ΔE. HOPG is known to have 100% sp^2 bonding, thus the number $I_{ref}^{\pi^*} / I_{ref}(\Delta E)$ represents 100% sp^2 bonding. The concentration of sp^2 bonded carbon in the sample can be determined from the ratio of the π^* peak integral in the sample to that of the reference. The change of sp^2 fraction calculated was approximately 12%. This indicates that the ion beam etching slightly increased the sp^2/sp^3 ratio at the surface of the CVD diamond. It is very likely that some sp^3 bonds on the top layer were transferred into sp^2 during the etching process. Chen *et al*.. [*Chen et al., 2007*] reported similar results of sp^3 bonding transforms into sp^2 at the surface after as-grown diamond was treated by nitrogen plasma immersion ion implantation. The transformation in the surface is desirable for some applications

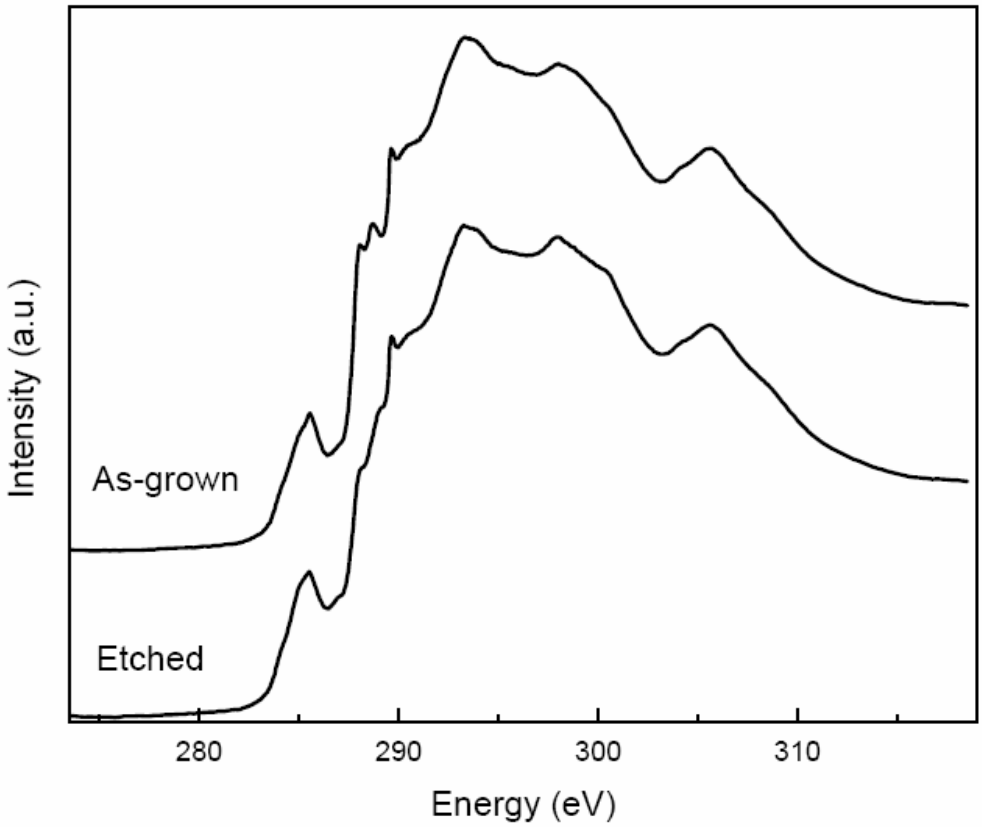

Figure 7.6. NEXAFS spectra of as-grown diamond coating and nanotips after being etched by ion beam at 30 degrees.

such as field electron emission because it can enhance electrical conductivity which improves field electron emission properties [*Chen et al., 2007*].

The formation of diamond nanotips in the experiments can be explained by Sigmund's sputtering theory [*Sigmund, 1969*] and the angle-dependent sputtering mechanism proposed by Yang *et al.* [*Yang and Tang, 2009*]. The sputtering yield depends on the ion energy and the incident angle of incoming ions for a given pair of etchant and target materials [*Ducommun et al., 1975*]. In the initial stage of ion etching of a diamond spike, sputtering yield could be different on each side of the

spike as the local incident angles may be not the same. The material on each side of the spike is etched out at a rate determined by the local incident angle. As the etching proceeds, the sputtering yield and local incident angle converge to the same value for each side of the spike. After achieving a stable etching state, a symmetric conical nanotip structures can be formed and the axis of each nanotip is in the direction against the incident ion beam. As a result, the orientation of the obtained nanotips is determined by the incident angle of etching.

7.3.2 Application of diamond nanotip structure for piezoelectric-driven stick-slip actuator

Piezoactuated positioning system is widely used in many applications, such as micro-scale precise machining and mechanical insertion of genes in cells. The key parts of the systems are the piezoelectric actuators (PEA) which produce extremely small displacements (down to 0.01 μm). The drawback of PEA is the limited motion range (typically up to 0.1% of the size of the piezoelectric element), which greatly restricts their applications from long-range positioning. Numerous displacement-amplifying designs have been reported, nevertheless, all suffer from complex configuration, large size or high cost.

Recently, a novel design of piezoelectric actuator, called piezoelectric-driven stick-slip actuator (PDSSA) was proposed as shown schematically in Figure 7.7 [*Zhang, 2009*]. A platform (object 2) is attached to a PEA (object 1). An end-effector (object 3) is placed on the platform. The actuator is stimulated by pulse voltages. When the voltage is on and the actuator is stimulated to expand, end-effector moves forward

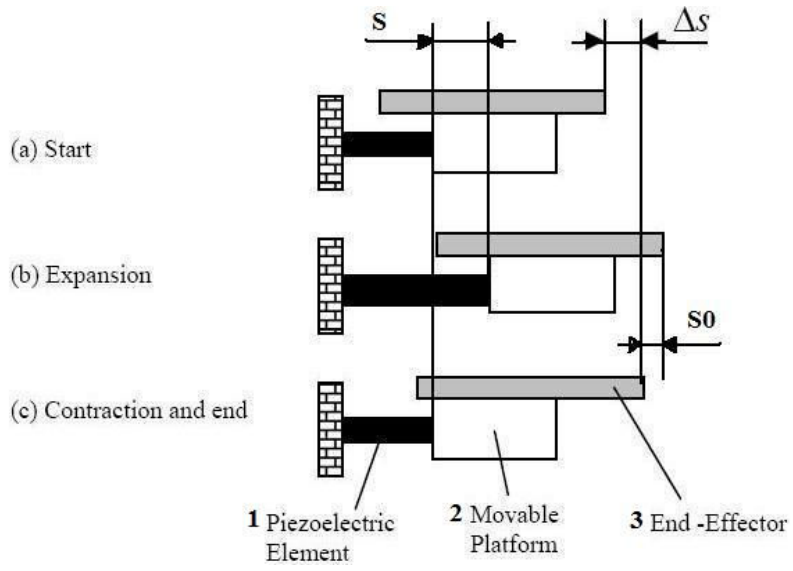

Figure 7.7. A schematic diagram of working principle of the PEA actuator

with the platform, due to the friction force, with a distance of *S*. The actuator contracts when the voltage is off. Because of the inertia, the end-effector slides forwards on the platform. As a result, the end-effector displaces (ΔS) with respect to its original position. By constantly stimulating the PEA to expand and contract, the end-effector's displacement of each cycle, ΔS, builds up and a long-range displacement can be achieved. For high efficiency of the PEA, the friction during PEA expansion should be large so that the end-effector sticks on the platform well and move forward without slipping. The friction during PEA contraction should be small so that the end-effector slips a long distance relative to the platform before it stops.

The friction anisotropy of the surface between PEA platform and end-effector is crucial to accomplish the novel design. It is well known that the friction coefficient

of materials is strongly affected by their surface structure. However, materials with ordinary surface finishing have isotropic surface, that is, the friction is roughly the same for difference directions. In this work, the surface with oriented diamond nanotips structures is proposed to achieve friction anisotropy for this application.

Friction test was performed with Universal Material Tester (UMT) between two surfaces etched by ion beam with 45 degree. Two etched samples were mounted on the tester face to face and the oriented tips from each surface were against each other as Figure 7.8 shows.

The coefficients of friction were measured respectively when the diamond tips slide along each other and against each other. To block out system errors, two mirror polished silicon wafers were also tested. The coefficients are around 0.25 and isotropic regardless the sliding directions. However, bi-directional friction anisotropy can be observed in the friction behavior of two etched diamond surfaces as shown in Figure 7.9. Graph A denotes the friction coefficients changing with time when the diamond tips of each surface slide against each other. In this condition, the friction coefficient stabilizes at about 0.60. When the diamond tips slide along each other, the friction coefficient stabilizes at about 0.35 as shown in graph B.

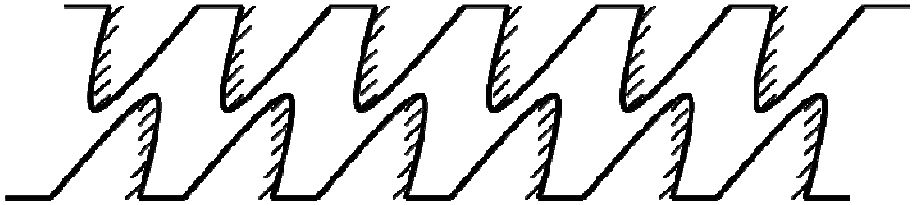

Figure 7.8. A schematic diagram of the two surfaces contacted together for friction test

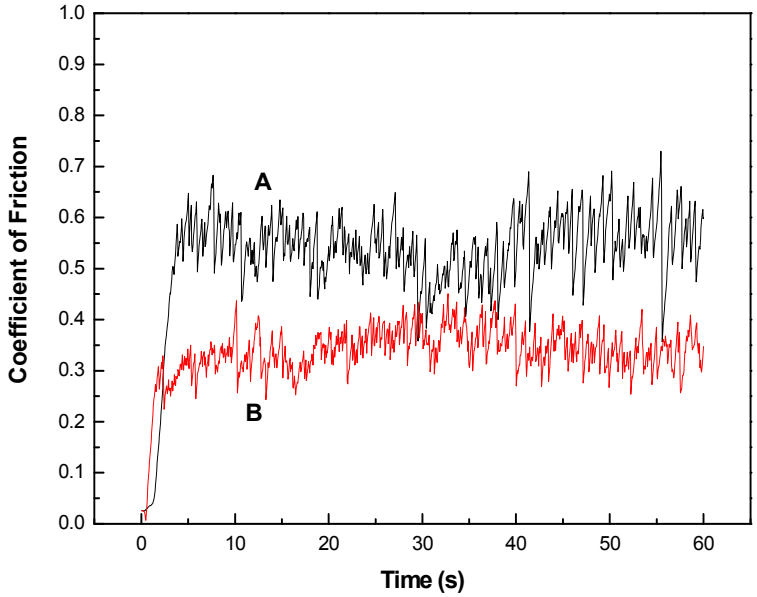

Figure 7.9. Friction coefficients when the diamond tips slide against (A) and (B) along each other.

Etched diamond coatings were amounted, tips against tips, on the contact surface between the platform and end-effector. Voltage signals were applied to the PEA power amplifier to drive the end-effector to move forward and backward. A sensor was used to measure the displacement of the end-effector, with a resolution of 0.01μm. The data of the displacement of the end-effector were recorded. In order to compare, isotropic-friction surfaces, fabricated with diamond coating on the silicon wafers with 90 degree etching, were also used for the working surfaces of the

actuator in the experiments. The measured displacements of the end-effector are shown in Figure 7.10. Curve A denotes the displacement of the end-effector when surface is frictional anisotropic. Curve B shows the displacements when the contact surface is isotropic (diamond surface vertically etched). Each "sawtooth" on the curve shows the displacement of a period of voltage on and off. The displacement increases when the voltage is on and drops as the voltage off. The end-effector on the frictional anisotropic surface (curve A) moves back much less than on the isotropic surface. This results in a large displacement on the anisotropic surface within the number of period. The step efficiency of the actuator (denoted by η) is introduced, which is defined by

$$\eta = \frac{S - S_0}{S} \times 100\% \tag{7.2}$$

where S is the displacement of the end-effector in the stick phase and S_0 the sliding displacement in the slip phase. Using the above equation, the step efficiencies for the results shown in Figure 7.10 were evaluated as 50.1% and 34.0% for the actuators with the anisotropic and isotropic surfaces, respectively.

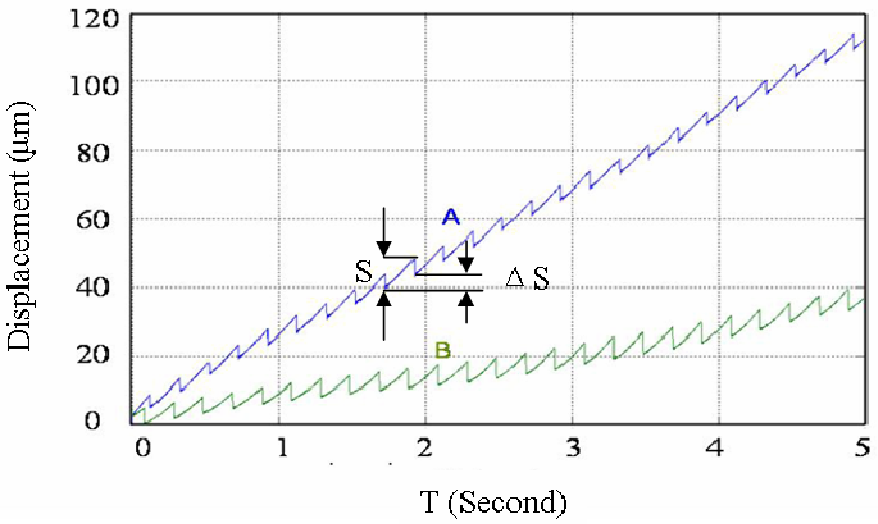

Figure 7.10. Displacement of End-effector with (A) fabricated anisotropic and (b) ordinary isotropic surfaces.

7.4 Conclusions

The experimental results reported in this chapter have clearly demonstrated that diamond nanotips can be fabricated by ion beam etching of as-grown CVD diamond. The orientation of diamond nanotips can be controlled by adjusting the incident ion direction. The sp^2/sp^3 ratio at the surface of diamond nanotips is slightly higher than that of as-grown diamond. Oriented diamond tip nano-arrays have been used to produce frictional anisotropic surface, which is successfully used for ultra-precise positioning system for micro-scale applications. This method of fabricating nanotips has the advantage of nanotip orientation control and it is possible to use the method to fabricate the nanotip arrays of other materials.

CHAPTER 8
DIAMOND-LIKE CARBON THIN FILMS BY END-HALL ION BEAM DEPOSITION

8.1 Introduction

Diamond-like carbon (DLC) has many properties comparable to diamond. DLC has some advantages over diamond, such as high smoothness and low temperature deposition. The most important advantage of DLC is that its properties can be finely tuned for different applications by controlling the composition and using different synthesis process. Based on the composition and structure, DLC can be divided into tα-C, tα-C:H, α-C, α-C:H, etc. Although some progress has been made on end-Hall (EH) ion beam deposited carbon thin films, little work has been reported on investigations of the microstructural and mechanical properties of α-C thin films deposited with EH ion beam. In this Chapter, we report on the preparation of α-C thin films by EH ion source at a mean energy in the range 24 to 48 eV, which was not covered in previous reports, and the investigation of the effects of ion energy and nitrogen doping on the microstructure and mechanical properties of the as-deposited thin films.

8.2 Experimental

In the experiments, an EH ion source (KRI EH-1000, manufactured by Kaufman & Robinson, Inc. USA) was used for thin film deposition. P-type (100) mirror-polished 6-in silicon wafers were used as substrates. The substrates were chemically cleaned in an ultrasonic bath for 10 minutes, first with acetone and then with methanol, before being placed into the vacuum chamber for thin film deposition. The sample stage was located 300 mm away from the ion source and tilted 45 degree with respect to the ion beam. The diameter of the uniform distribution circular area is ~100 mm at a distance of 300 mm as measured by a screened probe Samples were attached to the center of the sample stage, entirely under the uniform area of ion beam.

Methane (CH_4) gas was introduced at a rate of 5 sccm into the ion source to produce hydrocarbon ions. The ion energy was varied while keeping the ion current (1 A) and hydrocarbon gas flow rate (CH_4 of 5 sccm) constant. The discharge voltage, which is the voltage applied to the anode of the ion source, was controlled by the flow rate of Ar (0 to 8 sccm). Since a lower gas flow rate results in a lower pressure, and thus fewer collisions among the electrons, ions, atoms, and molecules in the discharge region, the same discharge current would result in a stronger electric field and higher ion energy for a lower gas flow rate. Therefore, the higher the gas flow rate, the lower the ion energy. The discharge voltage was tuned in the range of 38 to 74 V while the ion discharge current remained stable. The mean ion beam energy is proportional to the discharge voltage and is typically about 65% of the discharge voltage because of the presence of neutral species. Assuming the ions were singly

charged, the mean ion beam energy would range from 24 to 48 eV. For α-C:H:N deposition, N_2 with a flow rate of 1 sccm along with CH_4 and Ar at a flow rate of 5 sccm and 8 sccm, respectively, were used as feeding gases. The ion energy was 24 eV. All the depositions were performed without any extra heating. The temperature of the substrate holder was close to the room temperature. However, the surface of substrate during deposition should be above room temperature due to the ion bombardment. The surface temperature is estimated to be below 75°C because of the relatively low ion energy. The deposition duration was one hour for all the films. The gas pressure during deposition was 9×10^{-4} Torr. The as-deposited α-C thin films were characterized using a NanoAnalyser manufactured by Center for Tribology Inc, for surface morphologies and mechanical properties. The composition of the films and bonding states of the elements were studied by X-ray photoelectron spectroscopy (XPS).

8.3 Results and Discussion

The thin films deposited on 6-in Si wafers show no color patterns under naked eyes, indicating the films are uniform over the whole area. Pan *et al*. [*Pan et al*., *2007*] reported the α-C:H film deposited by EH ion source had the uniformity of 2.5% and 5% for substrate diameter of 20 cm and 40 cm respectively, which was confirmed in the experiments for this work. The thickness of as-deposited α-C:H was measured by a profilometer and found to be 135 nm for 60 min deposition. Therefore, the deposition rate of the films is approximately 2.3 nm/min. The thickness of α-C:H:N was 50 nm for 60 min deposition and the deposition rate is approximately 0.8

nm/min. It can be found that the N addition reduces the film growth rate. Silva *et al*. [*Silva et al*., *1997*] and Rodil *et al*. [*Rodil et al*., *1999*] observed similar phenomena. The cause of this reduction is attributed to two factors. One is the reduced CH growth species in the plasma while nitrogen is added [*Rodil et al*., *1999*]. The other is the chemical sputtering of growing films by nitrogen ionic species [*Rodil et al*., *1999*; *Hammer et al., 1996*].

The surface roughness of the films was evaluated using the scanning probe microscopy in NA. Typical images are shown in Figure 8.1. The root mean square (RMS) roughness of all the α-C:H samples ranges from 0.5 to 0.8 nm. Doping with N reduced the RMS roughness to 0.35 nm. Waltman *et al*. [*Waltman et al*., *2002*] reported RMS values of 0.8-1.2 nm for sputtered α-C:H and α-C:H:N films with a thickness of 1.2-6.5 nm. Logothetidis *et al*. [*Logothetidis et al., 1997*] reported RMS values of 0.5-1.0 nm for magnetron sputtered α-C:H film of 2.5 -35 nm thickness. Comparing the results, it can be found that EH ion beam deposition produces smoother α-C:H thin films than sputtering method does even if the films prepared in this work are much thicker (Surface roughness increases linearly with film thickness, as reported by Logothetidis *et al*. [*Logothetidis et al., 1997*]).

According to literature, filtered cathodic vacuum arc (FCVA) produces the smoothest amorphous carbon films so far. Ferrari *et al*. [*Ferrari et al., 2000*] reported RMS 0.4 -1 nm for tα-C films 30-80 nm in thickness which is comparable with those achieved by in this experiment. Shi *et al*. [*Shi et al., 1999*] reported tα-C films of RMS 0.12-0.6 nm with thickness of 60 nm. Casiraghi *et al*. [Ca*siraghi et al., 2003*] reported much smoother tα-C films by FCVA, RMS 0.1-0.18 nm for film

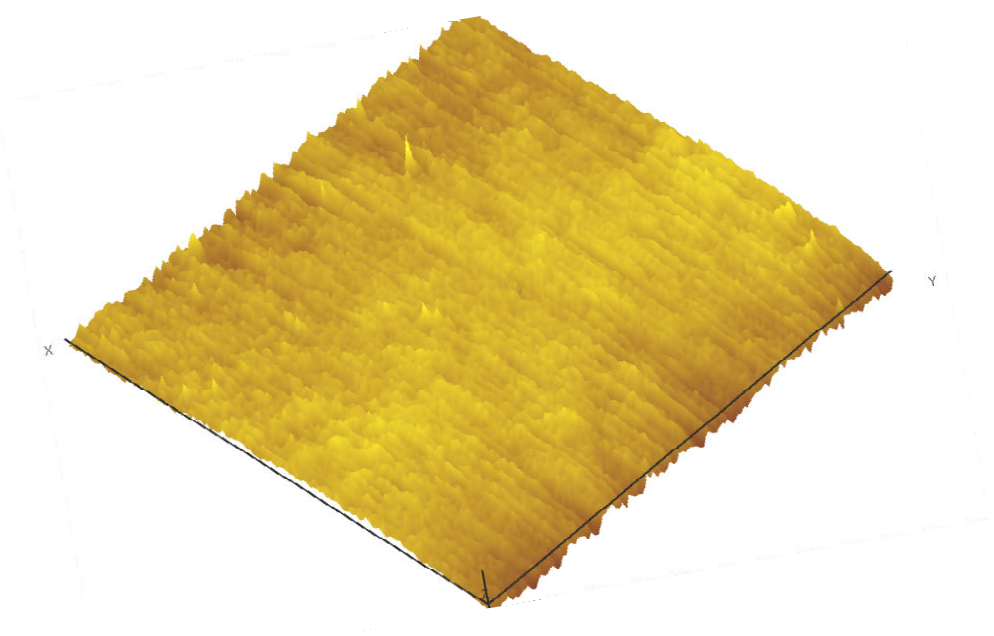

(a)

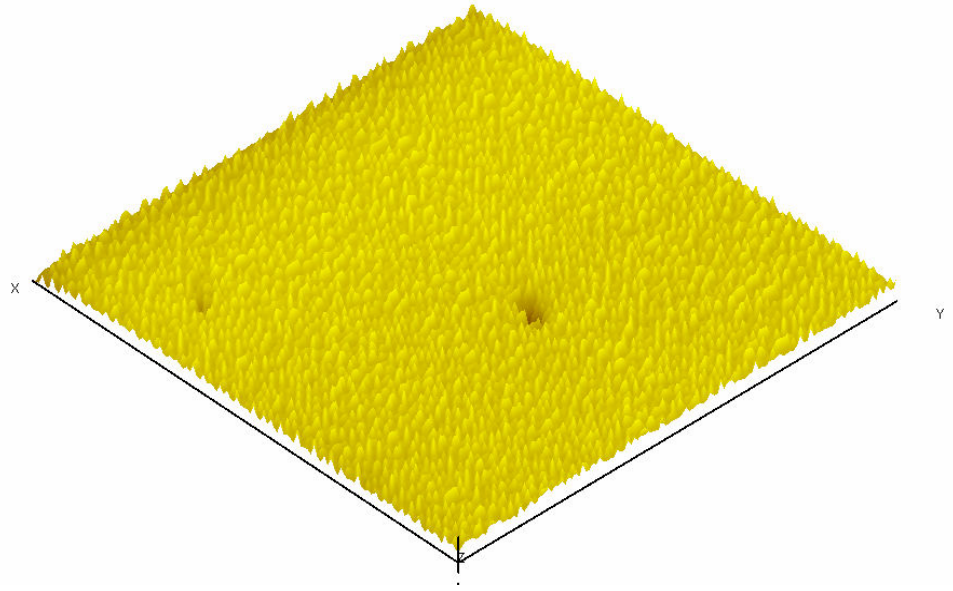

(b)

Figure 8.1. Typical Scanning Probe Microscopy image of (a) α-C:H and (b) α-C:H:N (size: 15μm 15μm) thin films.

thickness from 0.9 to 60 nm. However, apart from plasma, cathodic vacuum arc process generates micrometer sized graphite particulates as by-products. With magnetic filter, the number of particulates in the films can be reduced although some particulates can still pass through the filter by bouncing off the walls. For single-bend FCVA, the particle coverage for is typically around 5%. Even with a sophisticate S-bend filter, the particle coverage can be 0.1%. In areas without particulate inclusion, the surface can be extremely smooth. Particulates are generally avoided in surface roughness measurements [*Casiraghi et al., 2003; Teo et al., 2007*]. However, for large scale application the particulates have to be considered. The roughness as well as other properties can be undermined by the particulates. For instance, graphitic inclusion significantly affects optical gap measurement and hence reduces the apparent optical gap by scattering or absorbing light [*Teo et al., 2007*]. Comparing to FCVA, although EH ion beam deposition produces relatively rougher α-C:H, it is an intrinsically particulate free technique.

Figure 8.2 shows the surface roughness of α-C:H vs. the deposition ion energy. It can be clearly seen that the surface roughness is dependent on the ion beam energy. The α-C:H films deposited at 24 eV show the highest RMS value of 0.8 nm whereas the films show the smoothest surface with a RMS value of 0.5 nm at the ion energy of 34 eV. Further increase in the ion energy leads to the increase of surface roughness. Similar trends were observed by Shi *et al*. [*Shi et al., 1999*] in tetrahedral α-C (tα-C) film by FCVA deposition. The results can be understood from the formation mechanism of continuous film [*Robertson, 2003*]. To form smooth films, two requirements must be met: one is that the deposited phase must have a high

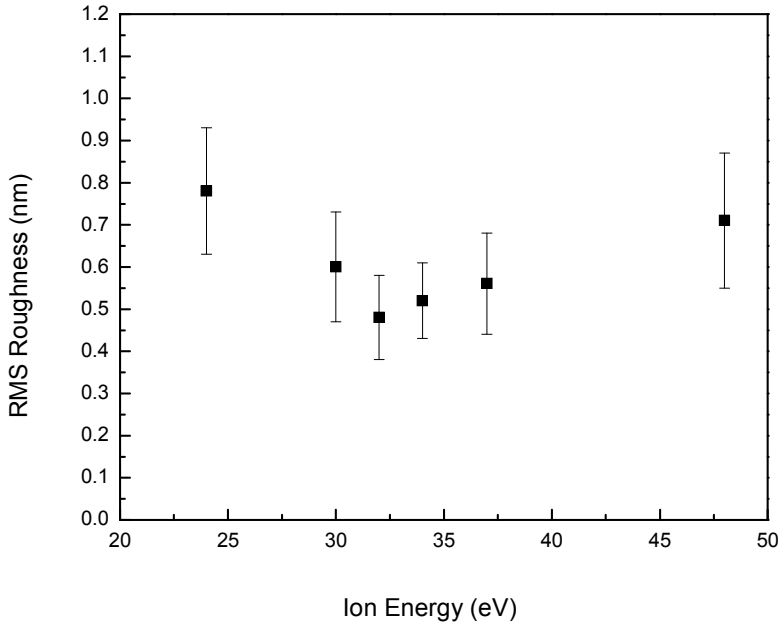

Figure 8.2. RMS roughness values of α-C:H thin films deposited at different ion energy values.

nucleation density on the whole surface and the other is that the deposited species have no surface mobility to move across the surface to form islands. With lower energies, ions have more difficulty to overcome nucleation barriers and thus resulting in relatively lower nucleation density and higher surface roughness. This scenario can also explain why sputtered α-C:H films have much higher roughness compared to EH ion beam deposited films. Sputtered carbon flux is composed of ions with a low average energy of approximately 5 eV mixed with a large fraction of non-energetic neutral species. The energy is much lower than that of EH ion beams, thus the resultant thin films exhibit much higher surface roughness. When the ion energy is higher than the optimum value, the atoms have high energy to migrate

across the surface and aggregate with other clusters, resulting in larger RMS values of roughness.

The chemical bonding structure of α-C:H was studied with XPS. The survey spectra of α-C:H, are presented in Figure 8.3, in which (a) is the spectrum of as-deposited film and (b) is the spectrum after Ar plasma cleaning (to remove surface contaminations). Both spectra show a strong C 1s peak, indicating the film is carbon in nature. The as-deposit films have two weak peaks of O 1s and N 1s. After Ar plasma cleaning, Figure 8.3 (b), N 1s peak is almost disappeared and the intensity of O 1s peak is greatly reduced, which means the presence of oxygen and nitrogen on the surface of the samples is largely due to the physical absorption during the air exposure. The fraction of each element can be estimated from the integral areas of XPS peak as they are proportional to the atomic percentage. After Ar plasma cleaning, the α-C:Hfilms have ≤3.5 at.% oxygen and only trace amount of nitrogen. Figure 8.3 (b) also reveals an Ar $2p_{2/3}$ peak. Ar is introduced by Ar plasma cleaning because the Ar $2p_{2/3}$ peak is not present before Ar plasma cleaning. The Ar fraction is estimated less than 2.5 at.%.

C 1*s* core-level spectrum can be decomposed into two components: sp^2 hybridization, as in graphite, and sp^3 hybridization, as in diamond [*Diaz et al., 1996; Merel et al., 1998*]. Considering the presence of O in the films, as shown by the survey spectrum, the contribution of C-O is also incorporated in the deconvolution analysis. A Shirley-type function [*Tokutaka et al. 1992*] was first used to remove the background which arises largely from inelastic electron scattering. The extracted spectra were then fitted with a combined Gaussian and Lorentzian line profile.

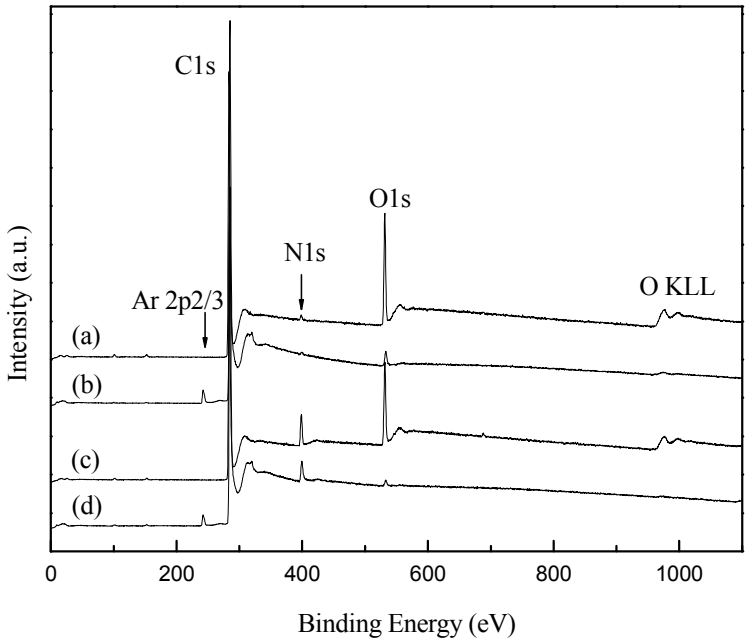

Figure 8.3. XPS survey spectra of α-C:H (a) as-deposited and (b) after Ar^+ cleaning, and α-C:H:N (c) as-deposited and (d) after Ar^+ cleaning.

Typical deconvoluted spectrum is shown in Figure 8.4a. The relative fraction of sp^3 binding was estimated from the ratio of sp^3 peak area over the total C 1s peak area. The binding energy and fractions of sp^2 and sp^3 bonding from the fitting shown in Figure 8.4a are summarized in Table 8.1. The sp^3 fraction of the α-C:H films is also plotted against ion energies and shown in Figure 8.4b. It can be seen see that the sp^3 fraction increases linearly from 36% to 55% with the ion energy varied from 24 eV to 48 eV.

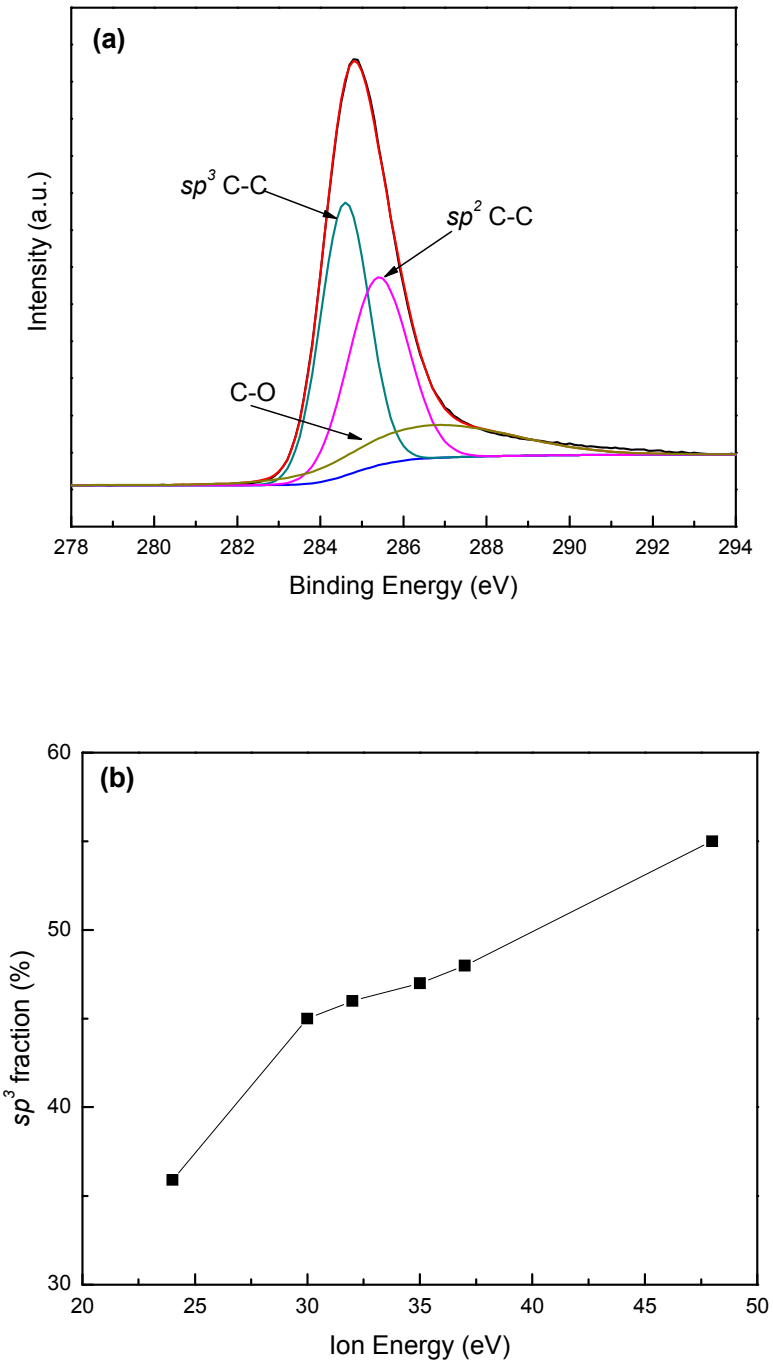

Figure 8.4. A typical XPS C1s spectrum and its fitting of α-C:H films (a) and sp^3 relative fractions as a function of ion energies (b).

In the survey spectra of α-C:H:N are shown in Figure 8.3 (c) as-deposited and (d) after Ar plasma cleaning. Similar to α-C:H, Ar plasma cleaning removed absorption of oxygen and nitrogen and introduced Ar to the films. Oxygen is estimated less than 3.0 at.% and Ar less than 4.5 at.% in the films. Besides that, an additional peak of N 1s is still clearly seen after cleaning. The value of N/C ratio is estimated to be approximately 0.087 based on the peak area ratio. According to Scharf *et al*. [*Scharf et al, 1999*], the C 1s of amorphous carbon nitride films can be deconvoluted with the peaks at binding energies of 284.5, 285.2, 286.5 and 288.6 eV attributed to sp^2C-C, sp^2C-N/sp^3C-C, sp^3C-N/spC-N and C–O bonds, respectively. The N 1s peak can be deconvoluted with four components at 397.2, 398.6, 400.1 and 402.3 eV [*Scharf et al, 1999*]. Figure 8.5 shows the spectra and fittings of C 1s and N 1s of α-C:H: N films. For N 1s, the components at 397.2 and 402.3 eV correspond to free N_2 and N-O bonds, respectively. The assignments the two major components at 398.6 and 400.0 eV are still controversial. While most authors agree the higher energy component should be assigned to N in substitutional graphite sites (N-sp^2C), the assignment of the lower energy component is diverse. It has been attributed to N-sp^3C by some authors [*Scharf et al, 1999;* Sjöström et al., 1995; *Hellgren et al., 1999*]. However, X-ray absorption spectroscopy studies [*Ripalda et al., 1999; Shimoyama et al., 2000; Quirós et al., 2000; Hellgren et al., 2001*] suggest that the component comes from pyridine-like N, i.e., N bonded to two C atoms at the edge of a graphitic structure

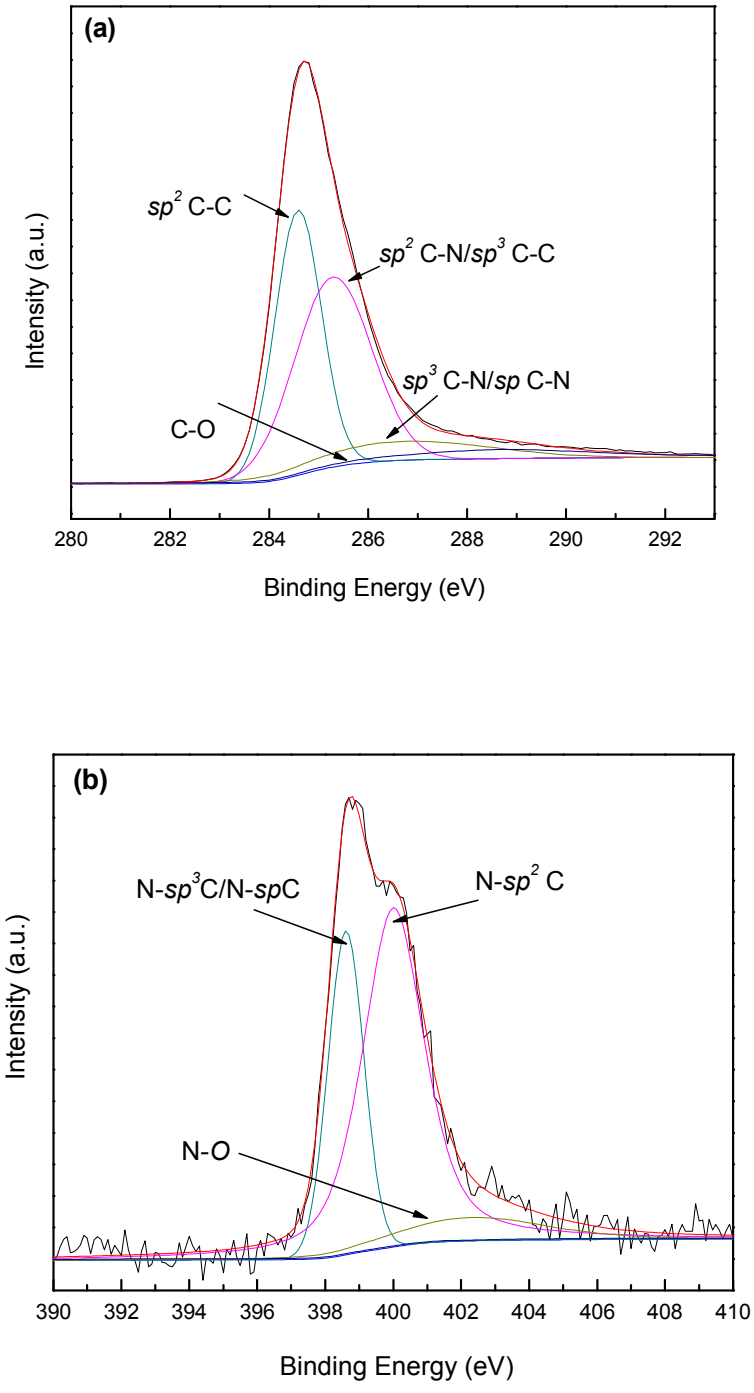

Figure 8.5. XPS spectra and their fittings of α-C:H:N: (a) C 1s and (b) N 1s.

The binding energy and relative fraction of the components are summarized in Table 8. 1. The peak at approximately 285.2 eV for α-C:H:N corresponds to sp^2C-N/sp^3C-C. Because of the small difference in binding energy, it is hard to distinguish sp^2C-N and sp^3C-C with XPS alone [*Rodil et al., 2004*]. This peak increases from 35.9% α-C:H to 44.8% after the addition of nitrogen. According to past reports [*Hu et al., 1998; Silva et al., 1997*], sp^3C-C fractions almost remain unchanged at lower nitrogen incorporation (N/C $\leq$ 0.1) and decreases at higher nitrogen content (N/C $\geq$ 0.1). Therefore, the increase of the sp^2C-N/sp^3C-C peak at 285.3 eV is largely due to the increase of sp^2C-N fraction. Nitrogen atoms tend to substitute C in sp^2C-C bonding, and the fraction of sp^2C-C bond reduces from 56.5% to 37.7%. The reduction of sp^2 C bonds also accounts for the smoothness of the α-C:H:N films because on the surface of α-C:H, there are a large number of H-terminated sp^2 C clusters, which are rough and loosely bonded with atomic scale voids existing at the cluster interfaces [*Zhao and Chen, 2001*].

Table 8.1. Binding energy and relative fraction of the components which contribution to the XPS spectra of C 1s and N 1s for α-C:H and α-C:H:N thin films.

α-C:H	Binding Types	Position (eV)	Area (%)	α-C:H:N	Binding Types	Position (eV)	Area (%)
C 1s	sp^2 C-C	284.5	56.5	C 1s	sp^2 C-C	284.5	37.7
	sp^3 C-C	285.3	35.9		sp^2 C-N /sp^3 C-C	285.2	44.8
	C-O	288.6	7.5		sp^3 C-N /sp C-N	286.6	10
					C-O	288.6	7
				N 1s	N_2	397.2	3.7
					N-sp^3 C/ pyridine-like N	398.6	26.6
					N-sp^2 C	400.0	60.5
					N-O	402.3	9.2

In Fig 8.6, the dependence of hardness and Young's modulus of the α-C:H films on the ion energy is shown. The hardness ranges from 8 to 12.5 GPa, and the Young's modulus values ranges from 100 to 130 GPa for the ion energy between 24 and 48 eV. The hardness range is reasonable for hydrogenated α-C:H films. As suggested by Robertson [*Robertson, 2002*], for hydrogenated α-C:H films, hardness values exceeding 20 GPa should be an overestimate unless there is some reason accounting for it, such as improved bonding or low hydrogen content. The ratios of hardness to Young's modulus are approximately 0.1 for all the films, as expected from hardness theory [*Tabor, 1970; Kelly and McMillan, 1986*]. Both hardness and Young's modulus increase with the increase of deposition ion energy, which correlates with the increase of sp^3 fractions. Hardness and Young's modulus of α-C:H:N are 15 GPa and 145 GPa, respectively, which are higher than those in any of the un-doped α-C:H samples. The values are higher than those in any of the un-doped α-C:H

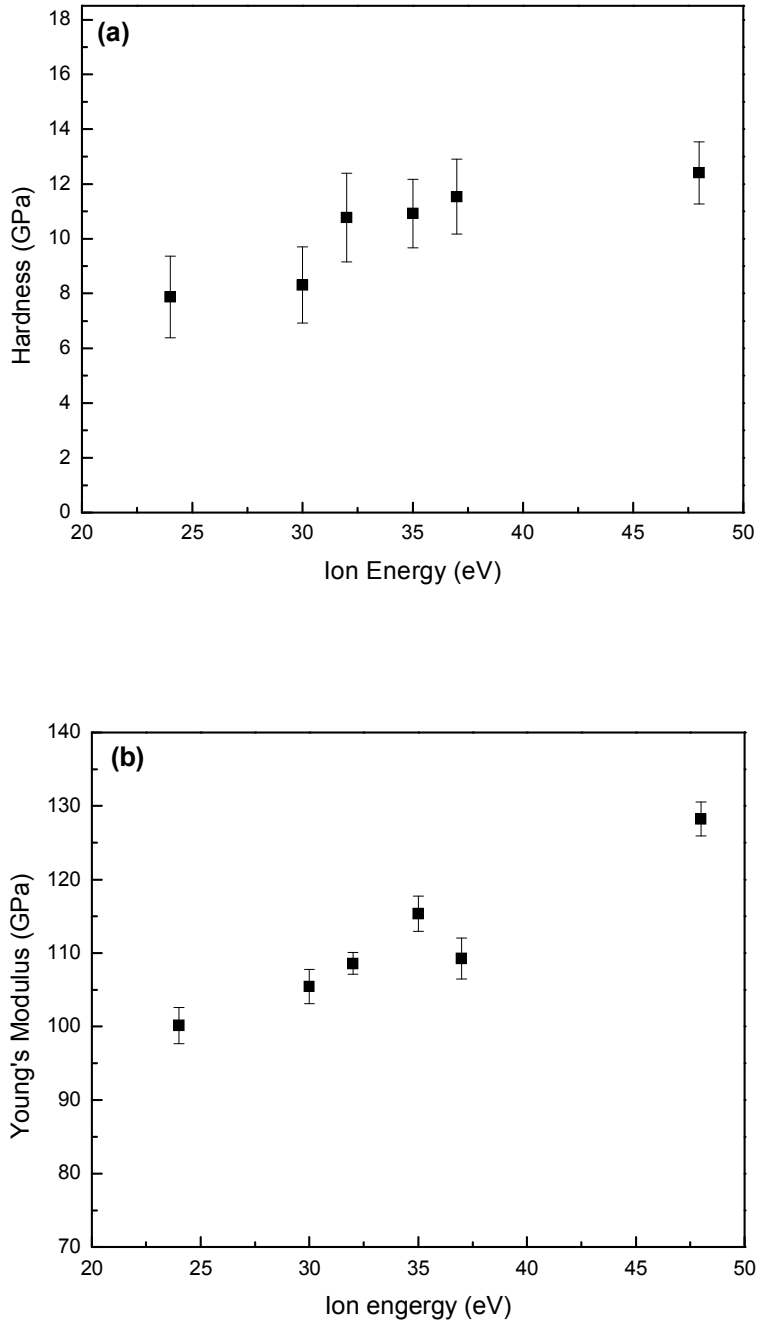

Figure 8.6. Mechanical properties: (a) Hardness and (b) Young's Modulus of α-C:H thin films vs ion energy

samples, which is contrary to many of the previous reports. To understand this effect, one should be aware the low nitrogen concentration in this work. Most of previous reports on carbon nitride thin films were attempting to achieve C_3N_4, and thus the nitrogen concentration is much higher. Large amount of nitrogen can disrupt sp^3 carbon network and results in lower hardness and Young's modulus. The N/C atomic ratio in this work is approximately 0.087 which is unlikely to change the sp^3 carbon fraction [*Hu et al., 1998; Silva et al., 1997*]. Secondly, the incorporation of nitrogen has an effect of reducing hydrogen content [*Silva et al., 1997*]. This would decrease hydrogen passivation of surface dangling bonds and lead to denser films and thus higher hardness and Young's modulus.

8.4 Conclusions

The microstructure and mechanical properties of α-C:H and α-C:H:N thin films deposited by an end-Hall ion beam source in the low ion energy range of 24 to 48 eV were studied. The films are uniform and smooth with RMS roughness values of 0.5-0.8 nm for α-C:H and 0.35 nm for α-C:H:N thin films. The sp^3 fraction of the α-C:H films increases from 36% to 55%, whereas the hardness increases from 8 GPa to 12.5 GPa and the Young's modulus increases from 100 GPa to 130 GPa when the deposition ion energy increases from 24 to 48 eV. The N/C atomic ratio, the hardness and Young's modulus of the α-C:H:N films are, 0.087, 15 GPa, and 145 GPa, respectively, which are higher than those in any of the un-doped α-C:H samples. The results have demonstrated that smooth and uniform α-C:H and α-C:H:N films with large area and reasonably high hardness and Young's modulus can

be synthesized by EH ion source. In addition, increasing ion energy and doping with N can improve the mechanical properties of the films. The EH ion beam deposition of carbon based thin films would have potential applications such as protective coatings for magnetic storage, where the ever growth requirement of coating uniformity and smoothness cannot be met by traditionally used sputtering methods.

CHAPTER 9
CONCLUSIONS AND RECOMMENDATIONS

9.1 Conclusions

The main findings made in the work are as follows:

(1) A combination of hydrochloric acid and H_2 plasma pretreatments were used to reduce Co concentration at the substrate surface and to modify the substrate surface morphology. The results show that the pretreatments, (1) HCl etching, (2) H_2 plasma treatment +HCl etching, and (3) HCl etching + H_2 plasma treatment, were all effective in forming continuous and adhesive nanocrystalline diamond coatings. In particular, H_2 plasma pretreatment followed with HCl etching produces the highest diamond phase content. The results hold the promise to replace the hazardous Murakami's regent in the WC-Co pretreatment with more environmental friendly hydrochloride acid etching combined with hydrogen plasma pretreatment.

(2) The growth of diamond coatings on WC–Co tool substrates with intermediate layers has been investigated. Diamond films directly synthesized on the as-received tool substrates are of low quality associated with the formation of graphite-rich impurities at diamond film-substrate interface. TiN or TiCN thin film pre-coated on the tool substrates as barrier layer has been found to be effective to suppress graphite formation, but the resulting nucleation density and adhesion strength of diamond on

it is low. An Al thin film applied either directly on the blank tool substrate, or on the TiN, TiCN-interlayer, offers enhanced nucleation density and adhesion strength for the diamond films formed on them.

(3) Diamond nucleation and growth on a new double interlayer of W/Al was investigated, in which the thin layer of Al directly deposited on WC-Co was used to suppress the formation of graphite catalyzed by Co and the thin layer of W on the top of Al layer was used to enhance diamond nucleation. The results have demonstrated that the W/Al interlayer can enhance diamond nucleation and adhesion on WC-Co tools and thus facilitates the formation of adherent nanocrystalline diamond coatings on WC-Co inserts.

(4) Results of investigations of diamond nucleation and growth on several typical CFE (Ti, Cr and W) coated Si and WC-Co substrates were presented. The results show that the CFE interlayers deposited by ion beam sputtering with amorphous/nanocrystalline structure enhance diamond nucleation, leading to the formation of nanocrystalline diamond thin films on the CFE interlayers even under conventional microcrystalline diamond growth conditions. Among the three interlayers investigated, diamond nucleation density is the highest on W and the lowest on Ti. The results also demonstrate that the diamond nucleation density on CFE interlayers is much higher than those on widely used metal nitride interlayers.

(5) It has been demonstrated that diamond nanotips can be fabricated by ion beam etching of as-grown CVD diamond. The orientation of diamond nanotips can be controlled by adjusting the incident ion beam direction. The sp^2/sp^3 ratio at the

surface of diamond nanotips is slightly higher than that of as-grown diamond. Oriented diamond tip nano-arrays have been used to produce anisotropic frictional surface, which is successfully used in ultra-precision positioning systems.

(6) The microstructure and mechanical properties of α-C:H and α-C:H:N thin films deposited by an end-Hall ion beam source in the low ion energy range of 24 to 48 eV were studied. The films are uniform and smooth with RMS roughness values of 0.5-0.8 nm for α-C:H and 0.35 nm for α-C:H:N thin films. The sp^3 fraction of the α-C:H films increases from 36% to 55%, whereas the hardness increases from 8 GPa to 12.5 GPa and the Young's modulus increases from 100 GPa to 130 GPa when the deposition ion energy increases from 24 to 48 eV. The N/C atomic ratio, the hardness and Young's modulus of the α-C:H:N films are, 0.087, 15 GPa, and 145 GPa, respectively, which are higher than those in any of the un-doped α-C:H samples. The results have demonstrated that smooth and uniform α-C:H and α-C:H:N films with large area and reasonably high hardness and Young's modulus can be synthesized by EH ion source. In addition, increasing ion energy and doping with N can improve the mechanical properties of the films. The EH ion beam deposition of carbon based thin films would have potential applications such as protective coatings for magnetic storage, where the ever growth requirement of coating uniformity and smoothness cannot be met by traditionally used sputtering methods.

9.2 Recommendations for future work

(1) The deposition of diamond coatings on WC-Co with surface pretreatment and interlayers has been studied. Rockwell C Indentation test was used to qualitatively

characterize the adhesion properties of coating. For precise measurement of the critical load of coatings, scratch test should be used. Moreover, it is necessary to test the cutting performance of diamond coated cutting tools for further optimization of processing parameters of surface pretreatments and interlayer preparation.

(2) More systematic studies on the effects of experimental parameters on the formation of diamond nanotips is needed in order to elucidate the detailed formation mechanism and to further manipulate the nanotip structure for potential applications. These parameters include ion energy, beam current density and shape of starting CVD diamond grains, etching gases, etc.

(3) Preliminary results have been presented for creation of the anisotropic friction of the diamond nanostructured surface. More detailed investigations of the friction behavior, including the effects of nanotip orientation, load and moving speed, and the degradation of the structure due to friction and wear, should be of great scientific and technical interests.

(4) CH_4 was used as carbon source for the deposition of DLC. Other hydrocarbon gases may be used for adjusting the composition of DLC films. The H content and density of the DLC films have not been measured and would be desirable to be determined. In addition, tribological data of the DLC under various conditions would be needed for the future applications.

LIST OF REFERENCES

S. Aisenberg and R. Chabot, J. Appl. Phys. 42 (1971) 2953.

Y. Ando, Y. Nishibayashi, K. Kobashi, T. Hirao and K. Oura, Diamond Relat. Mater. 11 (2002) 824.

J.C. Angus and C.C. Hayman. Science 241 (1988) 913.

S.D. Berger, D.R. McKenzie and P.J. Martin, Philos. Mag. Lett. 57 (1988) 285.

S. Bhattacharyya, C. Cardinaud, and G. Turban, J. Appl. Phys. 83 (1998) 4491.

J.G. Buijnsters, P. Shankar, W. Fleischer, W.J.P. van Enckevort, J.J. Schermer, and J.J. ter Meulen, Diamond Relat. Mater. 11 (2002) 536.

F.P. Bundy, Science 13 (1962) 71057.

F.P. Bundy, J. Chem. Phys. 38 (1963) 631.

E. Cappelli, F. Pinzari, P. Ascarelli and G. Righini, Diam. Relat. Mater. 5 (1996) 292.

C. Casiraghi, A. C. Ferrari, R Ohr, A. J. Flewitt, D. P. Chu and J. Robertson, Phys. Rev. Lett. 91 (2003) 226104.

F.G. Celii, and J.E. Bultler, Ann. Rev. Phys. Chem. 42 (1991) 643.

C.J. Chen, L. Chang, T.S. Lin, and F.R. Chen, J. Mater. Res. 10 (1995) 3041.

L.-J. Chen, C.-C. Liu, N.-H. Tai, C.-Y. Lee, W. Fang, and I-N. Lin, *J. Phys. Chem. C* 112 (2008) 3759.

M.Y. Chen, K.Y. Wu, J. Hwang, M.T. Chang, L.J. Chou and C.S. Kou, Nanotechnology 18 (2007) 455706

Y.K. Chih, Y.L. Chueh, C.H. Chen, J. Hwang, L.J. Chou and C.S. Kou, Diamond Relat. Mater. 15 (2006) 1246.

F. Deuerler, H. van den Berg, R. Tabersky, A. Freundlieb, M. Pies and V. Buck, Diam. Relat. Mater. 5 (1996)1478.

J. Diaz, G. Paolicelli, S. Ferrer and F. Comin, Phys. Rev. B 54 (1996) 8064.

J.P. Ducommun, M. Cantagrel and M. Moulin, J. Mater. Sci. 10 (1975) 52.

Q.H. Fan, J. Gracio, E. Pereira, N. Ali and W. Ahmed, J. Mater. Res. 15 (2000) 2330.

C. Faure, W. Hänni, C. Julia Schmutz and M. Gervanoni, Diam. Relat. Mater. 8 (1999) 830.

A.C. Ferrari, A. LiBassi, B.K. Tanner, V. Stolojan, J. Yuan, L.M. Brown, S.E. Rodil, B. Kleinsorge and J. Robertson, Phys. Rev. B 62 (2000) 11089.

A.C. Ferrari and J. Robertson, Phys. Rev. B 63 (2001) 121405.

S. Ferro, *J. Mater. Chem.* 12 (2002) 2843.

B.H. Frazer, B. Gilbert, B.R. Sonderegger and G. De Stasio, Surf. Sci. 537 (2003) 161.

Y. Fu, B. Yan, N.L. Loh, C.Q. Sun and P. Hing, J. Mater. Sci. 34 (1999) 2269.

Y. Fu, B. Yan and N.L. Loh, Surf. Coat. Technol. 130 (2000) 173.

G.N. George and I.J. Pickering, GEOL 498/898 Class note, University of Saskatchewan, 2006.

N. Gitis, I. Hermann and S. Kuiry, in Proceedings of the 7th International Conference Coatings in Manufacturing Engineering, ed. by: K.-D. Bouzakis, Fr.-W. Bach, B. Denkena, M. Geiger, Laboratory for Machine Tools and Manufacturing Engineering, 1-3 October 2008, Chalkidiki, Greece.

H. Gleiter, Prog. Mater. Sci., 33 (1989) 223.

V.P. Godbole, K. Jagannadham and J. Narayan, Appl. Phys. Lett. 67 (1995) 1322.

M. Gowri, H. Li, T. Kacsich, J.J. Schermer, W.J.P. van Enckevort, and J.J. ter Meulen, Surf. Coat. Tech. 201 (2007) 4601.

K.J. Grannen, X. Ma, R. Thangaraj, J. Gui, and G.C. Rauch, IEEE Trans. Magn. 36 (2000) 120.

D.M. Gruen, Annu. Rev. Mater. Res. 29 (1999) 211.

P. Hammer, M. A. Baker, C. Lenardi and G. Lisser, Ion beam deposited carbon nitride films: Characterization and identification of chemical sputtering, Thin Solid Films 290/291 (1996) 107-111.

R. Haubner, A. Lindlbauer and B. Lux, Int. J. Refract. Met. Hard Mat. 14 (1996) 119.

N. Hellgren, M. P. Johansson, E. Broitman, L. Hultman and J.-E. Sundgren, Phys. Rev. B 59 (1999) 5162.

N. Hellgren, J. Guo, C. Sathe, A. Agui, J. Nordgren, Y. Luo, H. Agren and J.E. Sundgren, Appl. Phys. Lett. 79 (2001) 4348.

J.T. Hu, P.D. Yang and C. M. Lieber, Phys. Rev. B 57 (1998) R3585.

Y. Huang, H. Xiao, Z. Ma, J. Wang and P. Gao, Surf. Coat. Technol. 202 (2007) 180.

Y.S. Huang, W. Qiu and C.P. Luo, Thin Solid Films 472 (2005) 20.

S. Iijima, Y. Aikawa, and K. Baba, Appl. Phys. Lett. 57 (1990) 2646.

S. Iijima, Y. Aikawa, and K. Baba, J. Mater. Res. 6 (1991) 1491.

W. Jacob and W. Moller. Appl. Phys. Lett. 63 (1993) 1771.

X. Jiang, C.P. Klages, R. Zachai, M. Hartweg, and H.J. Fusser, Appl. Phys. Lett. 62 (1993) 3438.

P.O. Joffreau, R. Haubner and B. Lux, Int. J. Refract. Met. Hard Mat. 7 (1988) 186.

H.R. Kaufman, J. Vac. Sci. Technol. 15 (1978) 272.

H. R. Kaufman, Rev. Sci. Instrum. 61 (1990) 230.

H.R. Kaufman, J.M.E. Harper, and J.J. Cuomo, J. Vac. Sci. Technol. 16 (1979) 899.

H.R. Kaufman, R.S. Robinson and R.I. Seddon, J. Vac. Sci. Technol. A5 (1987) 2081.

Kelly, N.H. McMillan, Strong Solids, Oxford University Press, Oxford, 1986.

T. Kolber, A. Koepf, R. Haubner and H. Hutter, Int J. Refract. Met. Hard Mater. 17 (1999) 445.

J.G. Li, D.P. Hu, J. Mei. S. Liu and Y.Y. Li, Acta Metallur. Sinica 42 (2006)763.

Y.S. Li and A. Hirose, Chem. Phys. Lett. 433 (2006) 150.

Y.S. Li and A. Hirose, Surf. Coat. Tech. 202 (2007) 280.

Y.S. Li and A. Hirose, J. Appl. Phys. 101 (2007) 073503.

Y.S. Li, Y. Tang, Q. Yang, S. Shimada, R. Wei, Y. Lee and A. Hirose, Int J. Refract. Met. Hard Mater. 26 (2008) 465

Y.S. Li, Y. Tang, Q. Yang, C. Xiao and A. Hirose, Int J. Refract. Met. Hard Mater. 27 (2009) 417.

Y. Liao, R.C. Fang, Z.Y. Ye, N.G. Shang, S.J. Han, Q.Y. Shao, and S.Z. Ji, Appl. Phys. A 69 (1999) 101.

M. A. Lieberman and A. J. Lichtenberg, Principles of Plasma Discharges and Materials Processing, Wiley Press, 2005.

C.R. Lin, C.T. Kuo and R.M. Chan, Diam. Relat. Mater. 7 (1998) 1628.

S. Logothetidis and G. Stergioudis, Appl. Phys. Lett. 71 (1997) 2463.

X. Lu, Q. Yang, C. Xiao and A. Hirose, Appl. Phys. A 82 (2006) 293.

B. Lux and R. Haubner, in Diamond and Diamond-like Films and Coatings, ed. by R.E. Clausing, L.L. Horton, J.C. Angus and P. Koidl, Plenum Press, New York, 1991.

S. Matsumoto, Y. Sato, M. Tsutsumi, and N. Setaka, J. Mater. Sci. 17 (1982a) 3106.

S. Matsumoto, Y. Sato, M. Kamo, and N. Setaka, Jpn. J. Appl. Phys. 21 (1982b) 183.

P. Merel, M. Tabbal, M. Chaker, S. Moisa, and J. Margot, Appl. Surf. Sci. 136 (1998) 105.

J. Michler, S. Laufer, H. Seehofer, E. Blank, R. Haubner, and B. Lux, Proc. 10th Int. Conf. on Diamond and Diamond-like Materials, Prague, Czech Republic, 12-17 Sept. 1999, paper 5.231.

B.A. Movchan and A.V.Demchishin, Phys. Met. Metallogr. 28 (1969) 83

R.J. Nemanich, J.T. Glass, G. Lucovsky and R.E. Shroder, J. Vac. Sci. Technol. A 6 (1988) 1783.

H. Niederwald, S. Laux, M. Kennedy, U. Schallenberg, A. Duparré, M. Mertin, N. Kaiser, D. Ristau, Appl. Optics 38 (1999) 3610.

H. Ollendorf and D. Schneider, Surf. Coat. Technol. 113 (1999) 86.

Y.Q. Pan and Y. Yin, Diamond Relat. Mater. 16 (2007) 220.

A.L. Patterson, Phys. Rev. 56 (1939) 978.

P.E. Pehrsson, F.E. Celii, and J.E. Butler, “Chemical mechanisms of diamond CVD” in Diamond films and coatings, ed. by R.F. Davis, Noyes, Park Ridge, NJ, 1993.

M.G. Peters and R.H. Cummings, European Patent 0519587 A1 (1992).

R. Polini, Thin Solid Films, 515 (2006) 4.

R. Polini, F.P. Mantini, M. Barletta, R. Valle, and F. Casadei, Diamond Relat. Mater. 15 (2006) 1284.

C. Quirós, J. Gómez-García, F. J. Palomares, L. Soriano, E. Elizalde and J. M. Sanz, Appl. Phys. Lett. 77 (2000) 803.

V.G. Ralchenko, A.A. Smolin, V.G. Pereverzev, E.D. Obraztsova, K.G. Korotoushenko, V.I. Konov, Y.V. Lakhotkin and E.N. Loubnin, Diamond Relat. Mater. 4 (1995) 754.

J. M. Ripalda, E. Román, N. Díaz, L. Galán, I. Montero, G. Comelli, et al., Phys. Rev. B 60 (1999) R3705.

J. Robertson, Mater. Sci. Eng. R 37 (2002) 129.

J. Robertson, Tribol. Int. 36 (2003) 405.

S.E. Rodil, N.A. Morrison, J. Robertson and W.I. Milne, Phys. Status Solidi A 175 (1999) 25.

S.E. Rodil and S. Muhl, Diam. Relat. Mater. 13 (2004) 1521.

S.R. Sails, D.J. Gardiner, M. Bowden, J. Savage and D. Rodway, Diamond Relat. Mater. 5 (1996) 589.

T.W. Scharf, R.D. Ott, D. Yang, and J.A. Barnard, J. Appl. Phys. 5 (1999) 3142.

X Shi, L.K. Cheah, J.R. Shi, Z. Sun, and B.K. Tay, J. Phys. Condens. Mat. 11 (1999) 185.

I. Shimoyama, G. Wu, T. Sekiguchi and Y. Baba, Phys. Rev. B 62 (2000) R6053.

R.E. Shroder and R.J. Nemanich, Phys. Rev. B 41 (1990) 3738

P. Sigmund, Phys. Rev. 184 (1969) 383

S. Silva, V.P. Mammana, M.C. Salvadori, O.R. Monteiro and I.G. Brown, Diam. Relat. Mater. 8 (1999) 1913.

S.R.P. Silva, J. Robertson, G.A.J. Amaratunga, B. Rafferty, L.M. Brown, J. Schwan et al., J. Appl. Phys. 81 (1997) 2626.

H. Sjöström, S. Stafström, M. Boman and J.-E. Sundgren, Phys. Rev. Lett. 75 (1995) 1336.

P.A. Steinmann and H.E. Hintermann, J. Vac. Sci. Technol. A 7 (1989) 2267.

B.R. Stoner and J.T. Glass, Appl. Phys. Lett. 60 (1992) 698.

C. Suryanarayana, Prog. Mater. Sci. 46 (2001) 1.

D. Tabor, Rev. Phys. Technol. 1 (1970) 145.

Y. Tang, S.L. Yang, W.W. Yi, Q. Yang, Y.S. Li, A. Hirose and R. Wei, in, Advanced Ceramic Coatings And Interfaces III Book Series: Ceramic Engineering And Science Proceedings, ed. by H.T. Lin and D. Zhu, , American Ceramic Society, Wiley InterScience, Vol. 29, 2009.

J. Taniguchi, N. Ohno, S. Takeda, I. Miyamoto, and M. Komuro, J. Vac. Sci. Tech. 16 (1998) 2506.

J. Taniguchi, J. Yokoyama, M. Komuro, H. Hiroshima and I. Miyamoto, Microelectron Eng. 53 (2000) 415.

N. Tayebi, A.A. Polycarpoua, and T. F. Conry, J. Mater.Res. 19 (2004) 1791.

K. B. K. Teo, S. E. Rodil, J.T. H. Tsai, A. C. Ferrari, J. Robertson, and W. I. Milne, J. Appl. Phys. 89 (2001) 3706.

O. Ternyak, R. Akhvlediani and A. Hoffman, Diamond Relat. Mater. 14 (2005) 323.

H. Tokutaka, N. Ishihara, K Nishimori, S Kishida and K Isomoto, *Surf. Interface Anal.* 18 (1992) 697

Z. Wang, C. Gu, J. Li and Z. Cui, Microelectron Eng. 78–79 (2005) 353.

W.D. Westwood, “Supported Discharges and Ion Beam” in Sputter Deposition, AVS, New York, 2003.

R.J. Waltman, H. Zhang, A. Khurshudov, D. Pocker, M.A. Karplus, B. York, Q.F. Xiao, H. Zadoori, J.U. Thiele and G.W. Tyndall, Tribol. Lett. 12 (2002) 51.

J.K. Wright, R.L. Williamson and K.J. Maggs, Mater. Sci. Eng. A 187 (1994) 87.

Q. Yang, W. Chen, C. Xiao, R. Sammynaiken and A. Hirose, Carbon 43 (2005) 748.

Q. Yang and Y.J. Tang, J. Phys. D: Appl. Phys. 42 (2009) 085306.

N. Yu and A.A. Polycarpou, J. Vac. Sci. Technol. B 22 (2004) 668.

S. Yugo, T. Kanai, T. Kimura and T. Muto, Appl. Phys. Lett. 58 (1991) 1036.

W.J. Zhang, X.M. Meng, C.Y. Chan, Y. Wu, I. Bello and S.T. Lee, Appl. Phys. Lett. 82 (2003) 2622.

W.J. Zhang, Y. Wu, C.Y. Chan, W.K. Wong, X.M. Meng, I. Bello, Y. Lifshitz and S.T. Lee, Diamond Relat. Mater. 13 (2004) 1037.

Q. Zhang, MSc. Thesis, University of Saskatchewan, 2009.

J.P. Zhao and Z.Y. Chen, Phys. Rev. B 3 (2001) 115318.

D. Zhou, D.M. Gruen, L.C. Qin, McCauley, and A.R. Krauss, J. Appl. Phys. 84 (1998) 1981.

W. Zhou, R.P. Apkarian, Z.L. Wang, D. Joy, Fundamentals of Scanning Electron Microscopy, in Handbook of microscopy for nanotechnology ed. by N. Yao, and Z.L. Wang, Kluwer Academic Publishers, 2005.

W. Zhu, R.C. McCune, J.E. deVries, M.A. Tamor and K.Y. S. Ng, Diam. Relat. Mat., 4 (1995) 220.

APPENDIX

Table A1.1. Some of the properties of diamond [http://www.docdiamond.com/articles/diamond-material-data.php]

Property	**Value**
Crystal structure	Diamond (cubic) Space group: Fd3m Pearson Symbol: cF8 Strukturbericht Designation: A4
Lattice parameter (300 K)	3.56683 Å 3.5597 Å
Bond length (300 K)	1.5445 Å
Bond angle (the tetrahedral angle)	$2\times\tan^{-1}(\sqrt{2})$ 1.9106332362... rads. 109.47122063...°
Packing fraction	$(\sqrt{3})\times\pi/16$ 0.34008738...
Relative hardness	10 Mohs
Knoop hardness	8000
Knoop microhardness (100) face (110), (111) faces	79 GPa 56–102 GPa 58–88 GPa
Vickers microhardness: (100) face (111) face	 88–147 GPa 98 GPa
Abrasive hardness	140,000
Modulus of elasticity	700–1200 GPa

Property	**Value**
Young's modulus ([111] direction)	1223 GPa
Volume compressibility	18×10^{-10} m^2 N^{-1}
Compressive yield strength	8680–16530 MPa
Poisson's ratio	0.1–0.29
Bulk modulus	442.3 GPa
Linear expansion coefficient (300 K)	1.05×10^{-6} K^{-1}
Melting point	3773 K 4027 °C 3850 K
Coefficient of (linear) thermal expansion (20 °C)	1.18 μm m°C^{-1}
Heat capacity	0.4715 J g^{-1} °C^{-1}
Thermal conductivity: (Type-I, 300 K) (Type-IIa, 300 K) (Type-IIb, 300 K) —	 895 W m^{-1} K^{-1} 2300 W m^{-1} K^{-1} 1350 W m^{-1} K^{-1} 2000 W m^{-1} K^{-1}